

2007

## The detection of unique turbulent signatures resulting from atmospheric disturbances of flying aircraft

Mark Anthony Garnet  
*University of Dayton*

Follow this and additional works at: [https://ecommons.udayton.edu/graduate\\_theses](https://ecommons.udayton.edu/graduate_theses)

---

### Recommended Citation

Garnet, Mark Anthony, "The detection of unique turbulent signatures resulting from atmospheric disturbances of flying aircraft" (2007). *Graduate Theses and Dissertations*. 2828.  
[https://ecommons.udayton.edu/graduate\\_theses/2828](https://ecommons.udayton.edu/graduate_theses/2828)

This Thesis is brought to you for free and open access by the Theses and Dissertations at eCommons. It has been accepted for inclusion in Graduate Theses and Dissertations by an authorized administrator of eCommons. For more information, please contact [mschlangen1@udayton.edu](mailto:mschlangen1@udayton.edu), [ecommons@udayton.edu](mailto:ecommons@udayton.edu).

THE DETECTION OF UNIQUE TURBULENT SIGNATURES RESULTING FROM  
ATMOSPHERIC DISTURBANCES OF FLYING AIRCRAFT

Thesis

Submitted to

The School of Engineering of the

UNIVERSITY OF DAYTON

In Partial Fulfillment of the Requirements for

The Degree

Master of Science in Aerospace Engineering

by

Mark Anthony Garnet

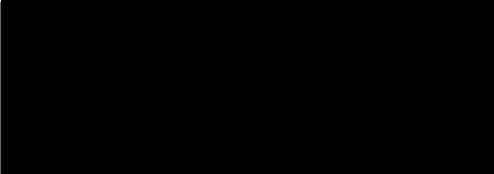
UNIVERSITY OF DAYTON

Dayton, Ohio

July 2007

THE DETECTION OF UNIQUE TURBULENT SIGNATURES RESULTING FROM  
ATMOSPHERIC DISTURBANCES OF FLYING AIRCRAFT

APPROVED BY:



Aaron Altman, Ph.D.  
Advisory Committee Chairman  
Assistant Professor, Department of  
Mechanical and Aerospace  
Engineering



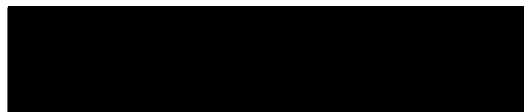
Kevin P. Hallinan, Ph.D.  
Committee Member  
Chairperson, Department of  
Mechanical and Aerospace  
Engineering



Andrew Sarangan, Ph.D.  
Committee Member  
Associate Professor, Electro-Optics  
Graduate Program



Malcolm W. Daniels, Ph.D.  
Associate Dean  
School of Engineering



Joseph E. Saliba, Ph.D., P.E.  
Dean, School of Engineering

©Copyright by  
Mark Anthony Garnet

All rights reserved

2007

## ABSTRACT

### THE DETECTION OF UNIQUE TURBULENT SIGNATURES RESULTING FROM ATMOSPHERIC DISTURBANCES OF FLYING AIRCRAFT

Name: Garnet, Mark Anthony  
University of Dayton

Advisor: Dr. Aaron Altman

During the mid 1990's, the National Aeronautics and Space Administration conducted research and experimentation on the detection of atmospheric turbulence through the use of laser detection and ranging equipment (LIDAR). This lidar technology was able to detect turbulent disturbances by the Doppler shift in the frequency of laser-emitted energy that is scattered from atmospheric aerosols. The main objective of this experimentation was to alleviate turbulent gust loads on aircraft and to prevent aircraft passenger injury through the detection and avoidance of severe turbulence. With the advent of this technology, practical applications could be developed to allow for the detection of turbulent disturbances physically created by the passage of aircraft through the atmosphere. Traditional aircraft detection methods include pulse-Doppler radar systems that measure the frequency shift of RF signals reflected off the skin of an aircraft. This traditional method of detection is currently being defeated through the use of stealth technology. As a military application, lidar turbulent detection would be able to spot the un-concealable turbulent disturbances caused by aircraft, and would defeat current stealth technology. In addition, research suggests that turbulent wake generators

(i.e. aircraft) have unique turbulent energy signatures. This revelation would conclude that detection technology could not only pinpoint the location of flying aircraft, but could also identify the aircraft through its turbulent signature. Through the use and manipulation of the Navier-Stokes equations, this thesis will explore the validity of this theory.

## ACKNOWLEDGEMENTS

My special thanks go out to Dr. Aaron Altman, Dr. Kevin Hallinan, and the University of Dayton Department of Mechanical and Aerospace Engineering for their approval in allowing me to research the visionary areas of this thesis. I would also like to thank Dr. Mark Glauser of the Syracuse University Department of Mechanical and Aerospace Engineering for his thoughts on the subject matter of this thesis and his suggestions for research material cited in this work. In addition, I would like to thank Ms. Olivia Pelletti of the National Air and Space Intelligence Center for providing me drag data for the aircraft presented in this work.

Finally, I would like to thank my wife, April, and children, McKenzie and Katie, for their support, patience, and understanding of the time I devoted to the research and authoring of this thesis. Without them, this paper would not have been possible.

## PREFACE

In today's dynamic battlefield environment, modern military forces use the latest technology to detect, identify, and neutralize the enemy. As technology becomes more sophisticated, the ability to achieve those three goals has become more complicated than ever. With the advent of stealth technology, military forces have been able to negate the ability of modern radars to detect aircraft, naval vessels, and ground vehicles through the use of radar absorbing materials (RAM) and multi-faceted geometries. The purpose of this paper is to discuss one possible approach to counter stealth technology. The author would like to note that the information contained in this thesis is solely referenced from his own imagination and the works cited in this paper. The author has no knowledge of any government projects currently researching the concepts presented here.

## TABLE OF CONTENTS

|   |     |
|---|-----|
| ABSTRACT.....   | iii |
| ACKNOWLEDGEMENTS.....   | v   |
| PREFACE.....  | vi  |
| LIST OF TABLES .....  | xi  |
| LIST OF SYMBOLS/ABBREVIATIONS.....                                  | xii |
| INTRODUCTION.....   | 1   |
| CHAPTER I: TURBULENT FUNDAMENTALS.....                              | 4   |
| Derivation of Reynolds Averaged Equations.....                      | 5   |
| Reynolds Decomposition .....  | 7   |
| Reynolds Stress and Kinetic Energy of the Mean Turbulent Flow ..... | 9   |
| Production Equals Dissipation .....                                 | 14  |
| Introduction to Turbulent Scales .....                              | 15  |
| Statistical Descriptions of Turbulence.....                         | 21  |
| Turbulent Self Preservation.....                                    | 26  |
| The Momentum Defect.....  | 30  |
| CHAPTER II: TURBULENT DETECTION BY RADAR.....                       | 37  |
| Basic Operating Principles of Radar.....                            | 37  |
| Radar Cross-Sections and Stealth.....                               | 44  |
| Detection of Clear Air Turbulence by Doppler Radar.....             | 51  |
| Detection of Clear Air Turbulence by Doppler Lidar .....            | 59  |
| CHAPTER 3: PRACTICAL APPLICATION OF TURBULENT WAKE DETECTION        |     |
| .....   | 63  |
| Preflight.....  | 65  |
| The Intercept .....   | 78  |
| Target Identification Using a Radar Only Configuration .....        | 82  |
| Target Identification Using a Lidar Configuration.....              | 85  |

|  |     |
|--|-----|
| The End Game.....                              | 88  |
| Conclusion and Recommendations .....           | 89  |
| VITA.....                                      | 91  |
| BIBLIOGRAPHY .....                             | 92  |
| APPENDIX 1: F-16C DRAG DATA.....               | 95  |
| APPENDIX 2: F-16C DRAG POLAR.....              | 96  |
| APPENDIX 3: F-15C DRAG DATA.....               | 97  |
| APPENDIX 4: F-15C DRAG POLAR.....              | 98  |
| APPENDIX 5: F-18C DRAG DATA.....               | 99  |
| APPENDIX 6: F-18C DRAG POLAR.....              | 100 |
| APPENDIX 7: B-52H DRAG DATA.....               | 101 |
| APPENDIX 8: B-52H DRAG POLAR.....              | 102 |
| APPENDIX 9: CHAPTER 3 SAMPLE CALCULATIONS..... | 103 |

## LIST OF ILLUSTRATIONS

|   |    |
|---|----|
| Figure 1: The drag coefficient of a flat plate. The several curves drawn in the transitional range (partially laminar, partially turbulent flow over the plate) illustrate that transition is very sensitive to small disturbances..... | 17 |
| Figure 2: Normalized energy and dissipation spectra for $R_\ell = 2 \times 10^5$ .....  | 22 |
| Figure 3: The measurement of the probability density of a stationary function. The function $l(t)$ represents the number of windows that $B(\tilde{u})$ occurs between $\tilde{u}$ and $\tilde{u} + \Delta\tilde{u}$ .....              | 23 |
| Figure 4: Example of PDF with a positive value of skewness .....  | 25 |
| Figure 5: Example of PDF with a small and large kurtosis.....   | 26 |
| Figure 6: The normalized turbulent intensity distributions for three wake generators ....   | 28 |
| Figure 7: The distributions of $\overline{uv}/u_o^2$ (non dimensional Reynolds stress) for the solid strip and airfoil .....  | 28 |
| Figure 8: Sketch defining nomenclature of the momentum wake in turbulent flow.....  | 30 |
| Figure 9: Radar Frequency bands.....  | 39 |
| Figure 10: Sensor frequencies and wavelengths .....   | 39 |
| Figure 11: Example of frequency difference between transmitted pulses from a pulse Doppler radar and reflected pulses from a moving air target.....   | 42 |
| Figure 12: The Doppler notch.....   | 43 |
| Figure 13: The German-Horten Aircraft.....  | 45 |
| Figure 14: SR-71: The first modern low-observable aircraft.....   | 46 |
| Figure 15: Basic principles of radar cross section.....   | 47 |
| Figure 16: Specular reflection and example of an aircraft using the concept in its design (F-117). .....  | 47 |
| Figure 17: The concept of radar diffraction.....  | 48 |
| Figure 18: Differences in design between the A-10 and F-117 that effect RCS .....   | 49 |
| Figure 19: The radar cross-section scale .....  | 50 |
| Figure 20: Examples of stealth aircraft: the F-22 Raptor and the B-2 Spirit.....  | 50 |
| Figure 21: Photograph of Kelvin-Helmholtz billows between 5-6 km in altitude using a pulse Doppler radar.....   | 58 |
| Figure 22: Basic principles of lidar use to detect CAT .....  | 61 |
| Figure 23: Configuration for lidar measurement of vertical velocity .....   | 61 |
| Figure 24: Picture of an actual APG-68 v9 radar. A notional APG-68 radar capable of detecting turbulent wakes may look similar.....   | 64 |
| Figure 25: MiG-29 with Slotback radar (not seen because it is within the nose radome) and IRSTS that is shown as a black protrusion just below the front of the canopy. .   | 65 |
| Figure 26: Example of F-16 radar display .....  | 66 |

|  |    |
|--|----|
| Figure 27: Hands on controls of the F-16 throttle.....   | 68 |
| Figure 28: Hands on controls of F-16 stick .....   | 69 |
| Figure 29: Reynolds stress model of B-52, F-16, F-15, and F-18 .....   | 75 |
| Figure 30: Close up view of Reynolds stress profile for the F-18, F-16, and F-15. ....   | 76 |
| Figure 31: Self-propelled momentum defect signatures and half-widths of F-16, F-18, F-15, and B-52 .....                               | 77 |
| Figure 32: Self-propelled momentum defect profiles for the B-52, F-16, F-18, and F-15 and their corresponding standard deviations..... | 77 |
| Figure 33: Viper 1 radar picture of initial contact with low-observable aircraft .....   | 79 |
| Figure 34: Viper 1 targets the low-observable aircraft (522 knots at 20,000' (STD temp) = $M=0.85$ ) .....                             | 80 |
| Figure 35: Geometric principles used to analyze radar contact parameters using two radar updates spaced 4 seconds apart. ....          | 81 |
| Figure 36: Description of the radar range gate sampling of turbulent flow 5 body lengths behind the targeted aircraft.....             | 83 |
| Figure 37: The total Reynolds stress of the F-18 model shown as the shaded area under the curve.....                                   | 84 |
| Figure 38: Instantaneous velocity fluctuations and the correlation to the F-16 PDF.....  | 86 |
| Figure 39: Instantaneous velocity fluctuations and the correlation to the F-15 PDF.....  | 87 |
| Figure 40: Instantaneous velocity fluctuations and the correlation to the F-18 PDF.....  | 87 |
| Figure 41: Radar display of identified hostile F-18 .....  | 88 |

## LIST OF TABLES

|   |    |
|---|----|
| Table 1: Coefficients of the refractive index as a function of height.....  | 55 |
| Table 2: Table of fighter aircraft lengths and resulting average fighter aircraft length ...  | 71 |
| Table 3: Table of bomber aircraft lengths and resulting average bomber aircraft length  | 71 |
| Table 4: Table of transport aircraft lengths and resulting average transport aircraft length<br>.....   | 71 |
| Table 5: Atmospheric conditions at 20,000' MSL.....   | 73 |
| Table 6: Calculated aerodynamic parameters for F-16, F-18, F-15, and B-52.....  | 73 |
| Table 7: Coefficients used for the Reynolds stress and self-propelled momentum defect<br>models.....  | 74 |
| Table 8: Modeled values for integral scale, mean rate of strain, Reynolds stress, and<br>turbulent dissipation for the F-16, F-15, and F-18 at $M=0.85$ , 20,000' MSL, at a<br>distance of $5\Delta x_f$ behind the aircraft..... | 84 |
| Table 9: Correlation between measured and modeled values of $\varepsilon$ for the F-16, F-15, and<br>F-18.....  | 85 |
| Table 10: Average velocity model of self-propelled momentum wake for F-16, F-15, and<br>F-18 at $5\Delta x_f$ .....   | 86 |
| Table 11: Correlation of self-propelled momentum defect average velocity and PDF<br>probability for F-16, F-15, and F-18.....   | 88 |

## LIST OF SYMBOLS/ABBREVIATIONS

|                     |  |
|---------------------|--|
| $\rho$              | Atmospheric density  |
| $\nu_T$             | Eddy viscosity or turbulent viscosity                      |
| $u_i$               | Fluctuating component of velocity                          |
| $U_\infty$          | Free stream velocity                                       |
| $\tilde{u}$         | Instantaneous velocity                                     |
| $\ell$              | Integral scale or characteristic length of large eddy size |
| $\overline{S_{ij}}$ | Mean rate of strain  |
| $\overline{U}_i$    | Mean velocity  |
| $\tau_{ij}$         | Reynolds stress tensor                                     |
| $T_{ij}$            | Total mean stress  |
| $\wp$               | Turbulent kinetic energy production                        |
| $\sigma^2$          | Variance   |
| $\tilde{s}_{ij}$    | Instantaneous strain rate                                  |
| $\sigma$            | Standard deviation   |
| $C_n^2$             | Turbulence parameter                                       |
| $\mu$               | Dynamic viscosity  |
| $\nu$               | Kinematic viscosity  |
| $\eta$              | Kolmogorov scale   |

|               |  |
|---------------|--|
| $\theta$      | Momentum thickness                         |
| $\theta_A$    | Radar azimuth                              |
| $\lambda$     | Taylor microscale                          |
| $\Theta_{BW}$ | Radar bandwidth                            |
| $\Delta n$    | Refractive index                           |
| $\lambda_R$   | Radar wavelength                           |
| $\eta_R$      | Reflectivity                               |
| $\Delta R$    | Sensor resolution cell                     |
| $A_D$         | Radar sensor aperture diameter             |
| $c$           | Propagation speed of wave (speed of light) |
| $C_D$         | Coefficient of drag                        |
| $e$           | Water vapor pressure                       |
| $f$           | Sensor operating frequency                 |
| $K$           | Kurtosis                                   |
| $k$           | Wave number                                |
| LHS           | Left Hand Side                             |
| $L_o$         | Turbulent wake half-width                  |
| $M$           | Momentum                                   |
| $N$           | Refractivity                               |
| N.S.          | Navier-Stokes                              |
| $P$           | Atmospheric pressure                       |
| PDF           | Probability Density Function               |
| $R$           | Target range                               |

|       |   |
|-------|---|
| RHS   | Right Hand Side                               |
| Ri    | Richardson Number                             |
| S     | Skewness                                      |
| T     | Temperature                                   |
| TKE   | Turbulent Kinetic Energy                      |
| $U_o$ | Amplitude of velocity profile (mean velocity) |

## INTRODUCTION

Germany's development of the modern radar between the years of 1928 and 1940 has been heralded as one of the greatest technological achievements of the 20<sup>th</sup> century. Although vast advances in radar technology have been made over the last 67 years, the basic principals of operation have remained the same. Through the transmission, skin reflection, and receiving of RF signals, the position and velocity of objects can be detected. Over the last two decades, these basic principals have been defeated through the use of stealth technology. By the use of multi-faceted geometries and radar absorbing materials, air and ground vehicles have been able to reduce their radar cross section; thereby reducing detection ranges and the engagement zones of radar guided munitions.

During the 1990's, experiments were conducted to detect clear air turbulence (CAT) by laser detection and ranging (LIDAR) equipment. Through the transmission and reflection of laser energy off of natural aerosols contained in the atmosphere, turbulent energy and turbulent fluctuations have been detected. The possible applications of this technology are far reaching. Since aircraft produce turbulence from their passage through an atmospheric fluid medium with greater turbulent energy than that produced by CAT, it is only reasonable to assume that the technology exists to detect the turbulent wakes generated by aircraft. As turbulent detection technology matures, its use as a military application becomes extremely appealing in light of defeatist methods used on traditional radars.

However, detection of aircraft is only one step in the process. Modern air forces typically follow rules of engagement (ROE) to ensure that friendly aircraft are not inadvertently destroyed during air battles. This task is not as easy as it seems. Through the current use of radio communications, computer data link, identification friend or foe systems (IFF), and other technologies, air forces can detect the friendly status of a radar target. All of these systems have one thing in common: they are all electrical systems that require the aircraft and the operator to ensure proper operation. Even these systems can be defeated or simulated with current electronic warfare counter measures. With this in mind, it is reasonable to explore the possibility that turbulent generators (i.e. aircraft) have unique turbulent energies that can be used to identify them as friendly or hostile. From this, a prediction can be made that only the receiver needs to have electronic equipment to detect the naturally occurring turbulent wake created by the unknown aircraft and thereby identifying its friendly status.

Turbulence research in the mid-1970's initially concluded that turbulent generators with identical momentum thicknesses resulted in identical turbulent intensities. However, research conducted on two-dimensional, turbulent, small-deficit wakes by Wygnanski, Champagne, and Marsali at the University of Arizona in 1983 made some startling revelations. By taking experimental turbulent intensity and drag calculations on generators tailored to have identical momentum thicknesses, the following conclusions were obtained<sup>1</sup>:

- 1) Normalized characteristic velocity and length scales depend on the initial conditions

---

<sup>1</sup> Wygnanski, F.; Champagne; Marasli, B. 1986: On the large-scale structures in two-dimensional, small-deficit, turbulent wakes. *Journal of Fluid Mechanics*. 168. pp. 31-71.

- 2) The shape of the normalized mean velocity profile is independent of the initial conditions or the nature of the generator
- 3) Normalized distributions of the longitudinal turbulence intensity *is* dependent on the initial conditions

Additional research performed by William George in the late 1980s at the University of Buffalo (SUNY) verifies this theory. The implication of this research is that different turbulent generators (i.e. aircraft) with identical momentum thicknesses can produce turbulent intensities that *are* dependent upon the aircraft's geometry. With this in mind, the logical conclusion is that if technology exists to detect turbulent intensities generated by flying aircraft, then each aircraft should have a unique turbulent intensity signature used for its identification. By doing this, the military requirements of detection and identification have been satisfied.

The goal of this thesis is to explore in detail the proposal outlined here. First, the author will provide a discussion on the fundamentals of turbulent flow and turbulent signatures. Next, a discussion on turbulent detection methods will be presented. Finally, real world aerodynamic data for the F-15C, F-16C Block 50, F-18C, and B-52 will be used to calculate the turbulent intensities of each individual aircraft to verify that each platform indeed has a unique signature.

## CHAPTER I: TURBULENT FUNDAMENTALS

While equations of motion are more easily manipulated using the assumption that a fluid is in a laminar state, it is important to note that naturally occurring laminar flows are exceptionally rare. Therefore, it is important to have an understanding of the Navier-Stokes equations that allows exploration of high Reynolds number flows. First, turbulent flow characteristics must be understood<sup>2</sup>:

- 1) Turbulent flows are irregular. This irregularity makes a deterministic approach to turbulent solutions impossible. Therefore, statistical methods are used.
- 2) Turbulent flows are highly diffuse which allows rapid mixing and increases rates of momentum, heat, and mass transfer.
- 3) Turbulent flows always occur at large Reynolds numbers.
- 4) Singularities occur in turbulent solutions due to high Re. Non-linearity and randomness make turbulent problems nearly intractable.
- 5) Turbulence exhibits random 3-D vorticity. The essence of turbulence is its ability to produce new and/or increased vorticity from vorticity already present. This can only happen if the flow is three-dimensional. This fact leads to the concept

---

<sup>2</sup> Tennekes, H. and Lumley, J.L. *A First Course In Turbulence*. The MIT Press, Cambridge, Massachusetts, 1972, pp. 1-4.

of an energy cascade where energy moves from larger to smaller scales.

- 6) Turbulence exhibits viscous dissipation. Although turbulent flows are primarily inviscid, scales are created (through vortex stretching and other means) within the flows that are sufficiently small so that viscosity can dominate.
- 7) The smallest scales of turbulence are usually much greater than the free path of the molecular exchange.
- 8) Turbulence is not a property of the fluid, but rather a state of motion of the fluid.

### Derivation of Reynolds Averaged Equations

The following section shows the derivation of the incompressible Navier-Stokes equations. The understanding and manipulation of the N.S. equations is fundamental for the understanding of a mathematical turbulent description. The following equations are in Einstein summation convention and this convention is used whenever possible in this paper.

First, the equations of motion for an incompressible fluid and the continuity equation shown in Equation 1 and Equation 2. The “~” notation indicates an instantaneous value.

$$\frac{\partial \tilde{u}_i}{\partial t} + \tilde{u}_j \frac{\partial \tilde{u}_i}{\partial x_j} = \frac{1}{\rho} \frac{\partial}{\partial x_i} \tilde{\sigma}_{ij}$$

**Equation 1: Equation of Motion for an Incompressible Fluid**

$$\frac{\partial \tilde{u}_i}{\partial x_i} = 0$$

**Equation 2: Continuity equation**

By assuming that the fluid is Newtonian, the constitutive relationship and the mathematical expression for the rate of strain (shown in Equation 3 and Equation 4 respectively) can be used and substituted into Equation 1.

$$\tilde{\sigma}_{ij} = -\tilde{p}\delta_{ij} + 2\mu\tilde{s}_{ij}$$

**Equation 3: Constitutive Relationship**

$$\tilde{s}_{ij} = \frac{1}{2} \left( \frac{\partial \tilde{u}_i}{\partial x_j} + \frac{\partial \tilde{u}_j}{\partial x_i} \right)$$

**Equation 4: Rate of Strain**

$$\frac{\partial \tilde{u}_i}{\partial t} + \tilde{u}_j \frac{\partial \tilde{u}_i}{\partial x_j} = \frac{1}{\rho} \frac{\partial}{\partial x_i} \left\{ \tilde{p}\delta_{ij} + 2\mu\tilde{s}_{ij} \right\}$$

**Equation 5: Substitute Equation 3 into Equation 1**

Through substitution and expansion of the last term of Equation 5, the continuity equation is applied and allows for simplification. The result is the Navier-Stokes equations for an incompressible fluid shown in Equation 7.

$$\frac{\partial \tilde{u}_i}{\partial t} + \tilde{u}_j \frac{\partial \tilde{u}_i}{\partial x_j} = -\frac{1}{\rho} \frac{\partial \tilde{p}}{\partial x_i} + \nu \frac{\partial}{\partial x_j} \left( \frac{\partial \tilde{u}_i}{\partial x_j} + \frac{\partial \tilde{u}_j}{\partial x_i} \right)$$

$$\nu \frac{\partial^2 \tilde{u}_i}{\partial x_j \partial x_j} + \cancel{\nu \frac{\partial}{\partial x_i} \left( \frac{\partial \tilde{u}_j}{\partial x_j} \right)}$$

**Equation 6: Substitute Equation 4 into Equation 5. Expand last term and apply continuity.**

$$\frac{\partial \tilde{u}_i}{\partial t} + \tilde{u}_j \frac{\partial \tilde{u}_i}{\partial x_j} = -\frac{1}{\rho} \frac{\partial \tilde{p}}{\partial x_i} + \nu \frac{\partial^2 \tilde{u}_i}{\partial x_j \partial x_j}$$

**Equation 7: Incompressible Navier Stokes Equation**

The convective term (2<sup>nd</sup> term on the LHS of Equation 7) scales proportional to Reynolds number as Re increases. Conversely, the viscous dissipation term (2<sup>nd</sup> term on the RHS of Equation 7) tends to grow very small at very large Reynolds numbers.

### Reynolds Decomposition

Due to the randomness associated with turbulent velocity fluctuations, it is imperative to use statistical methods to mathematically describe the flow field. In order to describe this, the flow must be analyzed in two parts: a mean (or average) and a fluctuating component. Thus, instantaneous velocity can be described as:

$$\tilde{u}_i = \overline{U}_i + u_i$$

**Equation 8: Instantaneous velocity described by the mean and fluctuating components of velocity**

Here, the instantaneous velocity equals the mean velocity (denoted by a capital U with an over bar) and the fluctuating component of velocity (denoted by the lower case u). The fluctuating component of velocity can be interpreted as a time average, an ensemble average, or, under certain conditions, a spatial average.

By applying this concept to the velocity and pressure terms, the Reynolds decomposition of the Navier-Stokes equations is generated:

$$\frac{\partial \overline{U}_i}{\partial t} + \frac{\partial u_i}{\partial t} + (\overline{U}_j + u_j) \frac{\partial}{\partial x_j} (\overline{U}_i + u_i) = -\frac{1}{\rho} \frac{\partial}{\partial x_i} (\overline{P} + p) + \nu \frac{\partial^2 (\overline{U}_i + u_i)}{\partial x_j \partial x_j}$$

**Equation 9: Navier-Stokes equation expanded through Reynolds Decomposition**

Next, the average of each of the terms are taken. By assuming that the flow is statistically steady, the first two terms of the LHS of Equation 9 reduce to zero. It is assumed that the average of the fluctuating velocity and pressure also reduce to zero.

Hence, the equation is simplified to:

$$\overline{U_j} \frac{\partial \overline{U_i}}{\partial x_j} + \overline{u_j \frac{\partial u_i}{\partial x_j}} = -\frac{1}{\rho} \frac{\partial \overline{P}}{\partial x_i} + \nu \frac{\partial^2 \overline{U_i}}{\partial x_j \partial x_j}$$

**Equation 10: Reynolds Averaged Equation non-final form**

Through further manipulation, zero is added to the second term on the LHS of Equation 10:

$$\begin{aligned} u_j \frac{\partial u_i}{\partial x_j} + 0 &= u_j \frac{\partial u_i}{\partial x_j} + u_i \frac{\partial u_j}{\partial x_j} \\ u_j \frac{\partial u_i}{\partial x_j} + 0 &= \frac{\partial}{\partial x_j} (u_i u_j) \end{aligned}$$

**Equation 11: Derivation of transport term of fluctuating momentum by turbulent velocity fluctuations.**

The final term in the RHS of Equation 11 represents the transport of fluctuating momentum by the turbulent velocity fluctuations in the flow. If  $u_i$  and  $u_j$  are uncorrelated, there is no turbulent momentum transport. Generally though,

$\frac{\partial}{\partial x_j} (\overline{u_i u_j}) \neq 0$ . This term exchanges momentum between the turbulence and the mean

flow, even though the mean momentum of the turbulent velocity fluctuations is zero.

Newton's Second Law relates the momentum flux to force so that it may be thought of as a divergence of a stress. Because of Reynolds decomposition, the turbulent motion can be perceived as a mechanism for producing stresses in the mean flow. Through further manipulation, the stresses are placed on the RHS of the Reynolds averaged equations:

$$\overline{U}_j \frac{\partial \overline{u}_i}{\partial x_j} = -\frac{1}{\rho} \frac{\partial \overline{P}}{\partial x_i} + \frac{1}{\rho} \frac{\partial}{\partial x_j} \left( \mu \frac{\partial \overline{u}_i}{\partial x_j} - \overline{\rho u_i u_j} \right)$$

**Equation 12: Reynolds Averaged Equations in final form**

To more easily manipulate Equation 12, the stresses are lumped into one term on the RHS of the equation.

$$\overline{U}_j \frac{\partial \overline{u}_i}{\partial x_j} = \frac{1}{\rho} \frac{\partial}{\partial x_j} \left( \sum_{ij} T_{ij} - \overline{\rho u_i u_j} \right)$$

**Equation 13: Reynolds Averaged Equation with simplified stress term**

Where the total mean stress,  $T_{ij}$  is equal to:

$$T_{ij} = \sum_{ij} \overline{-\rho u_i u_j} = -\overline{P \delta_{ij}} + 2\mu \overline{S_{ij}} - \overline{\rho u_i u_j}$$

**Equation 14: Definition of total mean stress**

### Reynolds Stress and Kinetic Energy of the Mean Turbulent Flow

The Reynolds stress tensor can be defined as:

$$\tau_{ij} = -\overline{\rho u_i u_j}$$

**Equation 15: Definition of Reynolds stress tensor**

Reynolds stress is symmetric. Therefore,  $\tau_{ij} = \tau_{ji}$ . The diagonal components of  $\tau_{ij}$  are the normal stresses (pressures). These stresses contribute little to the transport of mean momentum. The off diagonal components of  $\tau_{ij}$  are the shear stresses. These stresses play the dominant role in the theory of mean momentum transfer by turbulent motion. The Reynolds decomposition has isolated the effects of the fluctuations of the mean flow, however, Equation 13 contains 9 components of  $\tau_{ij}$  as unknowns, as well as  $\overline{P}$  and 3 components of the mean flow. These facts outline the closure problem of turbulence. If

one obtains additional equations from the Navier-Stokes equations,  $\tau_{ij}$  unknowns such as  $\overline{u_i u_j u_k}$  are generated by the non-linear inertia terms. This is a characteristic of all non-linear stochastic systems<sup>3</sup>. As a result, turbulent investigators have attempted to link a relation between  $\tau_{ij}$  and  $S_{ij}$ .

In order to obtain the equation of turbulent kinetic energy of the mean flow, the following equations are used:

a) Continuity (Equation 2)

b)  $\overline{U_j} \frac{\partial \overline{U_i}}{\partial x_j} = \frac{\partial}{\partial x_j} \left( \frac{T_{ij}}{\rho} \right)$  where the LHS represents the transport of mean momentum and the RHS represents viscous stress

**Equation 16: Equation of motion of steady mean flow in an incompressible fluid**

c) Equation of total mean stress (Equation 14) where the first term on the RHS of the equation represents stress due to pressure. The second term on the RHS represents viscous stress, and the third term on the RHS represents Reynolds stress.

$$d) \overline{S_{ij}} = \frac{1}{2} \left( \frac{\partial \overline{U_i}}{\partial x_j} + \frac{\partial \overline{U_j}}{\partial x_i} \right)$$

**Equation 17: Equation of the mean rate of strain**

e) Remember that the averaged momentum  $\overline{\rho u_i}$  of turbulent fluctuations is equal to zero.

---

<sup>3</sup> Tennekes, H. and Lumley, J.L. *A First Course In Turbulence*. The MIT Press, Cambridge, Massachusetts, 1972, p. 33.

To derive the equation of turbulent kinetic energy, Equation 16 is multiplied by the mean velocity  $\overline{U_i}$ :

$$\overline{U_i U_j} \frac{\partial \overline{U_i}}{\partial x_j} = \overline{U_i} \frac{\partial}{\partial x_j} \left( \frac{T_{ij}}{\rho} \right)$$

**Equation 18: Product of motion of steady mean flow in an incompressible fluid and mean velocity**  
To simplify, the LHS of Equation 18 is manipulated as shown below. This represents the transport of the mean kinetic energy.

$$\overline{U_i U_j} \frac{\partial \overline{U_i}}{\partial x_j} = \overline{U_j} \frac{\partial}{\partial x_j} \left( \frac{1}{2} \overline{U_i^2} \right)$$

**Equation 19: Derivation of the term representing transport of the mean kinetic energy**  
Additionally, the chain rule is used to simplify the RHS of Equation 18 as shown below.

$$\overline{U_i} \frac{\partial}{\partial x_j} \left( \frac{T_{ij}}{\rho} \right) = \frac{\partial}{\partial x_j} \left( \frac{T_{ij} \overline{U_i}}{\rho} \right) - \frac{T_{ij}}{\rho} \frac{\partial \overline{U_i}}{\partial x_j}$$

**Equation 20: Expansion of the LHS term of Equation 18**  
Next, Equation 19 and Equation 20 are combined and multiplied by  $\rho$  to obtain a new form of the turbulent kinetic energy (TKE) equation.

$$\rho \overline{U_j} \frac{\partial}{\partial x_j} \left( \frac{1}{2} \overline{U_i^2} \right) = \frac{\partial}{\partial x_j} (T_{ij} \overline{U_i}) - T_{ij} \frac{\partial \overline{U_i}}{\partial x_j}$$

**Equation 21: Manipulated form of the TKE equation**

The stress tensor is symmetric, and, as a result,  $T_{ij}=T_{ji}$ . Also, the product  $T_{ij} \frac{\partial \overline{U_i}}{\partial x_j}$  is equal to the product of  $T_{ij}$  and the symmetric part of  $\overline{S_{ij}}$  of the deformation rate  $\frac{\partial \overline{U_i}}{\partial x_j}$  (see Equation 22).

$$T_{ij} \frac{\partial \bar{U}_i}{\partial x_j} = T_{ij} \left[ \frac{1}{2} \left( \frac{\partial \bar{U}_i}{\partial x_j} + \frac{\partial \bar{U}_j}{\partial x_i} \right) \right]$$

**Equation 22: Equation representing the product of stress tensor and deformation rate as a function of mean strain.**

By substituting Equation 17 into Equation 22, the updated version of the kinetic energy of the mean flow is:

$$\rho \bar{U}_j \frac{\partial}{\partial x_j} \left( \frac{1}{2} \bar{U}_i^2 \right) = \frac{\partial}{\partial x_j} (T_{ij} \bar{U}_i) - T_{ij} \bar{S}_{ij}$$

**Equation 23: Updated equation of the kinetic energy of the mean flow as a function of the mean rate of strain.**

The first term in the RHS of Equation 23 represents the transport of the mean flow energy by stress. This term only changes energy within the control volume. This transport term integrates to zero if the integration refers to a control volume on whose surface either  $T_{ij}$  (the stress field) or  $\bar{U}_i$  vanishes<sup>4</sup>.

From the divergence theorem, where  $n_j$  is the unit normal to  $dS$ :

$$\int_V \frac{\partial}{\partial x_j} (T_{ij} \bar{U}_i) dV = \int_S n_j T_{ij} \bar{U}_i dS$$

**Equation 24: Applying divergence theorem to the transport of mean-flow energy by the stress  $T_{ij}$**   
If the work done by the stress on the surface of the control volume is zero, then only the volume integral of  $T_{ij} \bar{S}_{ij}$  can change the total amount of mean kinetic energy (i.e.

$\int_V T_{ij} \bar{S}_{ij} dV$ ). This term,  $T_{ij} \bar{S}_{ij}$ , is called deformation work. It represents the kinetic

energy of the mean flow that is lost to or retrieved from the agency that generates the

---

<sup>4</sup> Tennekes, H. and Lumley, J.L. *A First Course In Turbulence*. The MIT Press, Cambridge, Massachusetts, 1972, p. 60.

stress<sup>5</sup>. Deformation work is caused by the stresses that contribute to  $T_{ij}$ . By substituting Equation 14 into the term representing  $T_{ij}\overline{S_{ij}}$ , the following equation is obtained:

$$T_{ij}\overline{S_{ij}} = \overline{-P\delta_{ij}S_{ij}} + 2\mu\overline{S_{ij}S_{ij}} - \rho\overline{u_i u_j S_{ij}}$$

**Equation 25: Expanded expression for deformation work**

Pressure contributes zero deformation work in an incompressible fluid as shown in the following equation:

$$\overline{-P\delta_{ij}S_{ij}} = \overline{-PS_{ii}} = \overline{-P}\frac{\partial\overline{U_i}}{\partial x_i} = 0$$

**Equation 26: Equation showing pressure contributes zero deformation work in an incompressible fluid.**

Note that the contribution of viscous stresses to deformation work is always negative.

This means that mean viscous dissipation always represents a loss of mean kinetic energy. Hence,  $2\mu\overline{S_{ij}S_{ij}}$  is called mean viscous dissipation<sup>6</sup>.

When relating to Reynolds stresses, in most flows, their contribution to deformation work is always dissipative. Negative  $\overline{u_i u_j}$  occur in regions of  $\overline{S_{ij}}$ . Since the turbulent stresses perform deformation work, the kinetic energy of the turbulence benefits from this work. As a result,  $-\rho\overline{u_i u_j S_{ij}}$  is known as turbulent energy production.

By substituting Equation 14 into Equation 21, the equation for the mean flow becomes:

$$\overline{U_j}\frac{\partial}{\partial x}\left(\frac{1}{2}\overline{U_i U_j}\right) = \frac{\partial}{\partial x_j}\left(-\frac{P}{\rho}\overline{U_j} + 2\nu\overline{U_i S_{ij}} - \overline{u_i u_j U_i}\right) - 2\nu\overline{S_{ij}S_{ij}} + \overline{u_i u_j S_{ij}}$$

**Equation 27: Manipulated equation for the energy of the mean flow**

<sup>5</sup> Ibid. p. 60.

<sup>6</sup> Ibid. p. 61.

In Equation 27, the first three terms on the RHS (in parenthesis) represent, in order, pressure work, the transport of mean kinetic energy by viscous stresses, and the transport of mean kinetic energy by Reynolds stresses. These terms can only redistribute energy within the control volume. The last two terms on the RHS in Equation 27 represent the mean viscous dissipation and turbulent production, respectively.

The equation governing the kinetic energy  $\frac{1}{2} \overline{u_i u_i}$  of the turbulent velocity fluctuations is obtained by multiplying the Navier-Stokes equations by the instantaneous velocity, taking the time average of all terms, and subtracting Equation 27. The final equation, shown in Equation 28, is called the turbulent energy budget<sup>7</sup>.

$$\overline{U_j} \frac{\partial}{\partial x_j} \left( \frac{1}{2} \overline{u_i u_i} \right) = - \frac{\partial}{\partial x_j} \left( \frac{1}{\rho} \overline{u_j p} + \frac{1}{2} \overline{u_i u_i u_j} - 2\nu \overline{u_j s_{ij}} \right) - \overline{u_i u_j} S_{ij} - 2\nu \overline{s_{ij} s_{ij}}$$

**Equation 28: Equation of the turbulent energy budget**

Equation 28 provides the framework to be used for the measurement of the turbulent kinetic energy budget in the wake. By measuring the individual terms in Equation 28, the turbulent kinetic energy budget for the turbulent planar wake flow in pressure gradient can be constructed<sup>8</sup>.

Production Equals Dissipation

Turbulent flows can be considered homogeneous. This assumption is reasonable given the fact that high Reynolds number turbulent flows tend to approach a state of

<sup>7</sup> Tennekes, H. and Lumley, J.L. *A First Course In Turbulence*. The MIT Press, Cambridge, Massachusetts, 1972, p. 63.

<sup>8</sup> Xiaofeng, Liu, Thomas, Flint. 2004: Measurement of the turbulent kinetic energy budget of a planar wake flow in pressure gradients. *Experiments in Fluids*. 37. p. 472.

homogeneity at the smallest scales characteristic of the dissipative range<sup>9</sup>. In a steady, homogeneous, pure shear flow (in which all averaged quantities except  $U_i$  are independent of position and in which  $S_{ij}$  is constant), Equation 28 reduces to:<sup>10</sup>

$$-\overline{u_i u_j} S_{ij} = 2\nu \overline{s_{ij} s_{ij}}$$

**Equation 29: Production equals dissipation in a steady, homogeneous, pure shear flow**

This equation states that in this type of flow, the rate of production of turbulent energy by Reynolds stresses equals the rate of viscous dissipation<sup>11</sup>. To introduce a new term, future references to turbulent production will be shown as  $\phi$ , defined as:

$$\phi = -\overline{u_i u_j} S_{ij}$$

**Equation 30: Equation for turbulent energy production**

Additionally, future references to turbulent energy dissipation will be shown as  $\varepsilon$ , defined as:

$$\varepsilon = 2\nu \overline{s_{ij} s_{ij}}$$

**Equation 31: Equation for turbulent energy dissipation**

Therefore, the relationship between production and dissipation can be written as  $\phi = \varepsilon$ .

### Introduction to Turbulent Scales

Turbulence is associated with large Reynolds numbers. Because this value is so large in a turbulent flow, the flow is assumed to be inviscid. This is due to the fact the  $\rho V D \gg \mu$ . However, if this is the case, how can viscous turbulent dissipation be described? In order to understand this concept, and the concepts to follow in this thesis, it is important to introduce turbulent scales.

<sup>9</sup> *Ibid.* p. 472.

<sup>10</sup> Tennekes, H. and Lumley, J.L. *A First Course In Turbulence*. The MIT Press, Cambridge, Massachusetts, 1972, p. 64.

<sup>11</sup> *Ibid.* p. 64.

Aerodynamicists are first introduced to the concept of Reynolds number using the equation  $Re = \frac{uD}{\nu}$ . In this equation,  $D$  is defined as the characteristic length scale of the object placed in the fluid flow.  $D$  could be the length of the flat plate or the chord of a wing. It is obvious that  $D$  is directly proportional to Reynolds number. By increasing  $D$ , turbulence can be introduced into a flow. This is apparent when pouring water from a pitcher into a glass. If the distance between the pitcher and the glass is close, then the water seems to have a smooth, or laminar, flow. As the pitcher is lifted and the distance between the glass increases, the stream of water begins to break apart and become more turbulent. This is because the distance,  $D$ , between the glass and the pitcher, has increased enough to create a Reynolds number sufficiently large to induce a turbulent flow.

The flow over an object in a fluid can be characterized in one of three ways: 1) laminar, 2) transitional, and 3) turbulent. Transitional flow is not well defined, but occurs as a transition between laminar and turbulent flows. In the case of experimental measurements on a flat plate with varying coefficients of drag, Figure 1 shows the laminar, transitional, and turbulent Reynolds numbers as a function of coefficient of drag.

Turbulent flows generate large and small eddies. The large eddies do most of the transport of momentum of the flow. Between the largest and smallest eddies, there are many different length scales. However, only an attempt will be made to find an expression for the smallest length scale, called the Kolmogorov microscale, named after the Russian scientist, A. N. Kolmogorov in 1941. There will also be a reference to the Taylor microscale, named after G.I. Taylor, who defined a scale that is used as a tool to understand energy transfer between the largest eddy scales and the smallest eddy scales.

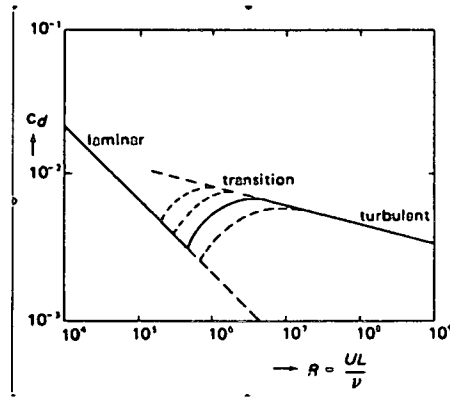


**Figure 1: The drag coefficient of a flat plate. The several curves drawn in the transitional range (partially laminar, partially turbulent flow over the plate) illustrate that transition is very sensitive to small disturbances<sup>12</sup>**

In a turbulent flow, the largest eddies are described by the symbol  $\ell$ .  $\ell$  also relates to the “integral” scale of turbulence. Using this term, the turbulent Reynolds number can be developed. Unlike the Reynolds number used by the characteristic length scale,  $D$ , of the object in the flow, the turbulence Reynolds number ( $R_\ell$ ) uses the length scale of the largest eddies. In addition,  $R_\ell$  has a lesser value than the object’s Reynolds number.

During the derivation of the terms for the dissipation and production of turbulent kinetic energy presented earlier in this thesis, it is suggested that any length scale involved in estimates of  $s_{ij}$  must be very much smaller than  $\ell$  if a balance between production and dissipation is to be obtained. The small scale of turbulence tends to be isotropic. In isotropic turbulence, the dissipation rate is equal to Equation 31. In 1959, Hinze derived another equation that allows us to re-write the term  $\overline{s_{ij}s_{ij}}$  in Equation 31 as

<sup>12</sup> Tennekes, H. and Lumley, J.L. *A First Course In Turbulence*. The MIT Press, Cambridge, Massachusetts, 1972, p. 18.

$\overline{\left(\frac{\partial u_1}{\partial x_1}\right)^2}$ . The following equation shows the new expression derived by Hinze for the

turbulent dissipation rate of kinetic energy:

$$\varepsilon = 2\nu \overline{s_{ij}s_{ij}} = 15\nu \overline{\left(\frac{\partial u_1}{\partial x_1}\right)^2}$$

**Equation 32: Term for turbulent dissipation rate of kinetic energy derived by Hinze in 1959.<sup>13</sup>**

G. I. Taylor defined a new length scale called the Taylor microscale that allows us to re-

write the  $\overline{\left(\frac{\partial u_1}{\partial x_1}\right)^2}$  term as:

$$\overline{\left(\frac{\partial u_1}{\partial x_1}\right)^2} = \frac{\overline{u_1^2}}{\lambda^2} = \frac{u^2}{\lambda^2}$$

**Equation 33: Introduction to the Taylor microscale**

The length scale,  $\lambda$ , is called the Taylor microscale. The substitution  $\overline{u_1^2} = u^2$  can be made because turbulence is assumed to be isotropic at small scales. With this assumption,  $\overline{u_1^2} = \overline{u_2^2} = \overline{u_3^2}$ . Since the small-scale structure of turbulence at large Reynolds numbers is always approximately isotropic, the following equation is used as an estimate of turbulent dissipation:

$$\varepsilon = 15\nu u^2 / \lambda^2$$

**Equation 34: Estimate of turbulent dissipation as a function of Taylor microscale and velocity**  
A relation between  $\lambda$  and  $\ell$  can be made using Equation 29. If it is assumed that  $S_{ij}$  is on the order of  $u/\ell$  and  $-\overline{u_i u_j}$  is on the order of  $u^2$ , then the following equation is obtained:

---

<sup>13</sup> Hinze, J.O., *Turbulence*. McGraw-Hill, New York, 1959.

$$Au^3 / \ell = 15\nu u^2 / \lambda^2$$

**Equation 35: Relationship between  $\lambda$  and  $\ell$**

The ratio of  $\lambda$  and  $\ell$  is given by:

$$\frac{\lambda}{\ell} = \left( \frac{15}{A} \right)^{\frac{1}{2}} \left( \frac{u\ell}{\nu} \right)^{-\frac{1}{2}} = \left( \frac{15}{A} \right)^{\frac{1}{2}} R_\ell^{-1/2}$$

**Equation 36: Ratio of  $\lambda$  and  $\ell$  as a function of turbulence Reynolds number**

The undetermined constant,  $A$ , is assumed to be on the order of one. Because in all turbulent flows,  $R_\ell \gg 1$ , the Taylor microscale  $\lambda$  is always much smaller than the integral scale  $\ell$ .<sup>14</sup>

The smallest length scale occurring in turbulence is called the Kolmogorov microscale,  $\eta$ . This scale is defined by:

$$\eta = \left( \frac{\nu^3}{\varepsilon} \right)^{1/4}$$

**Equation 37: Definition of the Kolmogorov microscale of length**

The difference between  $\eta$  and  $\lambda$  can be understood by looking at Equation 34. The dimensions of the strain-rate fluctuations are in units of frequency ( $\text{sec}^{-1}$ ). A time scale associated with turbulent dissipation is needed. This time scale is given by  $\tau$ , and is defined as:

$$\tau = (\nu / \varepsilon)^{1/2}$$

**Equation 38: Definition of the Kolmogorov microscale of time**

An additional relation that shows the ratio  $u/\lambda$  as a function of  $\tau$  is defined by the following:

---

<sup>14</sup> Tennekes, H. and Lumley, J.L. *A First Course In Turbulence*. The MIT Press, Cambridge, Massachusetts, 1972, pp. 66-67.

$$u/\lambda = 0.26\tau^{-1} = 0.26(\varepsilon/\nu)^{1/2}$$

**Equation 39: The ratio  $u/\lambda$  as function of  $\tau$**

With the preceding discussion in mind, it can be seen that the Taylor microscale is not a characteristic length of the strain-rate field and does not represent any group of eddy sizes in which dissipative effects are strong.<sup>15</sup> The Taylor microscale is also not a dissipation scale because it is defined with the assistance of a velocity scale that is not relevant for dissipative eddies.<sup>16</sup> Therefore,  $\lambda$  is only a tool used to provide a convenient estimate for  $s_{ij}$ .

The following equations were developed to show the relationships between  $\ell$ ,  $\lambda$ , and  $\eta$ <sup>17</sup>:

$$\frac{\lambda}{\ell} = \left(\frac{15}{A}\right)^{1/2} R_\ell^{-1/2} = \frac{15}{A} R_\lambda^{-1}$$

**Equation 40:  $\lambda/\ell$  shown as a function of both turbulence Reynolds number and microscale Reynolds number.**

$$\frac{\lambda}{\eta} = \left(\frac{225}{A}\right)^{1/4} R_\ell^{1/4} = 15^{1/4} R_\lambda^{1/2}$$

**Equation 41:  $\lambda/\eta$  shown as a function of both turbulence Reynolds number and microscale Reynolds number.**

The energy exchange between the mean flow and turbulence is governed by the dynamics of the large eddies. Large eddies contribute most to turbulent production because production increases with eddy size. The energy extracted by the turbulence from the mean flow thus enters the turbulence mainly at scales comparable to the integral scale  $\ell$ . The viscous dissipation of turbulent energy, on the other hand, occurs mainly at scales comparable to the Kolmogorov scale. This implies that the internal dynamics of turbulence must transfer energy from large scales to

---

<sup>15</sup> *Ibid.* p. 68.

<sup>16</sup> *Ibid.* p. 68.

<sup>17</sup> *Ibid.* p. 68.

small scales. All of the available experimental evidence suggests that this spectral energy transfer proceeds at a rate dictated by the energy of the large eddies (which is on the order of  $u^2$ ) and their time scale (which is on the order of  $\ell/u$ ). Thus, dissipation rate may always be estimated as  $\varepsilon = Au^3/\ell$  provided there exists only one characteristic length  $\ell$ . The estimate is independent of the presence of turbulent production, thus, the estimate is a valid statement about the dissipation rate even if production and dissipation do not balance<sup>18</sup>.

The interaction of energy production and dissipation can be visualized using the energy spectra plot shown in Figure 2. This plot clearly shows energy production that is normalized by the length scale  $\ell$  and the wave number  $k$ . Because turbulence contains eddies, and eddies tend to oscillate, an attempt is made to describe eddies in terms of waves. Energy production happens on the scale of  $\ell$ , and the wavelength of the eddy is defined as  $2\pi/k$  ( $k$  being the arbitrary wave number). Without going into further detail,  $k$  has units of  $\text{length}^{-1}$ . As a result,  $(k\ell)$  is a combination used to normalize the length scale for turbulent energy production. Similarly, turbulent dissipation happens on the scale of  $\eta$  (Kolmogorov scale). As a result, the turbulent dissipation length scale has been normalized as  $k\eta$ . Figure 2 graphs the shapes of the energy and dissipation spectra<sup>19</sup>. The region between the dashed vertical lines is called the “inertial subrange”.

### Statistical Descriptions of Turbulence

In order to accurately represent a statistical representation of a turbulent flow, an assumption must be made that the turbulent flow is statistically steady. This allows flows with fluctuating quantities of velocity to be measured. Despite the fact that turbulent flows are self-preserving (which will be discussed later in this chapter), an assumption

---

<sup>18</sup> Tennekes, H. and Lumley, J.L. *A First Course In Turbulence*. The MIT Press, Cambridge, Massachusetts, 1972, pp. 68-69.

<sup>19</sup> *Ibid.* p. 270.

must be made that the measurement of instantaneous velocity as a function of time in a turbulent flow is statistically independent of behavior at any other time.

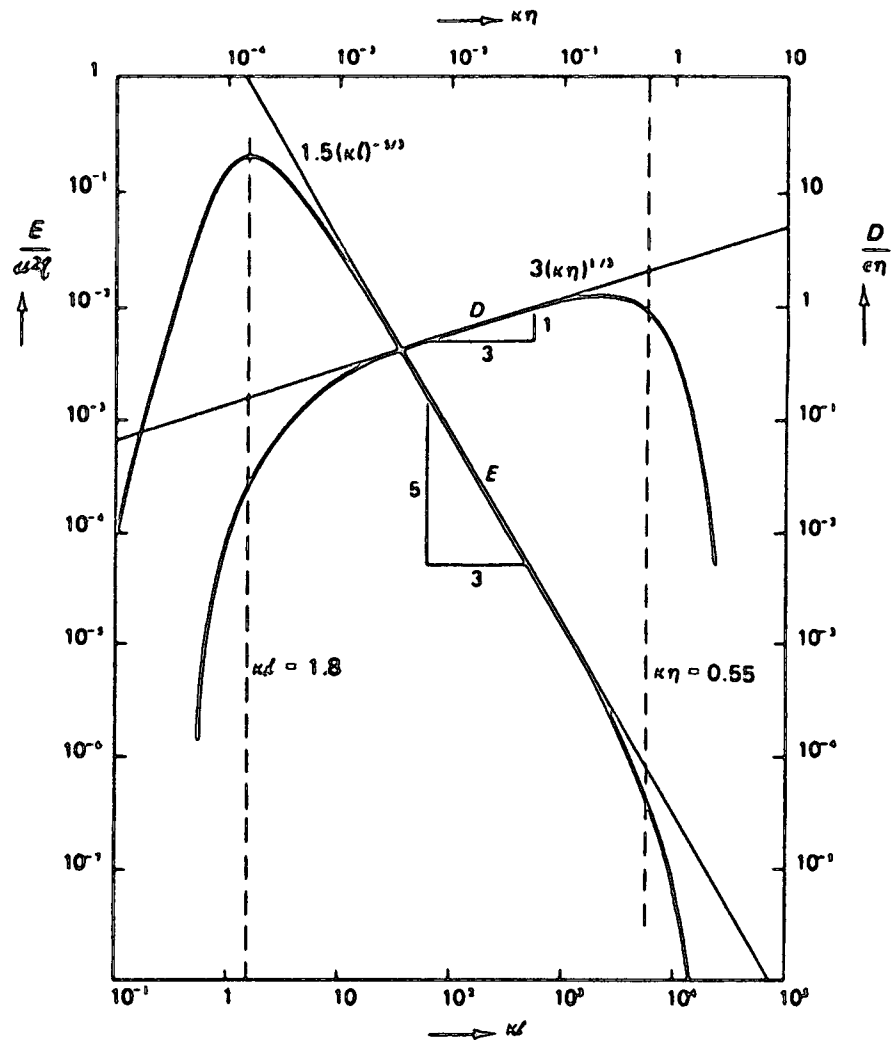


Figure 2: Normalized energy and dissipation spectra for  $R_\epsilon = 2 \times 10^5$ <sup>20</sup>

Therefore, it can be stated that no two identical experiments will result in the same data for instantaneous velocity as a function of time. However, turbulent flows have behavior that is only correlated for short times and spatial distances and becomes progressively uncorrelated as the time or spatial distance is increased. By using a deterministic process,

<sup>20</sup> *Ibid.* p. 270.

an attempt can be made to say that the behavior of a turbulent flow at a single or multiple occurrences determines the behavior at all times.

Measurement of the instantaneous fluctuating velocity can be taken as a function of time,  $\tilde{u}(t)$ . Figure 2 shows a representative graph of  $\tilde{u}(t)$ . The function,  $B(\tilde{u})$ , can be defined as the probability density function (PDF). The shape of  $B(\tilde{u})$  shown in Figure 2 is typical of the probability densities measured in turbulence.

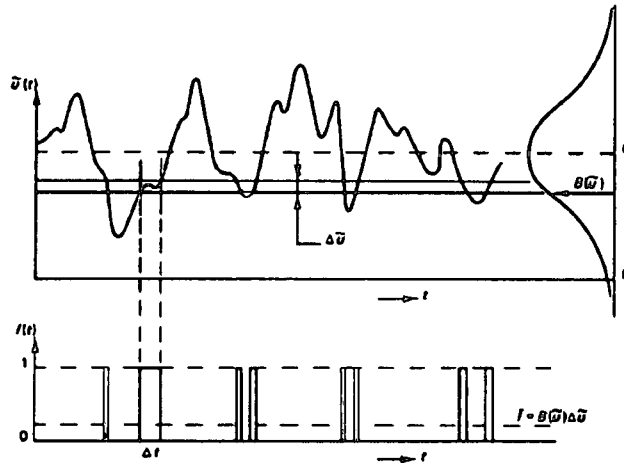


**Figure 3: The measurement of the probability density of a stationary function. The function  $I(t)$  represents the number of windows that  $B(\tilde{u})$  occurs between  $\tilde{u}$  and  $\tilde{u} + \Delta\tilde{u}$ <sup>21</sup>**

Let us define a window in the PDF called  $\Delta\tilde{u}$ . When  $\tilde{u}(t)$  falls within  $\Delta\tilde{u}$  then  $I(t)=1$ .

Otherwise,  $I(t)=0$ . The probability of finding  $\tilde{u}(t)$  within the window  $\Delta\tilde{u}$  is given by.

$$B(\tilde{u})\Delta\tilde{u} \equiv \lim_{t \rightarrow \infty} \frac{1}{t} \int_0^t I(t) dt$$

**Equation 42: Probability of finding an occurrence of  $\tilde{u}(t)$  within the window  $\Delta\tilde{u}$**

Basically, the probability of finding  $\tilde{u}(t)$  within the window  $\Delta\tilde{u}$  is equal to the proportion of the amount of time spent there.

<sup>21</sup> Tennekes, H. and Lumley, J.L. *A First Course In Turbulence*. The MIT Press, Cambridge, Massachusetts, 1972, p. 198.

The mean values of various powers of  $\tilde{u}$  are called moments. The first moment is the mean value:

$$\bar{U} \equiv \int_{-\infty}^{\infty} \tilde{u} B(\tilde{u}) d\tilde{u}$$

**Equation 43: Definition of the mean velocity of the PDF**

To make calculations easier, the mean velocity can be forced to equal to zero. It can be remembered that the fluctuating velocity equals the difference between the instantaneous and mean velocity (see Equation 8). As a result,  $B(\tilde{u}) = B(\bar{U} + u)$  which results in a PDF  $B(u)$  which is obtained by shifting  $B(\tilde{u})$  over a distance  $\bar{U}$  along the  $\tilde{u}$  axis. The first moment has now been formed and is called the central moment  $B(u)$ . The first central moment is equal to zero.

The second moment is called the variance and is shown by the symbol  $\sigma^2$ . It is defined by:

$$\sigma^2 \equiv \overline{u^2} = \int_{-\infty}^{\infty} u^2 B(\tilde{u}) d\tilde{u} = \int_{-\infty}^{\infty} u^2 B(u) du$$

**Equation 44: Definition of the variance of the PDF<sup>22</sup>**

The square root of the variance gives the standard deviation of the PDF, shown as  $\sigma$ . It defines the width of  $B(u)$ .

The third moment defines the skewness (S) of the  $B(u)$ . The skewness shows the symmetry or asymmetry of the PDF. The third moment,  $\overline{u^3}$  is typically non-dimensionalized by  $\sigma^3$ . If  $B(u)$  is symmetric about the axis, then  $\overline{u^3} = 0$  and  $S = 0$ . The equation for skewness is defined by:

---

<sup>22</sup> *Ibid.* p. 200.

$$S \equiv \overline{u^3} / \sigma^3$$

**Equation 45: Definition of skewness<sup>23</sup>**

Figure 4 shows the PDF  $B(u)$  with a positive skewness caused by more frequent negative values of  $u^3$  compared to the number of positive values of  $u^3$ .

The fourth moment, which is non-dimensionalized by  $\sigma^4$ , is called the kurtosis or flatness factor and is denoted by the symbol K. It is defined as:

$$K \equiv \frac{\overline{u^4}}{\sigma^4}$$

**Equation 46: Definition of kurtosis**

The kurtosis is large if the values of  $B(u)$  in the tails of the PDF are large. Figure 5 shows an example of a small and large kurtosis.

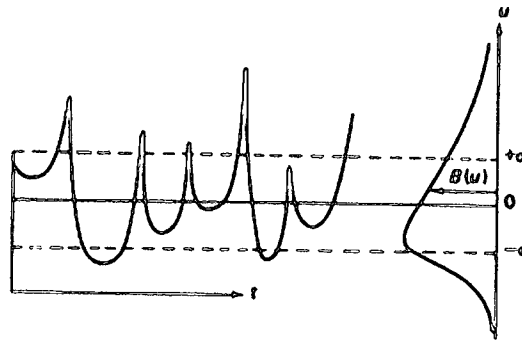


**Figure 4: Example of PDF with a positive value of skewness<sup>24</sup>**

<sup>23</sup> Tennekes, H. and Lumley, J.L. *A First Course In Turbulence*. The MIT Press, Cambridge, Massachusetts, 1972, p. 200.

<sup>24</sup> *Ibid.* p. 200.

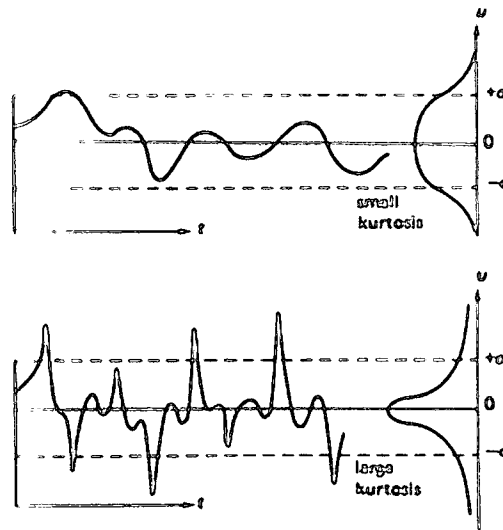


Figure 5: Example of PDF with a small and large kurtosis<sup>25</sup>

### Turbulent Self Preservation

The idea of self-preservation in turbulent flows began during the beginning of the 20<sup>th</sup> century. It was said to be first used by Blasius in 1908, and then Zel'dovick in 1937. Self-preservation is said to occur when the profiles of velocity (or any other quantity) can be brought into congruence by simple scale factors that depend on only one of the variables<sup>26</sup>. The major benefit of this fact is that it reduces the governing equations of 2-dimensional and axisymmetrical governing equations to ordinary differential equations.

There has been widespread belief in the turbulence community that flows achieve a self-preserving state by becoming asymptotically independent of their initial conditions. Thus, for example, all jets should asymptotically grow at the same rates; all wakes should be independent of their generators, and so forth. Such an argument is a logical consequence of a belief that 'turbulence forgets its origins', and can be modeled by its local properties. It is this belief that forms the basis of all single point models for turbulence<sup>27</sup>.

<sup>25</sup> *Ibid.* p. 201.

<sup>26</sup> George, William K. 1989: The self-preservation of turbulent flows and its relation to initial conditions and coherent structures. *Advances in Turbulence*. p. 39.

<sup>27</sup> *Ibid.* p. 39.

Experiments conducted by Wygnanski, Champagne, and Marasli challenged this belief despite widespread acceptance that ‘turbulence forgets its origins’. Experiments conducted by Townsend in 1956 used the velocity scale  $U_o$  and the single length scale  $L_o$  (which is the half-width of the turbulent wake) to normalize mean velocity and Reynolds stress. By doing this, it was theorized that mean velocity and Reynolds stress were now independent of the streamwise  $x$  coordinate. In attempt to verify the results of Townsend’s experiments, Wygnanski, Champagne, and Marasli obtained large differences in data that could not be attributed to experimental error. Of note were large variations of data that occurred at large values of  $x/C_D d$ , where  $C_D$  was the coefficient of drag of the turbulent wake generator in the experiment (in this case, a cylinder). Considerations based on the equations of motion show that the momentum thickness,  $\theta$ , should have been used as the normalizing length scale for the small deficit wake<sup>28</sup>. Basically, this conclusion stated that the total drag force on the cylinder should have been used to define the initial conditions. The following normalized velocity and length scales are obtained:

$$\left(\frac{U_\infty}{u_o}\right)^2 \approx \left(\frac{x - x_0}{2\theta}\right), \left(\frac{L_o}{\theta}\right)^2 \approx \left(\frac{x - x_o}{2\theta}\right)$$

$$\text{where } C_D d = 2\theta$$

**Equation 47: Small deficit wake velocity and length scales normalized by momentum thickness<sup>29</sup>**  
By using these new normalized length and velocity scales, it was found that different wakes develop differently with downstream distance. During their experiments, Wygnanski, Champagne, and Marasli constructed multiple turbulent wake generators

---

<sup>28</sup> Wygnanski, F.; Champagne, B.; Marasli, B. 1986: On the large-scale structures in two-dimensional, small-deficit, turbulent wakes. *Journal of Fluid Mechanics*. 168. pp. 31-71.

<sup>29</sup> *Ibid.* p. 32.

(cylinders, screens, solid strip, flat plate, and symmetrical airfoil) to obtain the same momentum thickness for each.

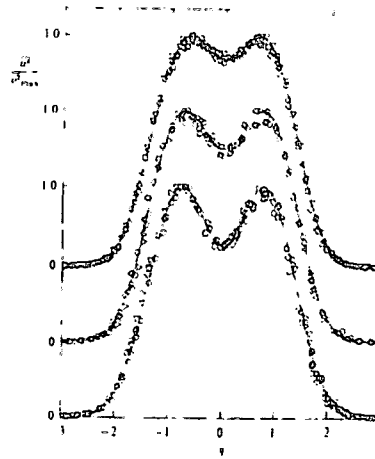


Figure 6: The normalized turbulent intensity distributions for three wake generators<sup>30</sup>

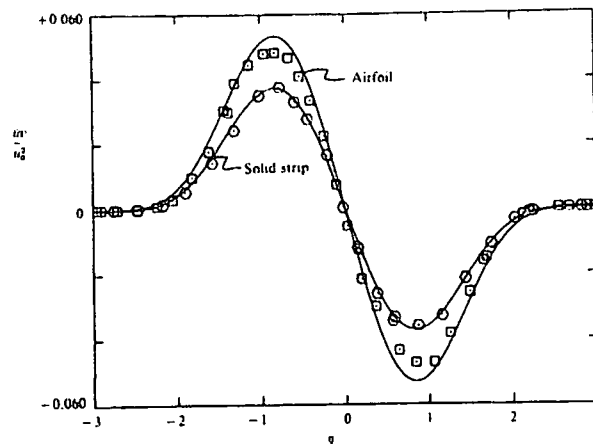


Figure 7: The distributions of  $\overline{uv} / u_o^2$  (non dimensional Reynolds stress) for the solid strip and airfoil<sup>31</sup>

As seen in Figure 6 and Figure 7, the experiments conducted by Wygnanski, Champagne, and Marasli show that there is indeed a difference in downstream turbulent effects that are resultant from initial conditions. Figure 6 clearly shows that the turbulent intensity distributions (measured at the same downstream location) for three different wake

<sup>30</sup> *Ibid.* p. 48.

<sup>31</sup> *Ibid.* p. 50.

generators produce different results. In Figure 6 and Figure 7, it is important to note that the horizontal axis, shown by  $\eta$ , is the non-dimensional distance  $y/L_0$ .

In 1992, W.K. George and M.M. Gibson published a paper dealing with the issue of self-preservation. The results of their experiments showed that the equations governing homogenous shear flows exhibited self-preservation and that these solutions were dependent upon initial conditions. In addition, George and Gibson found that the ratio of turbulent energy production rate to its dissipation rate remains constant ( $\frac{\rho}{\varepsilon}=\text{constant}$ ). They also showed that the energy spectra scale over all wave numbers, when normalized with  $q^2$  (Reynolds stress) and  $\lambda$  (Taylor microscale), have shapes determined by initial conditions<sup>32</sup>. Please refer again to Figure 2. The spectra shown in that example has a constant  $R_\ell=2 \times 10^5$  and is normalized by the large eddy characteristic length scale and the Kolmogorov scale.  $\frac{\rho}{\varepsilon}=\text{constant}$  implies that  $R_\ell$  is constant. What George and Gibson found in their experiments was that the turbulent energy spectra, when normalized by the Taylor microscale, changed shape based on the type of turbulent generator used. This implies that every turbulent generator has a unique energy and dissipation spectrum! From this revelation, it could be said with reasonable certainty that if the capability existed to measure the turbulent production or dissipation of aircraft, each aircraft would have a unique energy spectrum. This spectrum could then be used to identify the aircraft.

---

<sup>32</sup> George, W.K. and Gibson, M.M. 1992: The self-preservation of homogeneous shear flow turbulence. *Experiments in Fluids*. 13. pp. 229-238.

## The Momentum Defect

Say a velocity profile of an object is given in a turbulent flow defined by Figure 8.

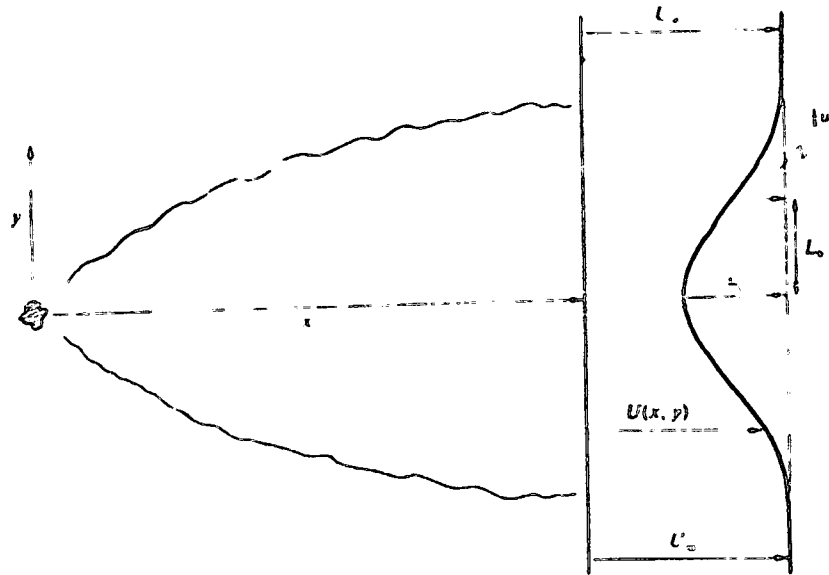


**Figure 8: Sketch defining nomenclature of the momentum wake in turbulent flow<sup>33</sup>**

In Figure 8, the velocity profile takes on a nice Gaussian shape.  $U_\infty$  represents the free stream velocity of the flow. The amplitude of the velocity profile (also representing the mean velocity of the velocity profile) is given by the variable  $U_0$ . Finally, the wake half width, defined by the value of  $U_0/2$ , is given by the variable  $L_0$ .

In turbulent flows, velocity fluctuations are created in three dimensions. However, the stream wise momentum is far greater than the cross-stream momentum effects<sup>34</sup>. As a result, cross-stream momentum effects can be ignored.

<sup>33</sup> Wygnanski, F.; Champagne; Marasli, B. 1986: On the large-scale structures in two-dimensional, small-deficit, turbulent wakes. *Journal of Fluid Mechanics*. 168. pp. 31-71.

<sup>34</sup> Tennekes, H. and Lumley, J.L. *A First Course In Turbulence*. The MIT Press, Cambridge, Massachusetts, 1972, pp. 106-107.

As an object passes through a fluid medium, the viscous interaction of the surface of the object and the surrounding medium causes the fluid to be “carried”. This phenomenon can be described using the following equation:

$$\rho \int_{-\infty}^{\infty} U(U - U_{\infty}) dy = M$$

**Equation 48: Equation of the momentum defect per unit volume**

Equation 48 represents the momentum defect per unit volume. When this term is used, it means that if the wake were not present, the momentum defect per unit volume would be  $\rho U_{\infty}$ . The difference  $\rho(U_{\infty} - U)$  is the momentum defect (or deficit). The constant  $M$  in Equation 48 is the total momentum removed per unit time from the flow by the obstacle that produces the wake<sup>35</sup>.

By using Equation 48, a new length scale can be defined in the turbulent description: momentum thickness. Imagine that the flow past an obstacle produces a completely separated, stagnant region of width  $\theta$ . The net momentum defect per unit volume is then  $\rho U_{\infty}$ , because the wake contains no momentum. The total volume per unit time and depth is  $U_{\infty}\theta$ , so that  $\rho U_{\infty}^2\theta$  represents the net momentum defect per unit time and depth. Thus:

$$-\rho U_{\infty}^2\theta = M$$

**Equation 49: Net momentum defect per unit time and depth<sup>36</sup>**

The length  $\theta$  is called the momentum thickness of the wake. It can be related to the drag per unit depth of the turbulent generator. Drag is defined as:  $D \equiv c_d \frac{1}{2} \rho U_{\infty}^2 d$ .

---

<sup>35</sup> *Ibid.* p. 112.

<sup>36</sup> *Ibid.* p. 112.

Drag is related to momentum where  $D = -M$ . Through substitution, the definition of drag can be placed into Equation 49 to obtain the relation  $C_D d = 2\theta$  shown in Equation 47. As the velocity profile moves downstream, the amplitude (or mean velocity)  $U_o$  of the profile decreases, while the width,  $L_o$ , increases. The magnitudes of both  $U_o$  and  $L_o$  can be approximated using the relations in Equation 47.

As stated earlier in this section, the velocity profile in Figure 8 resembles the Gaussian shape mentioned in the statistical description of turbulence. Using the tools given in the thesis thus far, a representative model of the velocity profile of a turbulent generator can be made based off of its coefficient of drag. If the coefficient of drag is known, an estimate of  $L_o$  and  $U_o$  can be made based on a given distance downstream. Those values are used to make a representative velocity profile using:

$$U_1(y) = U_o e^{-y^2 / 2L_o^2}$$

**Equation 50: Turbulent mean velocity profile model<sup>37</sup>**

Because Equation 50 resembles a Gaussian distribution, it can be said that it is now the PDF of the sample space. If enough samples are taken of the turbulent fluctuating velocity and they are compared to the mean velocity profile model (which is based off of a known coefficient of drag, i.e. for an aircraft), the level of probability that the turbulent wake is from that aircraft can be determined. This is because turbulent wakes are self-preserving and depend upon their initial conditions (i.e. aircraft have unique turbulent velocity and energy profiles). An example of this analysis will be made in Chapter 3. Setting a predetermined variance, skewness, and kurtosis can also narrow the identification process of the turbulent wake. If the values of the sample do not fall within

---

<sup>37</sup> Meunier, Patrice, Spedding, Geoffrey. 2006: Stratified propelled wakes. *Journal of Fluid Mechanics*. 552. pp. 229-256.

those pre-set limits, then it cannot be said with any degree of accuracy that the turbulent generator is identifiable as a known aircraft.

The above discussion represents a non-propelled body. However, aircraft are considered a self-propelled body and have a much different mean velocity profile. As a result, using the momentum defect technique would be extremely difficult to provide an accurate analysis in this case. The first reason the momentum defect calculation would be difficult is that a non-accelerating self-propelled body is in a condition where thrust equals drag. As a result, the turbulent wake is momentumless. However, the momentum-defect wake can still be seen when the aircraft is decelerating, and a momentum-defect jet is seen when the aircraft is accelerating. Therefore, the momentum defect can only be used to identify aircraft when they are maneuvering. This obviously decreases the amount of time-space that is needed for identification. However, the momentum defect technique would serve well for experimental analysis in a wind tunnel.

Other options are still available to continue the analysis. True momentumless wakes, where  $|U_B - U_c| \leq 4\%$ , are extremely difficult to obtain in the laboratory and in nature. A number of conditions can pull the wake far enough away from the momentumless condition and into a completely different regime. The possible perturbations include non-steady motion of the body, non-steady motion in the environment, and drag contributions from waves at boundaries, or internally within the fluid<sup>38</sup>. During their experimentation, Patrice Meunier and Geoffrey Spedding of the University of Southern California, noted that changes in self-propelled bluff body acceleration and deceleration, as well as fluctuations in velocity of the fluid, could cause

---

<sup>38</sup> *Ibid.* p. 253.

momentum wakes<sup>39</sup>. These fluid fluctuations are similar to oceanic currents or natural air currents in the atmosphere. Meunier and Spedding derived a calculation that could determine the mean amplitude of the momentum wake that is corrected for self-propelled (momentumless) condition. They concluded that if the velocity fluctuations (that cause a momentumless wake to exhibit a momentum defect) were on the order of 10% of the velocity of the bluff body, the mean absolute amplitude of the momentum wake would be equal to 46% of the amplitude of the wake without self-propulsion. This calculation is not unreasonable. If an aircraft at 20,000' MSL were cruising at 350 nm/hr, then approximately 35 knots of wind is needed (fluid velocity fluctuations) to cause a momentum wake of a non-maneuvering aircraft. Winds of this velocity occur often at these altitudes. With this in mind, Equation 50 can be corrected for the self-propelled condition.

$$U_1(y) = 0.54U_o e^{-y^2/2L_o^2}$$

**Equation 51: Turbulent mean velocity profile model of a self-propelled body**

The relations in Equation 47 are used to find values of  $L_o$  and  $U_o$  as a function of the momentum thickness and downstream position.

The final and most elegant method of identifying a self-propelled turbulent generator is through the detection of its Reynolds stress. In self-preserved, turbulent wakes, the mean profile of the wake diffuses due to the Reynolds stress, which is sustained by the mean shear. The hypothesis of a constant eddy viscosity can be checked for the case of stratified and propelled wakes. If  $\nu_T$  (eddy viscosity) is constant, then the

---

<sup>39</sup> Meunier, Patrice, Spedding, Geoffrey. 2006: Stratified propelled wakes. *Journal of Fluid Mechanics*. 552. p. 253.

Reynolds stress profile is proportional to  $\tilde{u}_1\tilde{u}_2 = \nu_T \frac{\partial \bar{U}_1}{\partial x_2}$ . Since the mean profile of velocity is approximated well by a Gaussian with amplitude  $U_o$ , the Reynolds stress profile should fit well by the derivative of a Gaussian function with an amplitude  $A$  and a width  $L_o'$  (see Equation 52).<sup>40</sup> An example of a Reynolds stress profile is shown in Figure 7.

$$\tilde{u}_1\tilde{u}_2(y) = -A \frac{y}{L_o'} e^{-y^2/L_o'^2}$$

**Equation 52: Reynolds stress profile model of a stratified or self-propelled body<sup>41</sup>**

The amplitude,  $A$ , should be similar to  $\nu_T U_o$  and the width  $L_o'$  should be similar to the wake width  $L_o$ . The value of  $\nu_T$  can be found using the relation  $\frac{\nu_T}{\nu} = c_1 R_\ell$  (reference Equation 36 for the definition of  $R_\ell$ )<sup>42</sup>. Tennekes and Lumley discuss the importance of carefully studying the kinetic energy budget to determine the value of  $c_1$ . However, determining the value of that coefficient is not of importance in this discussion and for the purposes of this thesis,  $c_1$  is on the order of one.

If the real-time components of velocity can be measured and the Reynolds stress of a self-propelled turbulent generator can be calculated, those values can be compared to the Reynolds stress profile model created from Equation 52. Knowing that  $R_\ell$  is constant (self-preservation), and that  $A$  and  $L_o'$  are dependent on the momentum thickness of a turbulent generator, the observed Reynolds stress can be compared to a Reynolds stress model created from a known coefficient of drag. If the observed values match the model

<sup>40</sup> *Ibid.* p. 242.

<sup>41</sup> *Ibid.* p. 242.

<sup>42</sup> Tennekes, H. and Lumley, J.L. *A First Course In Turbulence*. The MIT Press, Cambridge, Massachusetts, 1972, pp. 106-107.

to a specified degree of accuracy, the identity of the generator could be claimed. In other words, if the Reynolds stress profile of an aircraft in flight can be measured and compared to the Reynolds stress profile models of many known aircraft, a correlation could be made between the observed and model values that are subsequently used to identify the aircraft.

## CHAPTER II: TURBULENT DETECTION BY RADAR

In 1904, a German engineer named Christian Hulsmeijer invented the first telemobilescope. The device generated radio waves to detect ships at ranges of a few miles. 30 years after Hulsmeijer's invention, researchers in America, Britain, France, Italy, Germany, and the Soviet Union were at work on radar (Radio Detection and Ranging) techniques. In the summer of 1938, the German corporation Telefunken started testing the first reliable radar service.

### Basic Operating Principles of Radar

Radar detects scattered radiation from objects, and is particularly good at detecting highly reflective metallic objects against a less reflective background such as the sea or sky<sup>43</sup>. Waves are generated and transmitted in the radio-frequency part of the electro-magnetic spectrum. The radar receiver then captures the reflection of the waves as they are encountered and are transmitted back from objects of interest. Since the speed of the radio wave propagation from the radar is known as a constant, radar systems can determine the position, velocity, and other characteristics of an object by analysis of very high frequency radio waves reflected from its surfaces<sup>44</sup>.

The transmitted radio frequency is an electromagnetic wave that consists of an electric field and a magnetic field. These fields rapidly fluctuate in strength, rising to a

---

<sup>43</sup> Grant, Rebecca. *The RADAR game. Understanding Stealth and Aircraft Survivability*. IRIS Independent Research, Arlington, Virginia 1998, p. 6.

<sup>44</sup> *Ibid.* p. 6.

peak, falling away to zero, then rising to a peak again. This process repeats itself over and over as the wave propagates in the direction at right angles to the electric and magnetic field. The waves are measured in terms of frequency and wavelength. Frequency is measured in terms of kilohertz (one thousand cycles per second), megahertz (one million cycles per second), and gigahertz (one billion cycles per second). The wavelength represents the distances between two successive peaks of the electromagnetic wave and has units of distance. The wavelength is directly related to the physical size of the antenna<sup>45</sup>.

Radar systems are categorized according to their operating frequencies. In addition, each radar system's wavelength is a function of its frequency. This is given by the radar wavelength equation:

$$\lambda_R = \frac{c}{f}$$

**Equation 53: Equation for the wavelength ( $\lambda_R$ ) of a radar system**

Where  $c$  is the velocity of propagation of the wave ( $3 \times 10^{10}$  cm/s) and  $f$  is the sensor operating frequency. Figure 9 shows different bands of radar, their associated frequency range, and their associated wavelength.

---

<sup>45</sup> *Ibid.* p. 7.

| Band           | Frequency Range | Wavelength (cm) |
|----------------|-----------------|-----------------|
| VHF            | 30-300 MHz      | 1000-100        |
| UHF            | 300-1000 MHz    | 100-30          |
| L              | 1000-2000 MHz   | 30-15           |
| S              | 2000-4000 MHz   | 15-7.5          |
| C              | 4000-8000 MHz   | 7.5-3.75        |
| X              | 8000-12,500 MHz | 3.75-2.40       |
| K <sub>u</sub> | 12.5-18 GHz     | 2.40-1.67       |
| K              | 18-26.5 GHz     | 1.67-1.13       |
| K <sub>a</sub> | 26.5-40 GHz     | 1.13-0.75       |
| MMW            | $f > 30$ GHz    | $\lambda < 1.0$ |

Figure 9: Radar Frequency bands<sup>46</sup>

In addition, radar sensors are characterized by their frequency band (as shown in Figure 10).

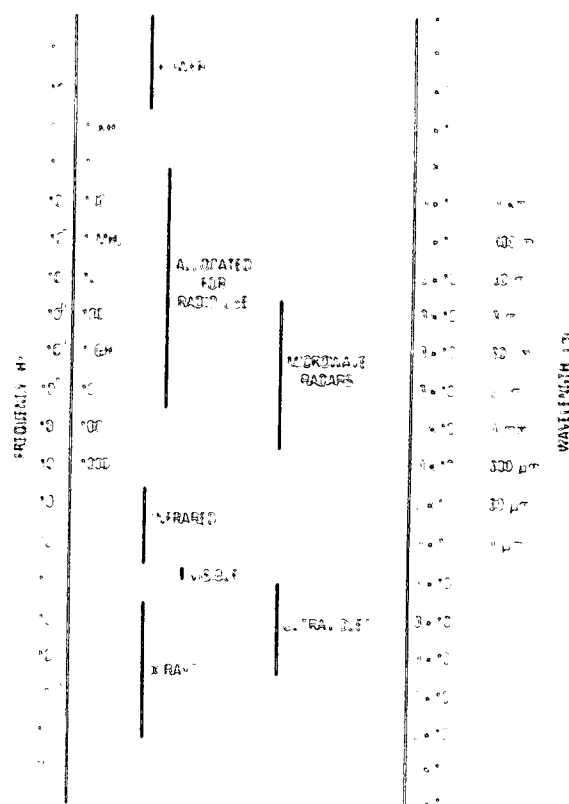


Figure 10: Sensor frequencies and wavelengths<sup>47</sup>

<sup>46</sup> Hovanessian, S.A. *Introduction to Sensor Systems*. Artech House, Norwood, MA, 1988, p. 6.

<sup>47</sup> *Ibid.* p. 5.

Most ground based radar systems are in the L-, S-, and C-band regions, while most airborne radars are in the X-band region. Infrared and electro-optical (i.e. laser) sensors operate at a much higher frequency with associated wavelengths shown in Figure 10.

Sensor systems are designed to be compatible with the atmospheric effects that are on that system. Usually, sensor systems are designed to operate under the conditions of rain, fog, snow, and other atmospheric phenomenon. These atmospheric conditions “attenuate” the transmitted radar frequency. The ratio of the signal strength to the attenuation is called the signal-to-noise (S/N) ratio. Usually, S/N is small at frequencies less than 20 GHz. After 30 GHz, there are several atmospheric windows where attenuation is tolerable. For the higher frequency ranges (such as the infrared and electro-optical systems), adverse weather effects play a major role in signal attenuation.

When considering the capabilities of a radar sensor, the resolution cell must also be determined. The resolution cell is defined as the corresponding area of space that a sensor is capable of resolving. For example, a large resolution cell would be good to search large volumes (such as weather radars). These types of searches are called “distributed” searches. A small resolution cell would be good for fighter aircraft radar. Enemy aircraft flying in formation within the resolution cell would look like a single target. By decreasing the resolution cell, more detail can be seen. Small resolution cells are for “point” searches. In order to determine the resolution cell, the beam width must be calculated. The beam width is defined as:

$$\Theta_{BW} = \frac{\lambda_R}{A_D}$$

**Equation 54: Definition of the beam width of a radar sensor<sup>48</sup>**

$A_D$  is defined as the aperture diameter of the radar. For example, a notional X-band microwave radar with a 9 GHz frequency has a wavelength of 3.3 cm. The sensor has a 30 cm aperture. The resulting beam width is 0.11 radians. To find the resolution cell, the following equation is used:

$$\Delta R = R\Theta_{BW}$$

**Equation 55: Equation for radar sensor resolution cell as a function of range and bandwidth.<sup>49</sup>**

$\Delta R$  is the resolution cell and  $R$  is the range to the target. For this example radar, the resolution cell is equal to 1100 m at 10 km. A laser radar (or lidar) with the same size aperture has a wavelength of 0.5  $\mu\text{m}$ , which results in a resolution cell of 1.64 cm at 10 km. It can be seen that the electro-optical (EO) systems are preferred for their target recognition and identification with high resolution, while microwave and MMW (millimeter wave) radars are preferred for their large beam widths and large area searches.

Microwave radar systems detect and track targets using two distinct principles: elapsed time between transmitted and received pulses to calculate range, and frequency shift between these pulses to calculate range rate<sup>50</sup>. The change in frequency is called the Doppler shift. To find the range, the following equation is used:

$$R = \frac{c * \text{time}}{2}$$

**Equation 56: Radar range equation**

<sup>48</sup> Hovanessian, S.A. *Introduction to Sensor Systems*. Artech House, Norwood, MA, 1988, p. 10.

<sup>49</sup> *Ibid.* p. 11.

<sup>50</sup> *Ibid.* pp. 11-12.

The time equals the elapsed time between transmitted and received pulses and the factor of two comes from the round-trip distance traveled by the pulse.

In order to calculate the velocity of the target, the signal processor determines the difference between the transmitted frequency and the returned frequency. The transmitted frequency is defined as  $f_o$  while the received waveform frequency is at  $f_o + f_d$  (where  $f_d$  is the Doppler shift). Using the target motion equation (Equation 57), the rate of change of the radar-target range,  $\dot{R}$ , can be determined. Figure 11 shows a visual example of the Doppler shift discussion.

$$f_d = \frac{2\dot{R}}{\lambda}$$

Equation 57: Target motion (range rate) equation

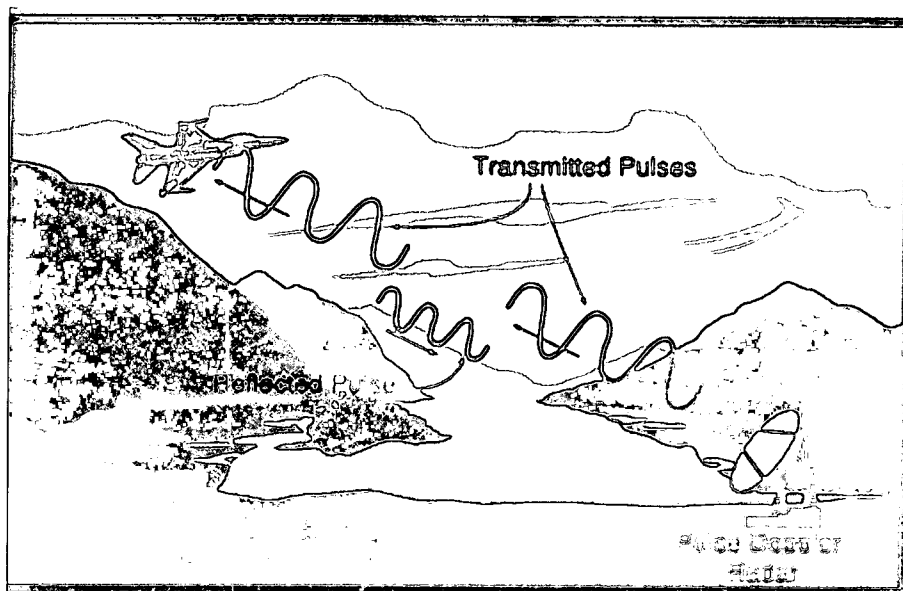
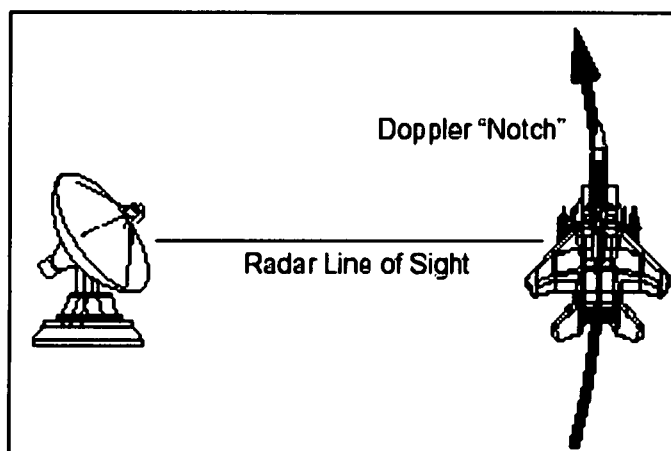


Figure 11: Example of frequency difference between transmitted pulses from a pulse Doppler radar and reflected pulses from a moving air target<sup>51</sup>.

<sup>51</sup> Younghase, John M. *Electronic Warfare Fundamentals*. SWL Inc., Vienna, VA, 1 August 1994, pp. 4-21.

The pulse Doppler radar has an Achilles heel. The radar must have the ability to filter backscatter returns (such as the ground). If the received frequency has no Doppler shift, or if the Doppler shift results in  $\dot{R}$  that is less than a pre-determined value, the return will not be displayed by the processor. For example, assume that  $\dot{R}$  must be  $> 50$  knots to be returned on the display for the user. It cannot reasonably be said that there are many flying objects of interest that have airspeeds of 50 knots or less. This is so that ground vehicles, such as cars, are not displayed on the radarscope. The pulse Doppler radar processor will be able to determine the range, aspect angle (to be defined later), heading, and airspeed of an airborne target. However, if an aircraft turns perpendicular to the radar, there is no apparent closure and the reflected waveform has no frequency shift or has a frequency shift resulting in a closure less than 50 knots (see Figure 12).



**Figure 12: The Doppler notch**

This is called the “Doppler notch” and is an effective technique to defeat airborne and ground radar systems. When a pilot flies his aircraft into “the notch”, the radar system illuminating him will typically “break lock” and/or radar guided munitions will not be able to track to the aircraft. Additionally, aircraft will essentially be “invisible” to pulse

Doppler radars while in the “notch”; however, flying exactly perpendicular to a target for long periods of time is extremely difficult.

There are volumes of information about radar sensors and the intricacies that make them operate. The information that has been presented thus far provides a framework for the upcoming discussion. New terms will be introduced when necessary. However, one more subject area should be covered: radar cross-sections and stealth.

### Radar Cross-Sections and Stealth

The very term “stealth” lends a person to think of the term “invisibility”. This is not necessarily the case in the world of radar. Stealth means that an aircraft has a low radar cross section that reduces the detection and employment range of radar sensors and their weapons. Every object in the atmosphere has a radar cross-section (RCS). Whether it is a B-52, F-16, Cessna 152, bird, bee, B-2 bomber, or natural aerosols and dust particles, a sensor can detect them all. The question is: does the radar sensor have enough power and receiver sensitivity to see them?

The concept of stealth, or low observable design, was studied by British engineers in 1941. However, it wasn't until 1943 that the Germans actually designed a low observable aircraft. A shortage in metal led Walter and Remier Horten to design an aircraft with improved performance, plus shaping and coatings that might have reduced its radar return. The Horten twin-engine flying wing bomber/reconnaissance aircraft used plywood and charcoal materials that efficiently absorbed the long centimetric wavelengths of the period<sup>52</sup>.

---

<sup>52</sup> Grant, Rebecca. *The RADAR game. Understanding Stealth and Aircraft Survivability*. IRIS Independent Research, Arlington, Virginia 1998, p. 22.



**Figure 13: The German-Horten Aircraft<sup>53</sup>**

An early prototype of the Horten aircraft crashed during landing and was destroyed. Other early production versions were finally captured when the factory was overrun by American troops in 1945. However, additional characteristics of its low observable design were discovered. Although the design characteristics were first used to reduce parasitic drag, the fact that there were no vertical surfaces on the plane, and that the cockpit and powerplants were all housed within the wing itself, aided in its low observability. Additionally, the plane was covered with plywood sandwiched around a center of charcoal that aided in its radar absorbing characteristics.

With the advent of radar-guided surface to air missiles (SAMs) in the 1960s, a large push was made to develop stealth technology. The first modern aircraft to incorporate low observable features was the SR-71. It was coated with radar absorbing materials and the flat, lateral sloped bottom of the surface reduced its radar cross-section by 90%<sup>54</sup>. In fact, the SR-71 has a lower RCS than the B-1 bomber, which was built two decades later.

---

<sup>53</sup> *Ibid.* p. 22.

<sup>54</sup> *Ibid.* p. 23.

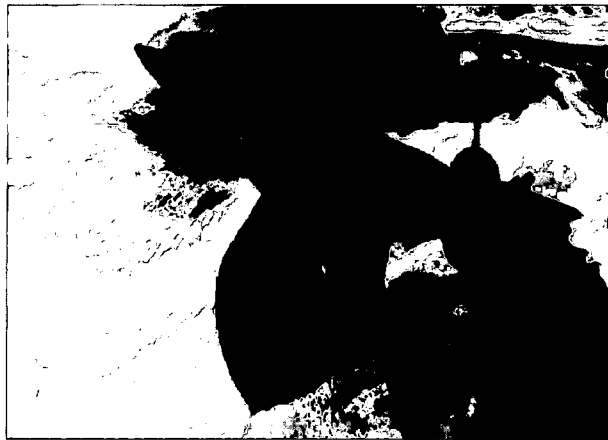


**Figure 14: SR-71: The first modern low-observable aircraft.<sup>55</sup>**

In the late 19<sup>th</sup> century, Clerk Maxwell developed equations that described the behavior of electromagnetic waves. In the 1960's, Russian scientist Pyotr Ufimtsev, built radar cross section engineering principles from the field of physical optics that estimated the type of scattered field that would be created when radar waves encountered the aircraft. The radar range equation and the equation for calculating RCS are both based upon physical optics principles<sup>56</sup>.

The sum of the major components of the aircraft's shape is defined by RCS. RCS is the area of the scattered wave field being returned to the radar. Generally, the size of the radar cross section of a conventional aircraft is much larger than the physical size of the aircraft. The RCS of an aircraft determines the amount of the sending radar's power is reflected back to the sender to receive. The RCS is typically measured in square meters, or decibels per square meter (dBSM).

---

<sup>55</sup> *Ibid.* p. 22.

<sup>56</sup> Grant, Rebecca. *The RADAR game. Understanding Stealth and Aircraft Survivability*. IRIS Independent Research, Arlington, Virginia 1998, p. 23.

## What the Radar Sees

- ▣ Radar "sees" the area defined by the returned radar waves
- ▣ This can be much larger or much smaller than the physical area
- ▣ Radar cross section reduction shrinks the size of return field
- ▣ RCS is sum of return vectors

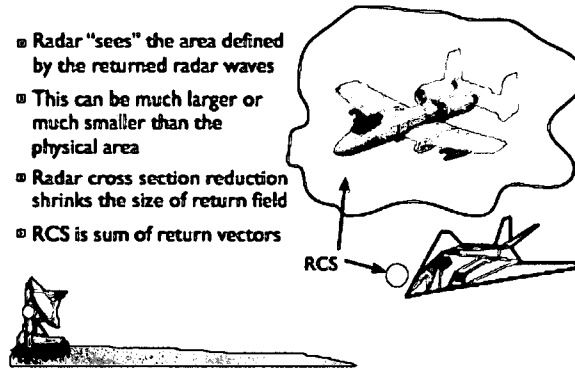


Figure 15: Basic principles of radar cross section<sup>57</sup>

There are several design techniques that reduce RCS. The first is specular reflection. Specular reflection is like a mirror. The direction of the reflected waves depends on physical laws that relate the angle the wave strikes the target to the angle at which the wave is reflected. These laws also allow different aircraft shapes to produce different radar returns. By varying the geometric shapes of aircraft, specular reflection can be reduced. The F-117 is a perfect example of a stealth design based upon specular reflection (see Figure 16.)

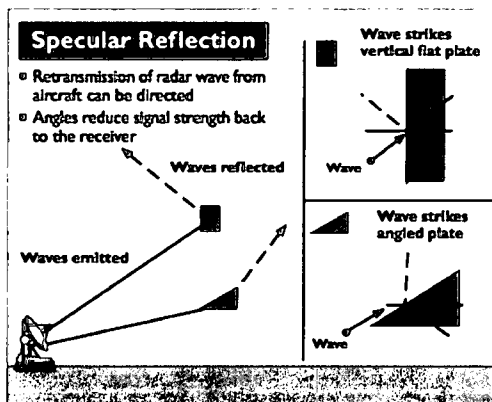


Figure 16: Specular reflection and example of an aircraft using the concept in its design (F-117)<sup>58</sup>.

<sup>57</sup> *Ibid.* p. 23.

<sup>58</sup> *Ibid.* p. 25.

RCS is also a function of the amount of diffraction on an aircraft. Diffraction occurs when waves strike a point such as a wedge or tip. The source of diffraction can be as small as the head of a screw that is not flush with the surface or covered with radar absorbing material (RAM). Diffraction can also be caused by conical points, sharp corners, and even rounded tubular surfaces. A special case of diffraction occurs inside a cavity. Waves inside a cavity like a cockpit or an engine scatter in complex patterns. Inlet covers on the F-117 help reduce this effect, and special coatings on aircraft canopies can reduce cockpit scatter. Figure 17 further explains the concept of diffraction.

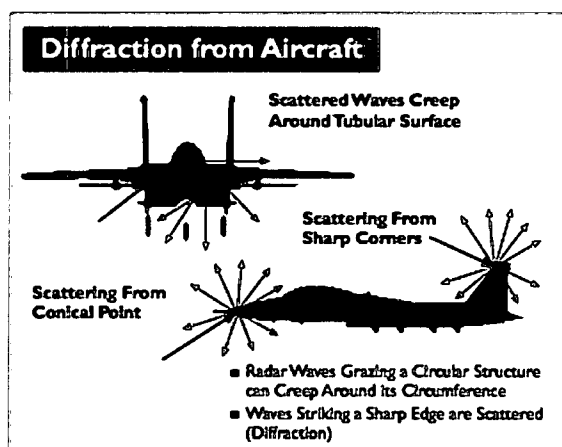


Figure 17: The concept of radar diffraction<sup>59</sup>

A final technique used to reduce RCS is radar-absorbing material (RAM). From the previous discussion, the German Horten aircraft first used a primitive RAM. German submarines in WW II used a product called *Sumpf* on their periscopes that were being detected by primitive centimeter-wave radar<sup>60</sup>. *Sumpf* consisted of a sandwich of rubber and carbon granules embedded in it. Its purpose was to absorb radar pulses, reduce the strength of the echo and make the periscope less detectable by radar. Additional

<sup>59</sup> Grant, Rebecca. *The RADAR game. Understanding Stealth and Aircraft Survivability*. IRIS Independent Research, Arlington, Virginia 1998, p. 25.

<sup>60</sup> *Ibid.* p. 26.

experiments with RAM were conducted with the U-2. The U-2 was covered with ferrite-laced paint. The concept was that the iron in the paint would change the magnetic properties of the radar waves in order to diminish return. However, the loss of radar energy was not very strong. Other types of RAM reduce radar returns through passive cancellation or impedance. RAM is used on the leading edges of wings, pylons, and control surfaces to reduce radar diffusion.

Aircraft are designed by a specified set of requirements. Most conventional fighter aircraft were not designed with low observability in mind. For example, the A-10 has a large RCS, but is well suited for the mission it was designed to perform. On the other hand, the F-117 was designed for stealth. Figure 18 shows the design features of each aircraft and how they affect RCS. Figure 19 shows the spectrum of RCS found in today's radar environment. While typical fighter jets have an RCS on the order 10-20 square meters, stealth "zone" aircraft have a RCS less than -0.1 to -0.0001 square meters. The RCS of the F-117 is about the size of a hummingbird, while the RCS of the B-2 is less than that of a bee.

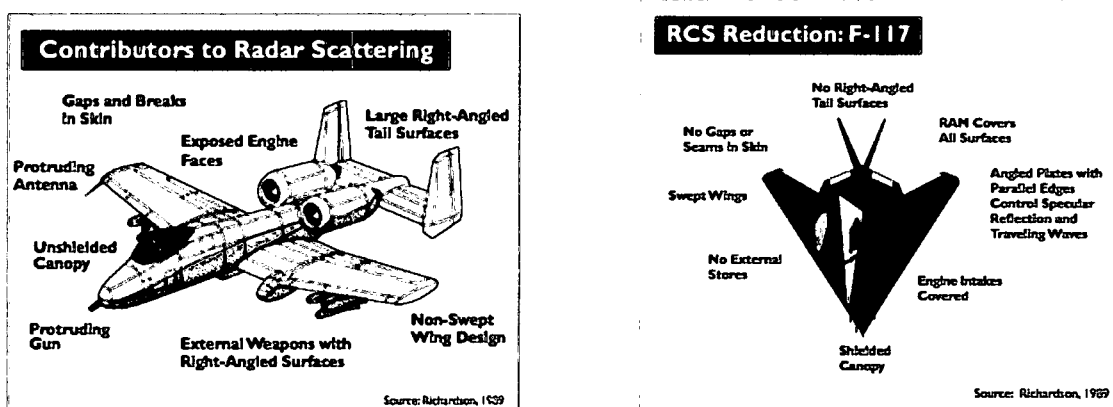


Figure 18: Differences in design between the A-10 and F-117 that effect RCS<sup>61</sup>

<sup>61</sup> *Ibid.* p. 27.

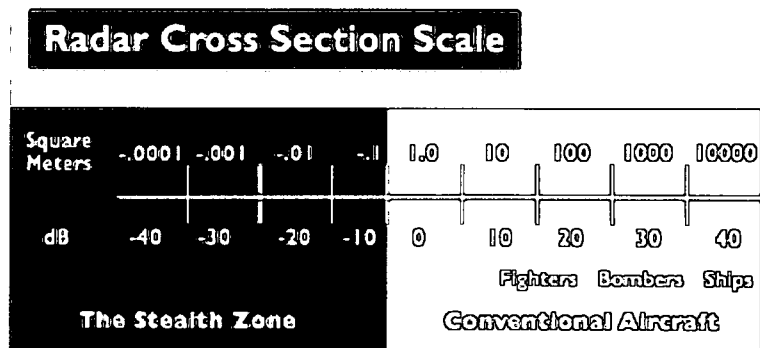


Figure 19: The radar cross-section scale<sup>62</sup>

Other considerations in stealth design are noise and infrared signature. Both noise from engine and airframes can be detected. In fact, U.S. Patent number 6,480,142, submitted by William Rubin, claims the invention of a radar system that can sense noise from aircraft airframes by the use and detection of pressure variations in the atmosphere. Minimizing infrared signatures is also important not only to defeat IR guided munitions (such as short range air-to-air missiles), but to also defeat IR detecting sensors on the ground and in the air (such as the Infrared Sensing and Targeting System, IRSTS, on the MiG-29).

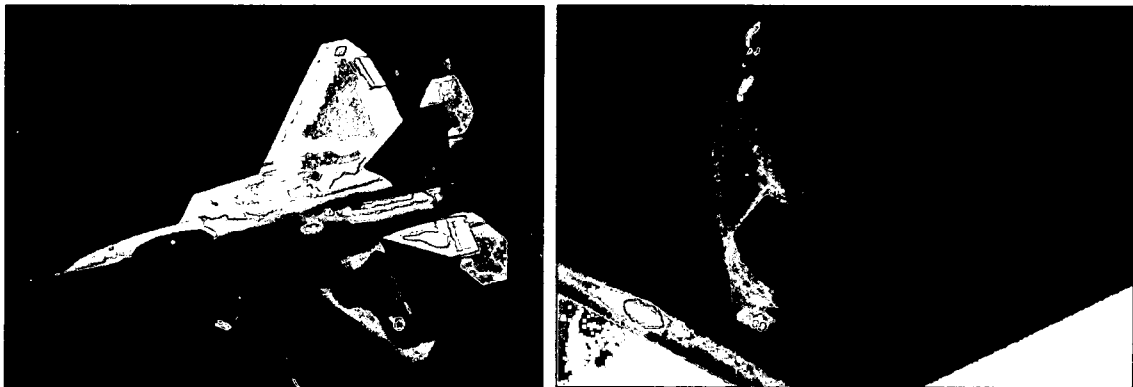


Figure 20: Examples of stealth aircraft: the F-22 Raptor and the B-2 Spirit<sup>63</sup>

<sup>62</sup> *Ibid.* p. 28.

<sup>63</sup> Grant, Rebecca. *The RADAR game. Understanding Stealth and Aircraft Survivability*. IRIS Independent Research, Arlington, Virginia 1998, pp. 28-29.

Over the last 2 decades, the U.S. Air Force has dominated stealth design. Current stealth aircraft in the U.S. inventory include the B-2, F-117, F-22, and the newly introduced F-35 Joint Strike Fighter. However, this is not stating that stealth characteristics have not been employed on other systems around the world. Current microwave radars have limited capability to detect or target low RCS targets. With the possible advent of a sensor that can detect the turbulent wakes of low observable aircraft, the detectable area of this type of wake could be on the order of a 1000 meters long and 10-100 meters wide. Not even aircraft that have reduced their noise and IR signatures will be immune to detection. As stated at the beginning of this thesis, any object that displaces a fluid will leave behind it a wake. Unless engineers are able to change the laws of physics, any type of aircraft should be detectable by this sensor (assuming the sensor is not being defeated by other types of electronic countermeasures). While this type of sensor would seem to benefit only those countries without stealth technology, it is important that the types of methods used to negate stealth design are understood. Armed with this knowledge, countries are better prepared to defend against future technologies.

#### Detection of Clear Air Turbulence by Doppler Radar

During the early stages of air travel, aircraft performance limited their maximum altitude. Strong winds and air currents in the lower layers of the atmosphere made traveling by air uncomfortable. By the mid-1950's, jet passenger aircraft with pressurized cabins allowed them to travel into higher levels of the troposphere, thus avoiding the turbulent complications of lower heights. However, it was found that high-altitude airflow also contained turbulence. While most of this turbulence was isolated

around thunderstorms, there was also turbulence in areas with no clouds. Thus, the term for turbulence in the absence of clouds was coined clear air turbulence (CAT).

In 1963, at the tenth weather radar conference for the American Meteorological Society, Smith and Rogers made one of the earliest suggestions that CAT might be detectable by radar<sup>64</sup>. Previous attempts at detecting CAT had, to various extents, failed using airborne techniques. These techniques included infrared and microwave radiometry, stellar scintillations, laser radar, electric field measurements, air temperature gradients, and VHF radar<sup>65</sup>. Smith and Rodgers made the claim that CAT could be detected by powerful installations that have receivers sensitive enough to detect weak scattering of radar waves from fluctuations in the refractive index that accompany CAT. Between the years of 1966 and 1970, many ground installations were able to prove Smith and Rodgers correct. However, up to that time, there were no airborne sensors with the ability to detect CAT.

There are several possible conditions that induce clear air turbulence, but the two most common are mountain rotors and the Kelvin-Helmholtz (KHI) instability. While mountain rotors are usually induced by terrain, KHI can happen over any terrain and is more difficult to predict. KHI occurs when the level of maximum wind shear and the vertical shear are sufficiently strong. KHI manifests itself as amplifying waves that are oriented perpendicularly to the shear vector and eventually “break” into turbulent flow on a range of smaller scales<sup>66</sup>. The onset of KHI over the entire depth of an atmospheric

---

<sup>64</sup> Smith, P.L. and Rogers R.R. 1963: *Proc. Tenth Weather Radar Conference, Am. Metro. Soc.*, Boston, p. 316.

<sup>65</sup> Watkins, C.D, and Browning, K.A. 1973: The detection of clear air turbulence by radar. *Physics in Technology*. 4. p. 30.

<sup>66</sup> *Ibid.* p. 31.

layer of thickness  $\Delta z$  is determined by the value of the Layer Richardson Number,  $Ri(\Delta z)$ , given by:

$$Ri(\Delta z) = \frac{g}{\bar{\theta}} \left( \frac{\Delta \theta}{\Delta z} \right) / \left( \frac{\Delta V}{\Delta z} \right)^2$$

**Equation 58: Equation for the Layer Richardson Number**

In Equation 58,  $\Delta V$  and  $\Delta \theta$  are the magnitude of the vector of wind shear and increment of potential temperature over the depth  $\Delta z$  and the mean potential temperature  $\bar{\theta}$ . The variable  $g$  is the acceleration due to gravity. The quantity  $(1/\bar{\theta})(\Delta \theta/\Delta z)$  represents the static stability of the layer. Theoretical and experimental studies indicate that KHI does not occur until  $Ri$  drops below the critical value of 0.25.<sup>67</sup> Intense CAT occurs in association with large-amplitude KH billows when  $Ri$  drops below 0.25 over a deep and strongly sheared layer of high static stability. During the growth of large billows, secondary billows of much smaller amplitude develop within the large billows in places where the distortion of the flow pattern leads to a further reduction in  $Ri$ . The radar is then able to detect the small secondary billows and uses them as tracers to determine the large-amplitude billows responsible for CAT.

When the Kelvin-Helmholtz billows break it may be considered, as a first approximation, that the flow has degenerated locally into homogeneous isotropic turbulence<sup>68</sup>. The turbulent energy of the KH billow then cascades from larger to smaller scales as described in Chapter 1. Obviously, from the Chapter 1 discussion about turbulent scales, the smallest scale will be the Kolmogorov scale. In CAT, the Kolmogorov scale,  $\eta$ , is on the order of 10 mm and 6 mm in the case of weak and severe

---

<sup>67</sup> *Ibid.* p .31.

<sup>68</sup> Watkins, C.D, and Browning, K.A. 1973: The detection of clear air turbulence by radar. *Physics in Technology*. 4. p. 31.

turbulence, respectively<sup>69</sup>. The integral scale,  $\ell$ , is the amplitude of the KH billows. The one dimensional energy spectrum of the velocity perturbations within the inertial range is given by:

$$E(k) = A\varepsilon^{2/3}k^{-5/3}$$

**Equation 59: Equation of one-dimensional energy spectrum of Kelvin-Helmoltz Instability<sup>70</sup>**

In Equation 59,  $\varepsilon$  is the rate of turbulent energy dissipation (as defined in Chapter 1) with units of  $\text{m}^2\text{s}^{-3}$ .  $k$  (with units of  $\text{m}^{-1}$ ) is the wavenumber corresponding to the scale  $\ell = 2\pi/k$ .  $A$  is a constant, presumably on the order of 1.

A radio wave propagating through a medium that has a non-uniform refractive index will suffer some loss of energy away from the direction of propagation. The Earth's atmosphere is far from uniform and thus, in addition to refraction, both partial reflection and scattering of radio waves are possible under the appropriate conditions. Bean and Dutton give the refractive index of air for radio waves as:

$$n = 1 + \frac{77.6}{T} \left( p + \frac{4810e}{T} \right) \times 10^{-6}$$

**Equation 60: Equation for the refractive index of air<sup>71</sup>**

In Equation 60,  $T$  is the temperature in degrees  $K$ ,  $p$  is the pressure in millibars, and  $e$  is the water vapor pressure in millibars. For convenience, the term refractivity can be used and is defined as:

$$N = (n - 1) \times 10^6$$

**Equation 61: Definition of refractivity<sup>72</sup>**

---

<sup>69</sup> *Ibid.* p. 34.

<sup>70</sup> *Ibid.* p. 32.

<sup>71</sup> Bean, B.R. and Dutton, E.J. 1966 *Radio Meteorology* NBS Monograph 92, US Government Printing Office, Washington, D.C.

<sup>72</sup> Watkins, C.D. and Browning, K.A. 1973: The detection of clear air turbulence by radar. *Physics in Technology*. 4. p. 30.

Typical values of refractivity would be  $N \approx 350$  at the surface and  $N \approx 90$  at the height of 10 km<sup>73</sup>. Because refractivity changes as a function of height, the following relationship allows us to compensate:

$$\Delta n = (a\Delta T + b\Delta e + c\Delta p) \times 10^{-6}$$

**Equation 62: Equation of the refractive index<sup>74</sup>**

Where a, b, and c are functions of height and are given in Table 1.

**Table 1.**

|             |    | <i>a</i> | <i>b</i> | <i>c</i> |
|-------------|----|----------|----------|----------|
| Height (km) | 0  | -1.3     | 4.5      | 0.27     |
|             | 10 | -0.5     | 7.5      | 0.30     |
|             | 20 | -0.1     | 8.0      | 0.35     |

**Table 1: Coefficients of the refractive index as a function of height<sup>75</sup>**

In addition to the refractive index, the scattering volume of air is also a function of the reflectivity (denoted  $\eta_R$ ). Megaw gave the reflectivity of a refractively turbulent medium in 1957<sup>76</sup>.

$$\eta_R = \frac{\pi}{8} \overline{(\Delta n)^2} k^2 F_n(K) \sin^2 \beta \sin^{-4}(\gamma/2)$$

**Equation 63: Megaw's equation for the reflectivity of a refractively turbulent medium**

In Equation 63,  $\overline{(\Delta n)^2}$  is the mean square fluctuation of the refractive index,  $\beta$  is the angle between the direction of the receiver and that of the electric field of the transmitted wave,  $k$  is the wavenumber,  $F_n(k)$  is the one dimensional spectral density of  $\overline{(\Delta n)^2}$  in terms of  $k$ , and  $\gamma$  is the angle between the directions of the incident and scattered waves<sup>77</sup>.

<sup>73</sup> *Ibid.* p. 32.

<sup>74</sup> Bean, B.R. and Dutton, E.J. 1966 *Radio Meteorology* NBS Monograph 92, US Government Printing Office, Washington, D.C.

<sup>75</sup> *Ibid.* p. 32.

<sup>76</sup> Megaw, E.C.S. 1957. *Proc. Inst. Elec. Eng.* 104C. p. 441.

<sup>77</sup> Watkins, C.D. and Browning, K.A. 1973: The detection of clear air turbulence by radar. *Physics in Technology*. 4. p. 30.

The most difficult part of Equation 63 is determining the value of  $F_n(k)$ . However, many well-known turbulent theorists such as Kolmogorov, Batchelor, Silverman, and Tatarski developed the relationship for  $F_n(k)$ :

$$F_n(k) = \frac{2}{3} k_o^{2/3} k^{-5/3}$$

**Equation 64: Equation for the auto-correlation function<sup>78</sup>**

Where  $k_o = 2\pi/\ell$ . This relation has been tested experimentally with excellent results.

The mean-square fluctuation of the refractive index is related to the integral scale:

$$\overline{(\Delta n)^2} = 0.19 \ell^{2/3} C_n^2$$

**Equation 65: Equation for the mean-square fluctuation of the refractive index**

By using Equation 65, Equation 64, and Equation 63, terms can be substituted and a relation is created that is the backbone of the radar detection of turbulence: Tatarski's theory.

$$\eta_R = 0.38 C_n^2 \lambda^{-1/3}$$

**Equation 66: Tatarski's theory of reflectivity of a refractively turbulent medium**

The value of  $\eta_R$  is also the radar cross-section per unit volume of isotropic turbulence in the inertial range<sup>79</sup>.

The last step of the process is to determine the value of the coefficient  $C_n^2$ . This coefficient is called the turbulence parameter. It is also known as the turbulence intensity. Therefore, the reflectivity of the atmosphere is a function of turbulence.  $C_n^2$  is defined as:

---

<sup>78</sup> *Ibid.* p. 34.

<sup>79</sup> Shariff, Karim and Wray, Alan. 2002: Analysis of the radar reflectivity of aircraft vortex wakes. *Journal of Fluid Mechanics*. 463 p 124.

$$C_n^2 = a^2 \varepsilon^{2/3} \left( \frac{dn}{dz} \right)^2 \left( \frac{d\bar{u}}{dz} \right)^{-2}$$

**Equation 67: Equation for the turbulence parameter<sup>80</sup>**

In Equation 67,  $\left( \frac{dn}{dz} \right)$  is the mean vertical gradient of the potential refractive index, and

$\left( \frac{d\bar{u}}{dz} \right)$  is the vertical gradient of the mean horizontal wind. The coefficient  $a^2$  is non-

dimensional constant. The key value in this equation is that of the turbulent dissipation rate,  $\varepsilon$ . Determining the value of  $C_n^2$  is not an arbitrary process. In fact, several technical papers have been written to describe various ways to find the value of  $C_n^2$ . However, those discussions go beyond the scope of this thesis. The important point to be made in this discussion is that the measurement of the reflection and refraction of radio waves in the atmosphere can be used to find the value of the turbulent dissipation rate.

Experimentation with radars detecting CAT has been accomplished since the 1960's. Figure 21 shows an example of a radar return of Kelvin-Helmholtz billows. This is a radar return from actual clear air turbulence occurring in the atmosphere on 13 April 1970.

---

<sup>80</sup> Watkins, C.D, and Browning, K.A. 1973: The detection of clear air turbulence by radar. *Physics in Technology*. 4. p. 34.

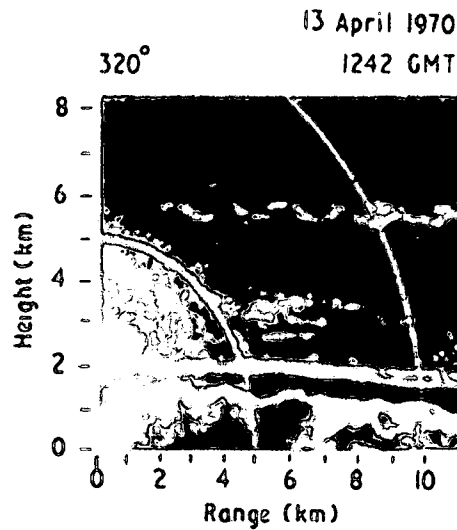


**Figure 21: Photograph of Kelvin-Helmholtz billows between 5-6 km in altitude using a pulse Doppler radar<sup>81</sup>**

Meteorologists have been using this technology to determine turbulent dissipation rates and mixing efficiencies in the atmosphere.

Research has been conducted privately and through the government to use radar technology to detect the turbulence caused by aircraft wakes. This research stemmed from concerns of wake turbulence from large aircraft causing accidents to aircraft following them on takeoff and landing at airports. By detecting these aircraft wakes, radio warnings could be issued to aircraft that would be affected.

Experiments in this area have been conducted for decades. In 1980, Noonkester and Richter were able to detect wakes of departing aircraft using radar at a frequency of 3 GHz, at a range of 100-300 m<sup>82</sup>. In 1984, Chadwick, using a similar radar, was able to detect the wake turbulence of arriving and departing aircraft using a 200 W radar and a

<sup>81</sup> *Ibid.* p. 52.

<sup>82</sup> Noonkester, V.R. and Richter, J.H. 198. FM-CW radar sensing of the lower atmosphere. *Radio Sci.* 15, pp. 337-353.

8 ft diameter dish at ranges less than or equal to 1 km<sup>83</sup>. In 1994, Nespor detected vortices of small fighter aircraft in approach configuration using a 1 MW pulse Doppler radar with a frequency of 5.6 GHz at ranges of approximately 2.7 km<sup>84</sup>. Gilson, from the Lincoln Laboratory, conducted the best-documented and controlled experiment at Kwajalein atoll in 1992. The RCS of the wake of a C-5A was measured at a range of 15 km using a powerful pulse Doppler radar having 2-7 MW of peak power<sup>85</sup>.

The National Aeronautics and Space Administration (NASA) has been experimenting with the detection of aircraft vortices for some time. They have used both radar detection techniques and Doppler lidar (Laser Detection and Ranging) using infrared frequencies. While Doppler radar has had some success in the detection of turbulent aircraft wakes, Doppler lidar is the more mature of the two detection methods and will be described in the next section.

#### Detection of Clear Air Turbulence by Doppler Lidar

The underlying principle of pulsed Doppler lidar measurement of wind and aerosols is the use of optical heterodyne (coherent) detection, in which laser pulses are transmitted into the atmosphere and scattered off of naturally-occurring small dust particles (aerosols) entrained in the ambient flow. In 1997-1998, NASA conducted airborne experiments with the Lockheed L-118C Electra aircraft and with the SR-71 research aircraft. On each airborne platform, a lidar sensor was configured to detect CAT in the atmosphere ahead of the aircraft.

---

<sup>83</sup> Chadwick, R. B., Jordan, J. and Detman, T. 1984 Radar cross section measurements of wingtip vortices. *Proc. ESA IGARSS 1984*, vol. 1, pp. 479-483.

<sup>84</sup> Nespor, J., Hudson, E., Stegall, R., and Freedman, J. 1994 Doppler radar detection of vortex hazard indicators. *NASA Conf. Proc. CP-10139*, Part 2, pp. 651-688.

<sup>85</sup> Gilson, W.H. 1994 Aircraft wake RCS measurement. *NASA Contractor Rep. 10139*, Part 2, pp. 603-623.

Radars and lidars can be categorized according to their wavelengths. Doppler radars with wavelengths ranging from 3 cm to 10 cm can detect the motion of rain, snow, pollens, and insects. They require the presence of a target and cannot detect clear air. Doppler radars with wavelengths of 30 cm to 6 m are called UHF (ultrahigh frequency) and VHF (very high frequency) radars. The radars described in the previous section belong to this category and can detect refractive index fluctuations arising from turbulent mixing of temperature and moisture in the clean air. Pulse Doppler lidars have wavelengths below 10  $\mu\text{m}$  and can detect the motion of aerosol particles. Doppler lidar uses the same principles as Doppler radar using shorter wavelengths so smaller aerosols and be used to trace the wind. Wind speed is relatively small in the atmosphere so the corresponding Doppler shift will also be small. Through the use of heterodyne detection, there is a mixing of a weak returned signal with a stronger signal close to that of the returned signal. The difference in the two frequencies should be low enough that it can be separated from the original source frequency (see Figure 22).

Lidar sensors only measure the velocity of the radial component of the aerosols. However, in order to determine the values of the turbulent velocity fluctuations, the streamwise and vertical component of velocity must be known as a minimum. Lidars use a technique where measurements are made at a given range and angle ( $\theta/2$ ) above and below the flight path of the sensor aircraft. The radial velocity is measured along the lidar beam and is given by:

$$V_{\text{radial}} = V_x \cos\left(\frac{\theta}{2}\right) - V_z \sin\left(\frac{\theta}{2}\right)$$

**Equation 68: Equation for the components of radial velocity**

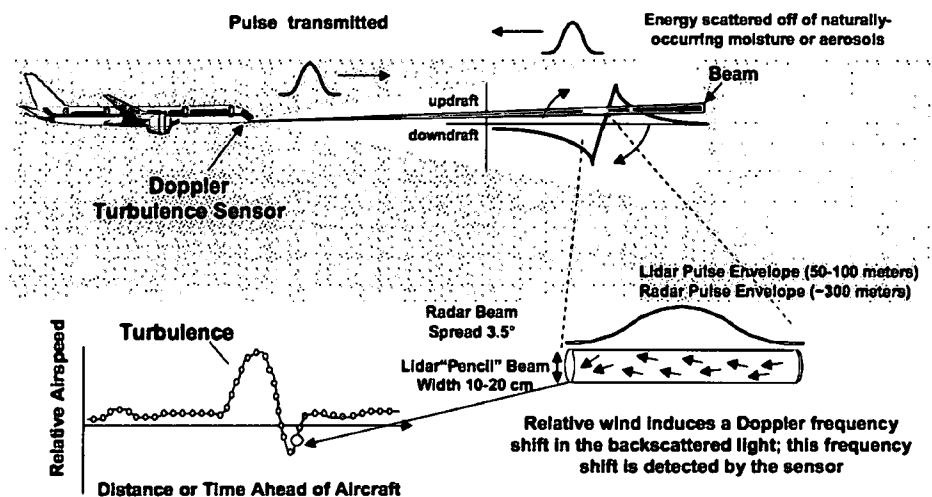


Figure 22: Basic principles of lidar use to detect CAT<sup>86</sup>

Where  $V_z$  is the  $z$  or vertical component of the air velocity (in the Chapter 1 discussion, this would be considered  $u_2$ ) and  $V_x$  is the  $x$  or axial component of velocity (or  $u_1$  in the Chapter 1 discussion).  $\theta$  is the angle between the two lidar beams (see Figure 23).

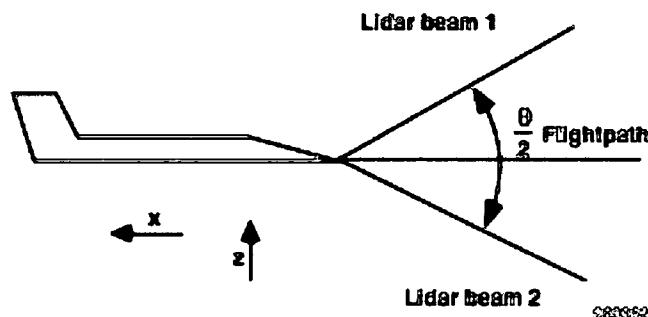


Figure 23: Configuration for lidar measurement of vertical velocity<sup>87</sup>

If two radial velocity measurements are made above and below the flightpath ( $V_1$  and  $V_2$ ) then these simultaneous equations can be solved for  $V_z$  using the system of equations defined by:

<sup>86</sup> Soreide, D., Bouge, R., Ehernberger, L.J., Bagley, H. 1996. Coherent Lidar Turbulent Measurement for Gust Load Alleviation. *NASA Technical Memo. 104318*. p. 2.

<sup>87</sup> *Ibid.* p. 8.

$$V_z = \frac{V_1 - V_2}{2 \sin\left(\frac{\theta}{2}\right)}$$

**Equation 69: Equation for the vertical component of velocity using two separate lidar measurements**

By knowing the magnitude of horizontal and vertical velocities of turbulence in clear air, and the spatial locations of those quantities, the Reynolds stress and mean strain of the flow can be determined. With these values, the turbulent energy production and dissipation of the turbulent flow can be calculated. In addition, lidar can measure the streamwise component of a turbulent wake and determine the momentum defect of a turbulent generator (i.e. an aircraft).

## CHAPTER 3: PRACTICAL APPLICATION OF TURBULENT WAKE DETECTION

Chapter 3 will take a unique approach in describing a practical application where airborne radar capable of detecting and identifying aircraft turbulent wakes may be used. In the following paragraphs, three players will be introduced. The first will be the ground control intercept (GCI) radar controller with callsign "Darkstar". The GCI provides long-range radar pictures to airborne fighter-intercept aircraft and can often direct fighter intercepts using "close" control. GCI is also equipped with IFF (Identification Friend or Foe) interrogators that can communicate with corresponding IFF systems on board aircraft to determine their friendly or hostile status. In this scenario, Darkstar utilizes a standard pulse Doppler radar that can be defeated using stealth technology. The airborne equivalent of a GCI would be the Airborne Warning and Control System (AWACS). The "blue-air" or friendly airborne aircraft in this scenario is a F-16 Block 50 with callsign "Viper 1". He carries a notional APG-68 version X radar that has the capability of detecting turbulent wakes using pulse Doppler radar.

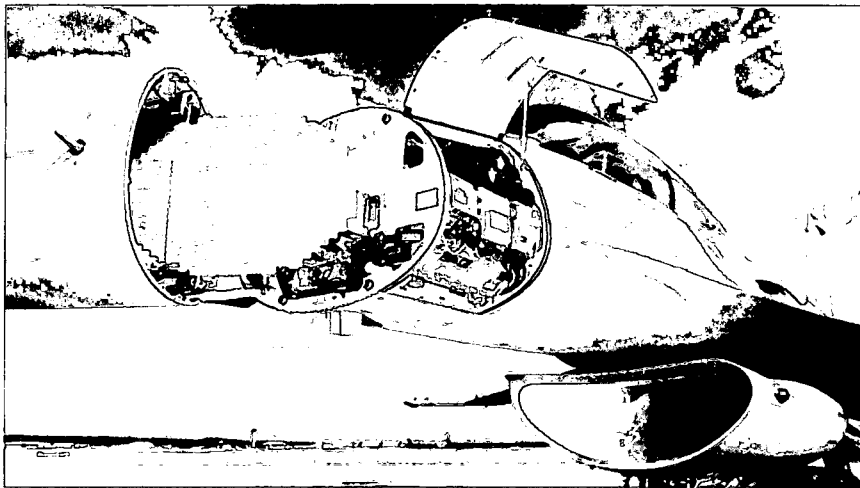


**Figure 24: Picture of an actual APG-68 v9 radar. A notional APG-68 radar capable of detecting turbulent wakes may look similar.**

The third player in the scenario is a notional “red-air” or enemy aircraft from a known hostile country. The aircraft in this scenario will be a developmental, low-observable F-18 Hornet. Based on the real-world geometry of the F-18, it would be difficult to make it a low-observable aircraft, but for the sake of demonstration, it will be assumed that this experimental F-18 has the same RCS as a B-2 stealth bomber (less than  $-0.0001$  dBS).

The blue-air F-16 will be described with two different types of configurations. The first configuration will be with a stand-alone APG-68 radar that has the capability to detect turbulence from aircraft wakes and identify the aircraft through the use of the Reynolds stress model. By using refractive and reflective indexes, the turbulent dissipation of the aircraft wake can be measured. The advantage of using the pulse Doppler radar for both detection and identification is that the microwave frequencies used are less susceptible to interference from adverse weather (such as clouds, rain, etc.). The second configuration will be similar to that used on the MiG-29 IRSTS (Infrared Sensor

and Targeting System, see Figure 25). In this configuration, the F-16 will have an APG-68 radar used for target detection and a lidar turret just below the canopy to be used for target identification. The lidar will be used to directly measure the vertical and horizontal velocity of the aerosol particles in the turbulent wake, thus allowing a direct measurement of the momentum defect of the flow. This measurement, when compared to the self-propelled momentum defect model, will allow identification of the aircraft based on a function of its Mach number and coefficient of drag. The large advantage in using lidar technology is that it is a more mature technology compared to pulse Doppler radar techniques.

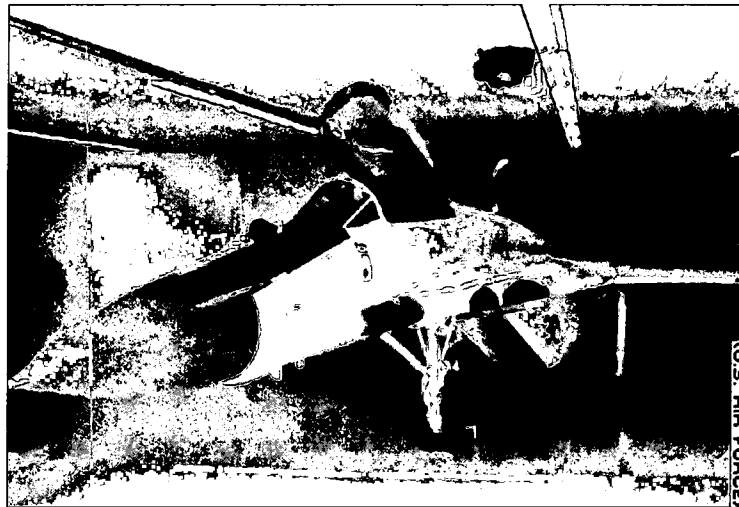


**Figure 25: MiG-29 with Slotback radar (not seen because it is within the nose radome) and IRSTS that is shown as a black protrusion just below the front of the canopy.**

### Preflight

Before the intercept can be described, it is important to introduce some of the mechanisms that will allow this mission to be a success. First, the avionics displays being used need to be described. The radar display of the F-16 is called a B-scope. In

this type of scope, the typical polar coordinate system (bearing and range) of a radar system is converted into an x-y coordinate display. Thus, the entire bottom of the radarscope is considered the origin (the ownship aircraft). A target that is on a collision course (also known as an “aware” target) will proceed straight down the scope. A target that maintains its heading, while the ownship aircraft maneuvers around it (also known as an “unaware” target) will indicate a J-hook pattern off the scope as the radar reaches its gimbal limits. Gimbal limit is defined as the maximum left, right, up, and down look angles of the radar. Figure 26 shows an example of the F-16 radar display. Across the top of the display are indications about what mode the radar is operating. This is not important to this discussion. The next row across the top of the display indicates, in order, the aspect angle (in this case 15L indicates 150 degrees left aspect), heading of the bugged target (in this case 210 degrees), airspeed of the target (540 nm/hr or 540 knots), and the closure rate between the target aircraft and the ownship (900 knots). On the left

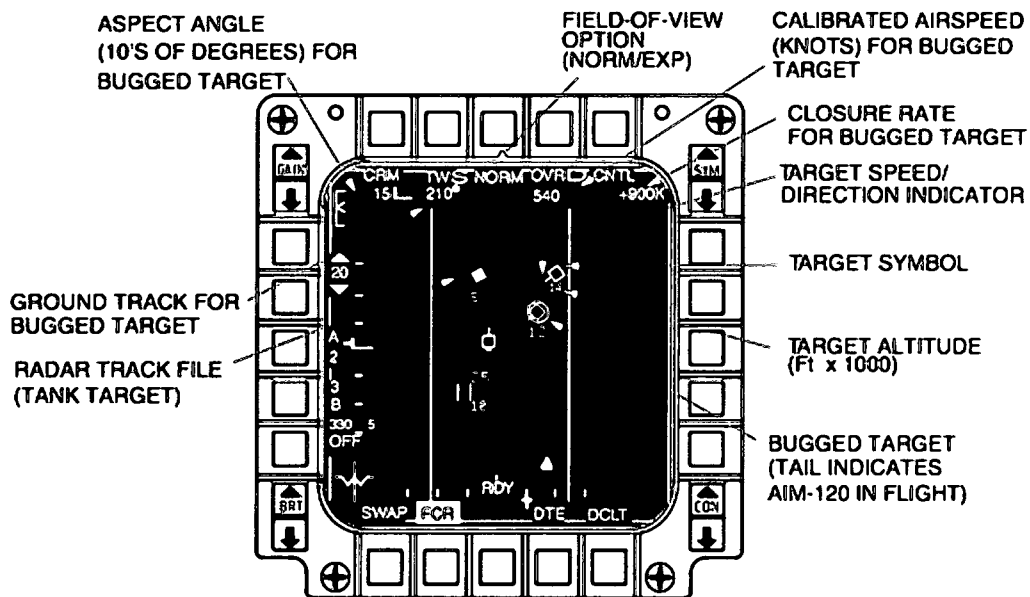


Figure 26: Example of F-16 radar display

side of the display indicates the range of the scope (20 nautical miles) and additional indications showing the scan azimuth of the radar antenna and the scan pattern (in this case 20 degree azimuth and 3-bar scan).

Aircraft are able to navigate using a combination of ring laser gyros called an Inertial Navigation System (INS). An INS system is initialized based on a known latitude and longitude position (this would be the lat/long of where the aircraft is started; the hangar, ramp, shelter, etc.). Based on the movement of the aircraft, the gyros in the INS move and give the system a constant calculation of the aircraft's exact latitude, longitude, groundspeed, and heading. INS systems also have the ability to determine in-flight windspeeds by calculating the drift of an aircraft caused by winds aloft. INS systems have a tendency to drift due to friction in mechanical parts. Since the advent of GPS in the 1990's, current INS systems are updated through the use of GPS filters. The GPS system checks the INS and determines if the delta between the two is sufficiently large. If it is, the GPS forces the INS into agreement allowing the system to continually update and give an accurate position.

The term "bullseye" defines a bearing and range from a known latitude and longitude position (called a steerpoint). The steerpoint assigned as a bullseye is usually a prominent landmark or structure (such as a lake, mountain, airfield, etc.). A steerpoint is assigned as a "bullseye" in the aircraft's INS. GCI and fighter aircraft use bullseye to describe the location of radar contacts. For example, the following statement, "Viper 1, picture, single group bullseye 210, 10, 25 thousand, bogey", means Viper 1 has an single unknown radar contact bearing 210 degrees and 10 nautical miles from the bullseye steerpoint at 25,000' MSL.

On Figure 26, the cursors on the scope are shown as two parallel vertical lines (in the figure they are currently just left of center in azimuth and at a range of about 7 nm). On the right hand side of the cursor is a set of two numbers. These numbers indicate the upper and lower level of radar beam coverage at the range of the cursors (in this case the upper limit is 25,000' MSL and the lower limit is 10,000' MSL. Anything outside of these altitudes will not be seen on the radar). These numbers are determined by the vertical beamwidth of the radar. The cursors are slewed using the cursor control on the throttle (see Figure 27). The altitude coverage of the radar beam can be controlled using the antenna elevation on the throttle.

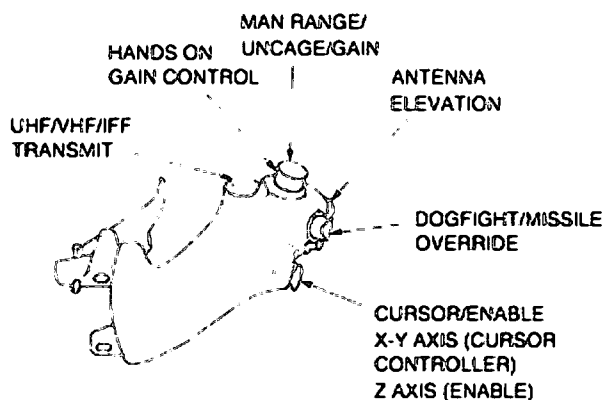


**Figure 27: Hands on controls of the F-16 throttle**

When the cursors are moved over a symbol of interest on the radar screen, the symbol's bullseye position will be located on the bottom left of the radar scope. This allows the pilot to positively ensure that the bullseye position called out by GCI is correlated to the radar target he is seeing in his cockpit. In Figure 26, the cursors are sitting at bullseye 330 degrees for 5 nautical miles.

When the radar starts to display radar tracks, they will be shown as yellow squares (Also known as tanks. They are so called because they are colored yellow with a little line indicating the direction of movement; making them look like tanks. Reference Figure 26). To target a radar track, the pilot moves the cursors over the track of interest and pushes forward the TMS (Target Management Switch). The TMS switch can be moved forward, aft, left, and right, and is located on the stick of the aircraft (see Figure 28). To “bug” a target, the cursor is placed over a selected target and the TMS switch is again pushed forward (or the cursors could be placed over a tank track and a double TMS forward accomplished). A bugged target looks like an open square with a circle around it and a small line protruding in the direction of movement. Only aspect, heading, airspeed, and closure information is displayed from the bugged target. In addition, the bugged target is the contact that will be shot with a missile if so consented by the pilot. Bugged targets can be switched by moving the TMS switch right. By doing this, target symbols can be stepped through individually to display a new bugged target.

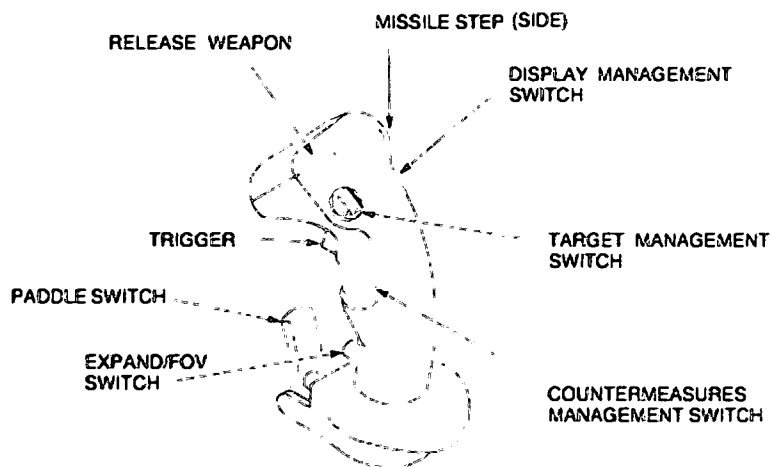


**Figure 28: Hands on controls of F-16 stick**

Now that the avionics displays have been introduced, the information that makes turbulent wake detection possible must be understood. First, a database of aircraft information must be created. In the United States Air Force, this type of information is usually obtained from the National Air and Space Intelligence Center at Wright-Patterson AFB, Ohio. This turbulent wake detection database (TWDD) would have to contain drag coefficients as a function of Mach number for all the world's aircraft. In this example, only unclassified drag information for the F-16, F-15, F-18, and B-52 has been obtained. As a result, the database in this thesis will be a small representation of the information required. Next, the radar range gate information must be defined. The radar range gate is defined as a radar sample set at a pre-defined range. Because this radar is being used to detect *and* identify, the radar must take a turbulent flow sample at a pre-determined distance from the main target. From the research presented in this thesis, it can be assumed that turbulent wakes less than 40 body lengths from the turbulent generator are fully self-preserved; thus maintaining their individual identity as a function of the generator. In this example, a range gate 5 body lengths from the leading main turbulent disturbance will be defined. However, since the body length of the turbulent generator (i.e. the aircraft) is not known, the types of targets that may be encountered on this mission must be categorized.

In order to determine a good estimate for a range gate, a quick sensitivity analysis must be made on the varying body lengths of aircraft that could be encountered in flight. For this example, three target size categories will be created called fighter, bomber, and transport. This could be selected under the radar control page. The selection made for a particular mission would depend on the types of targets most likely to be encountered that

day. A fourth category called 'unknown' could be added if the pilot was unsure of the type of aircraft he would be flying against on that mission. This category would take range gate samples from all three aircraft size categories. Obviously, this type of sampling would take more time and processing power.

| Fighter Aircraft Type | Length (ft) | Average fighter length ( $\Delta x_f$ ) |
|-----------------------|-------------|---|
| F-16                  | 49          | 58.5 ft                                 |
| F-15                  | 60          |   |
| F-18                  | 63          |   |
| F-22                  | 62          |   |

**Table 2: Table of fighter aircraft lengths and resulting average fighter aircraft length**

| Bomber Aircraft Type | Length (ft) | Average bomber length ( $\Delta x_b$ ) |
|----------------------|-------------|--|
| B-1                  | 146         | 124.7 ft                               |
| B-2                  | 69          |  |
| B-52                 | 159         |  |

**Table 3: Table of bomber aircraft lengths and resulting average bomber aircraft length**

| Transport Aircraft Type | Length (ft) | Average bomber length ( $\Delta x_b$ ) |
|-------------------------|-------------|--|
| C-5                     | 247         | 183 ft                                 |
| C-141                   | 168         |  |
| KC-135                  | 136         |  |
| KC-10                   | 181         |  |

**Table 4: Table of transport aircraft lengths and resulting average transport aircraft length**

Referencing Table 2, Table 3, and Table 4, a sensitivity analysis has been completed on a small sample of aircraft. Realistically, this type of sensitivity analysis would be done for all aircraft types throughout the world. However, for the purposes of this exercise, only the aircraft listed here have been evaluated. In addition, a database would be created to determine the coefficient of lift and drag for these aircraft as a function of Mach number, altitude, temperature, and atmospheric density. Temperature, atmospheric density, and altitude of the ownship and target can be measured directly using onboard sensors (such as the radar and exterior probes). Standard lapse rates can be used to determine the values of temperature and density at altitudes not co-located with the ownship aircraft.

For the purposes of this exercise, the coefficient of lift has been calculated for an aircraft traveling at  $M=0.85$  at an altitude of 20,000' MSL. The standard temperature, density, and kinematic viscosity were used for this calculation (see Table 5). At these conditions,  $M=0.85$  results in an airspeed of 881.31 feet per second. In addition, the aircraft weight has been determined to be 85% of the aircraft's maximum takeoff weight. Since lift will equal weight for a non-maneuvering aircraft, the coefficient of lift has been calculated using the simple equation  $C_L=L/qS$ . The resulting coefficient of drag was determined using the unclassified tables and graphs located in the appendices. The momentum thickness of the aircraft was determined using Equation 47, where the variable  $d$  is equal to the wingspan of the aircraft in feet. Only information for the F-16, F-15, F-18, and B-52 is shown since this was the only unclassified data obtained for this thesis. The resulting calculations are shown in Table 6.

| Atmospheric Conditions at 20,000' MSL (Standard Temperature and Pressure) |                                |
|---|--------------------------------|
| Density ( $\rho$ )  | 0.001226 slugs/ft <sup>3</sup> |
| Temperature (degrees F)   | -12.3232 degrees F             |
| Kinematic viscosity ( $\nu$ ) at temp. shown                              | 1.24 e -4 ft <sup>2</sup> /s   |
| M = 1   | 1036.845 fps                   |
| M = 1   | 614.314 nm/hr                  |

**Table 5: Atmospheric conditions at 20,000' MSL**

| Type A/C | T/O Weight (lbs) | Cruise Weight (lbs) | S (ft <sup>2</sup> ) | Wingspan (ft) | Mach | Airspeed (fps) | C <sub>L</sub> | C <sub>D</sub> | $\theta$ (ft) |
|----------|------------------|---------------------|----------------------|---------------|------|----------------|----------------|----------------|---------------|
| F-16     | 37,500           | 31,875              | 303.83               | 34            | 0.85 | 881.318        | 0.220          | 0.026          | 0.439         |
| F-18     | 65,800           | 55,930              | 405.11               | 45            | 0.85 | 881.318        | 0.290          | 0.032          | 0.730         |
| F-15     | 68,000           | 57,800              | 615.29               | 42            | 0.85 | 881.318        | 0.197          | 0.026          | 0.536         |
| B-52     | 488,000          | 414,800             | 4051.08              | 185           | 0.85 | 881.318        | 0.215          | 0.022          | 2.044         |

**Table 6: Calculated aerodynamic parameters for F-16, F-18, F-15, and B-52<sup>88</sup>**

From the information gathered from the “mini” database contained in Table 6, the turbulent models for the self-propelled momentum defect and the Reynolds stress profiles can be built. First, the Reynolds stress profile will be discussed. If Equation 47 is referenced, the relations to determine the half-width and mean velocity of the turbulent wake as a function of momentum thickness and downstream distance can be found. The downstream distance that will be measured is equal to 5 times the average aircraft length as determined by the fighter, bomber, or transport category (reference Table 2, Table 3, and Table 4). The momentum thickness for each aircraft is shown in Table 6. The model for the Reynolds stress profile is shown in Equation 52. In order to build this model, the coefficients  $A$  and  $L_o'$  must be calculated. From the discussion on page 55,  $A$  is proportional to  $\nu_T U_o$ . In addition,  $\nu_T$  can be found using the relation  $\frac{\nu_T}{\nu} = c_1 R_\ell$  where  $c_1$

<sup>88</sup> Example calculations of this table can be found in APPENDIX 9: CHAPTER 3 SAMPLE CALCULATIONS

is on the order of 1. Finally,  $L_o'$  is proportional to the half-width of the turbulent wake  $L_o$ .

Using these tools, aircraft information can be applied to perform calculations. In order to find  $R_\ell$ , some assumptions must be made. The integral scale  $\ell$  is approximately  $\frac{1}{4}$  of  $L_o$ <sup>89</sup>. The integral scale is determined using the wake width near the aircraft. In addition, the instantaneous velocity used to calculate  $R_\ell$  can be approximated using 3-5 % of the mean velocity  $U_o$ <sup>90</sup>. The instantaneous velocity used to calculate  $R_\ell$  is dependent on the mean velocity at a given position downstream (in this case, 5 category lengths downstream).

| Aircraft Type | $L_o$ at $x=0$ (ft) | $L_o$ at $x=5\Delta x$<br>note 91 (ft) | $U_o$ at $x=5\Delta x$<br>note 89 (fps) | $R_\ell$ | $v_T$<br>(ft <sup>2</sup> /s) | $A$     |
|---------------|---------------------|--|---|----------|-------------------------------|---------|
| F-16          | 3.5818              | 8.0091                                 | 48.264                                  | 2.36 e 4 | 2.90                          | 139.921 |
| F-18          | 4.6212              | 10.3335                                | 62.271                                  | 3.92 e 4 | 4.83                          | 300.521 |
| F-15          | 3.9577              | 8.8497                                 | 53.329                                  | 2.88 e 4 | 3.54                          | 188.763 |
| B-52          | 7.7327              | 17.2908                                | 71.376                                  | 7.53 e 4 | 9.26                          | 660.671 |

**Table 7: Coefficients used for the Reynolds stress and self-propelled momentum defect models<sup>92</sup>**

The resulting values shown in Table 7 are then placed into Equation 52. The model of the Reynolds stress of the vertical and horizontal components of velocity as a function of the cross component of wake are graphed in Figure 29.

<sup>89</sup> Lecture notes from Dr. Mark Glauser during Fundamentals of Turbulence course, Syracuse University, Spring 2006.

<sup>90</sup> *Ibid.*

<sup>91</sup> The value of  $\Delta x$  is dependent on the aircraft category. F-16, F-15, and F-18 are in the fighter category while the B-52 is in the bomber category. Reference Table 2, Table 3, and Table 4 for the proper values.

<sup>92</sup> Example calculations of this table can be found in APPENDIX 9: CHAPTER 3 SAMPLE CALCULATIONS

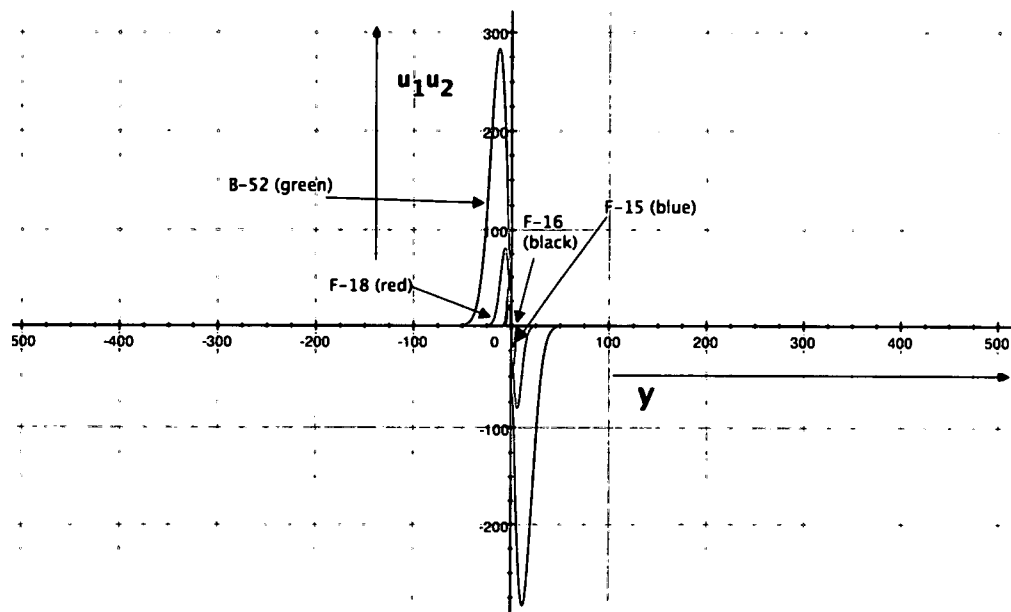


**Figure 29: Reynolds stress model of B-52, F-16, F-15, and F-18**

The area under each curve constitutes the total Reynolds stress exerted by each aircraft's turbulent wake. As expected, the B-52 has a much larger stress profile compared to the fighter aircraft. On today's mission, Viper 1 has only selected the fighter category to search. A close up of the Reynolds stress profiles for the fighter aircraft are shown in Figure 30.

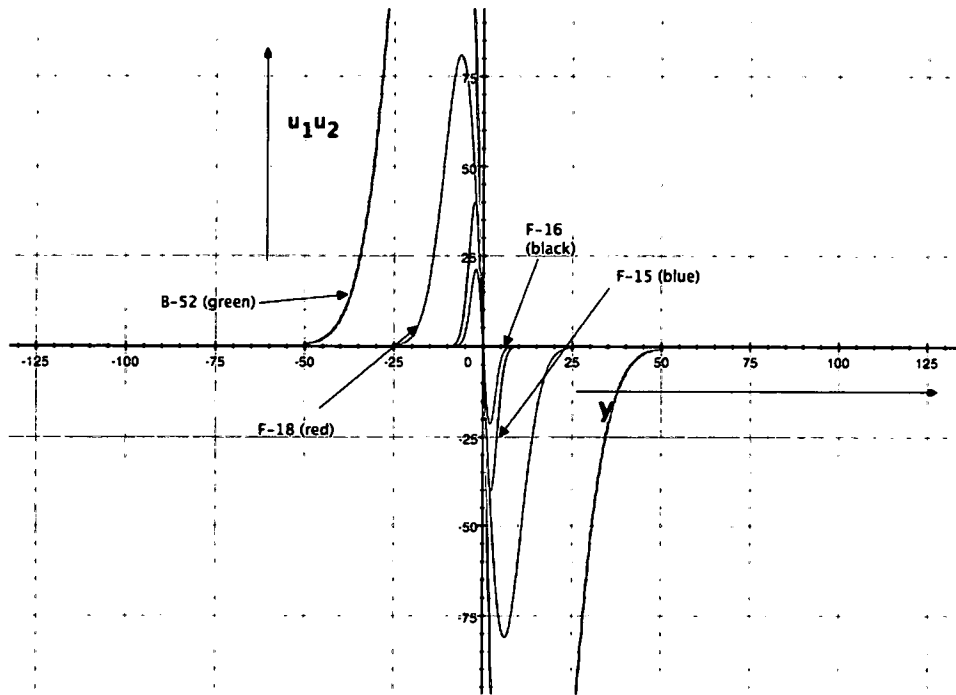


**Figure 30: Close up view of Reynolds stress profile for the F-18, F-16, and F-15.**

From inspection, it can be seen that turbulent self-preservation indeed holds true due to the fact that each aircraft has its own distinct turbulent signature. In addition, the shape of each curve closely resembles experimental results of Reynolds stress profiles measured with horizontal and vertical components of velocity shown in Figure 7.

The same coefficients in Table 7 are used to create the self-propelled momentum defect model (reference Equation 51). Figure 31 shows the graphs of their profiles and half-widths. The y-axis denotes the cross width of the wake profile in feet. The x-axis represents the mean velocity in feet per second. Note the Gaussian shape of the momentum defect signatures. The equation for each profile is also the probability density function used to correlate mean velocity measurements to the type of aircraft. In Figure 32, the standard deviations are displayed for each aircraft. The standard deviation,  $\sigma$ , is 54% of  $U_0$ . In this figure, the mean velocity is shown on the right side of the x-axis,

while the instantaneous velocity is shown on the y-axis. The left side of the x-axis is used for probability analysis based off of horizontal velocity fluctuations per time.

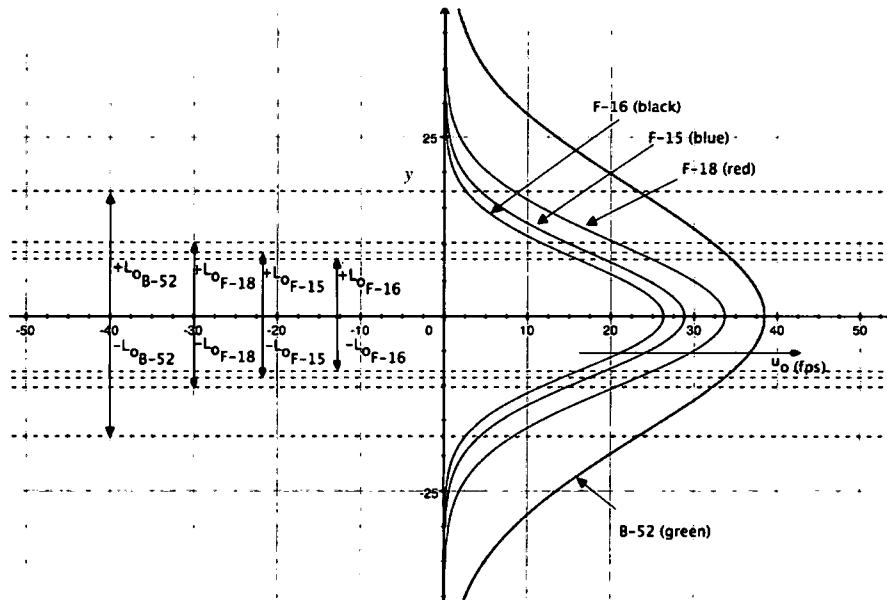


**Figure 31: Self-propelled momentum defect signatures and half-widths of F-16, F-18, F-15, and B-52**

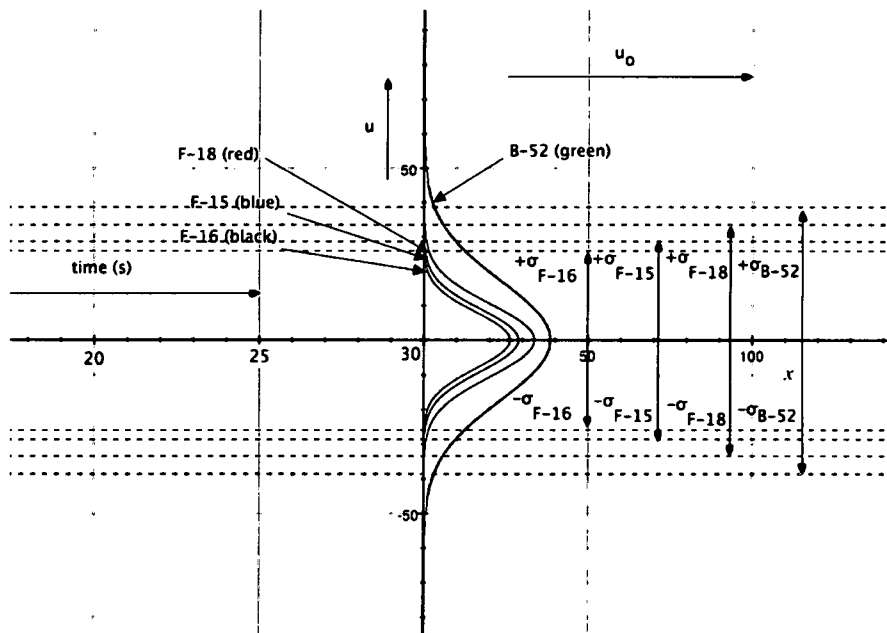


**Figure 32: Self-propelled momentum defect profiles for the B-52, F-16, F-18, and F-15 and their corresponding standard deviations.**

Armed with the information presented in this section, hostile aircraft is ready to be detected and identified.

### The Intercept

Air Force ground intelligence has received information that a hostile, low-observable F-18 has taken off from a combatant nation airfield and is heading south-west towards friendly airspace. The alert F-16 aircraft, Viper 1, has been scrambled and is flying north in an effort to intercept the aircraft. Viper 1 is carrying the new APG-68vX radar with the capability to target low-observable aircraft through the detection and identification of their turbulent wakes. GCI, callsign Darkstar, has a standard pulse-Doppler radar. Read the following radio conversation:

Viper 1: *"Darkstar, this is Viper 1, checking in as fragged. Picture north?"*

Darkstar: *"Viper 1, this is Darkstar, altimeter 29.92. Picture north clean."*

Viper 1 has reported "on-station" to Darkstar and is flying north. Currently, both GCI and the F-16 have a clean radarscope (*"picture clean"*). Viper 1's radar antenna is sweeping left and right transmitting and receiving microwave energy. The antenna is looking for changes in the reflective index of the atmosphere. The reflective index (described in detail on page 56) is a function of the refractive index,  $\Delta n^2$ . The refractive index, in turn, is a function of the turbulence parameter,  $C_n^2$ . Finally, the turbulence parameter is a function of turbulent dissipation,  $\epsilon$ . From the Chapter 1 discussion, turbulent production is equal to turbulent dissipation. By taking direct radar measurements of the atmosphere, the radar aboard the aircraft will be able to detect turbulent production within its field of view. Of course, turbulent production can come from natural or man-made objects. In order to determine the difference, a filtering

method will be applied. This is similar to the same filtering method used for pulse-Doppler radars to blank ground returns (discussed in Chapter 2). It will be assumed that the turbulent production generated by an aircraft is much greater than the turbulent production of CAT. Through further real-world experimentation, a value for maximum CAT production can be determined. Any value equal to or less than the CAT value will be filtered from the radar return. As an additional filtering method, turbulent radar returns from aircraft will move at a high velocity. This velocity will be much greater than the movement of CAT. Therefore, turbulent returns that are moving less than a pre-defined velocity threshold will also be filtered.

Viper 1: *"Darkstar, this is Viper 1. Picture, single group, bullseye 180, 45, 20 thousand. Declare?"*

Darkstar: *"Viper 1, Darkstar is clean."*

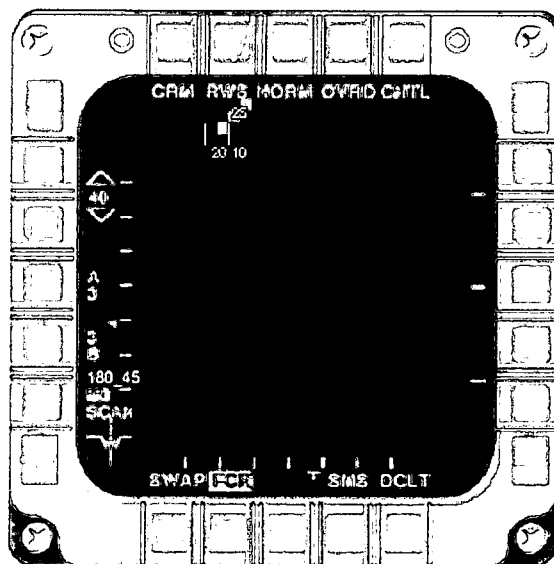


Figure 33: Viper 1 radar picture of initial contact with low-observable aircraft

Viper 1 now has radar contact with a single group at a range of approximately 35 nautical miles at a left azimuth of 30 degrees (see Figure 33). Viper 1 calls out his

picture to Darkstar and requests an IFF interrogation to determine whether the contact is friendly, hostile, or unknown (*Declare?*). Because the unknown aircraft is low-observable, Darkstar does not have a radar contact and transmits that he is “*clean*”.

Viper 1’s radar is now detecting turbulent production above the sensor’s filtering threshold. As the unknown aircraft proceeds through the fluid medium of the atmosphere, a turbulent wake is being generated behind it. As the radar sweeps left and right, it detects updates of radar refractivity. The refractivity being generated at the aircraft is much greater than that of the dissipating wake trailing it. Therefore, only the highest intensity of refractivity is being displayed (the actual location of the aircraft).

Viper 1: “*Darkstar, Viper 1 is targeted bullseye 181, 46, 20 thousand, bogey.*”

Darkstar: “*Darkstar copies.*”

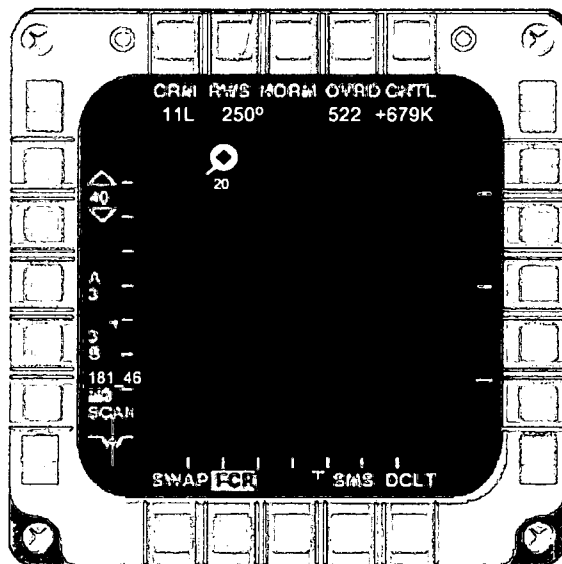


Figure 34: Viper 1 targets the low-observable aircraft (522 knots at 20,000’ (STD temp) =  $M=0.85$ )

With the absence of further information from Darkstar, Viper 1 moves his cursors over the radar contact, pushes forward on his TMS switch, and targets the contact (see Figure 34). Since it still an unknown contact, Viper 1 declares him as “*bogey*”. Darkstar

acknowledges Viper 1. The radar antenna is now “dwelling” on the radar bug and providing continuous updates on position, aspect angle, heading, airspeed, and closure rate. This is done through a processor using geometric parameters. Figure 35 shows how two dwell updates, spaced 4 seconds apart, produce the radar picture shown in Figure 34.

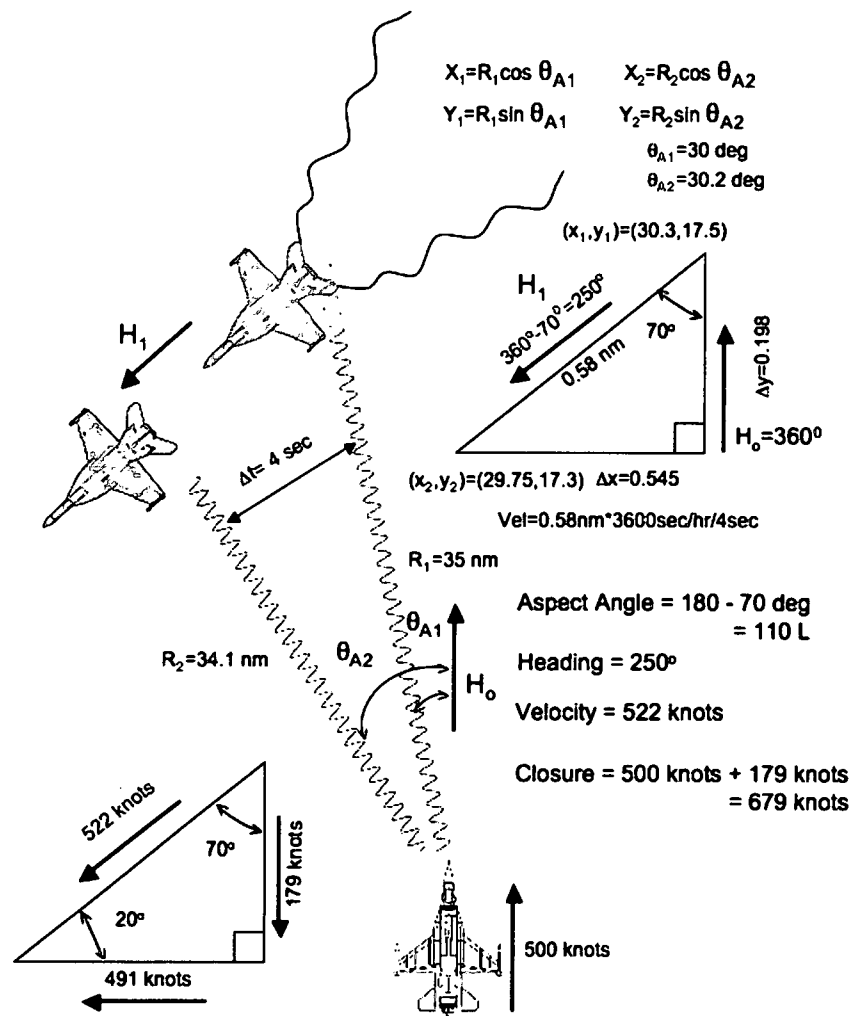


Figure 35: Geometric principles used to analyze radar contact parameters using two radar updates spaced 4 seconds apart.

### Target Identification Using a Radar Only Configuration

It has already been established that the radar sensor onboard Viper 1 can detect turbulent disturbances by means of the atmospheric radar reflectivity. Through multiple associations, the turbulent dissipation can be calculated as a function of the radar reflectivity (reference Equation 67 and associated discussion). Equation 29 also shows that turbulent production equals turbulent dissipation. Turbulent production is a function of Reynolds stress and the mean rate of strain (reference Equation 17 for the definition of the mean rate of strain). The mean rate of strain (units of  $s^{-1}$ ) can be estimated using the relation  $\frac{u}{\ell}$ , where  $u$  is the mean velocity at a defined point in the turbulent flow, and  $\ell$  is the integral scale. The assumption that the mean rate of strain equals  $\frac{u}{\ell}$  is the same assumption made to derive the Taylor microscale in Equation 35. This being said, the measured turbulent dissipation can be related to Reynolds stress using the relation:

$$u_1 u_2 = \frac{\varepsilon}{\bar{S}} \text{ where } \bar{S} \text{ is approximated using the relation } \frac{u}{\ell}$$

**Equation 70: Reynolds stress as a function of turbulent dissipation and mean rate of strain**

As noted on page 70, a radar range gate has been preset into the processor of the radar sensor to take radar samples at a point 5 body lengths behind the targeted aircraft. Since the “fighter” category has been selected today, the radar will take samples at a distance of  $5\Delta x_f$  (units of feet) behind the targeted aircraft. The definition of range gate is a discrete point in range along a single radial of radar data at which the received signal is sampled. The range gate sample in this case will be defined as a function of the

targeted aircraft's body length (selected category), range, and heading, as well as the ownship's heading and radar azimuth (see Figure 36).

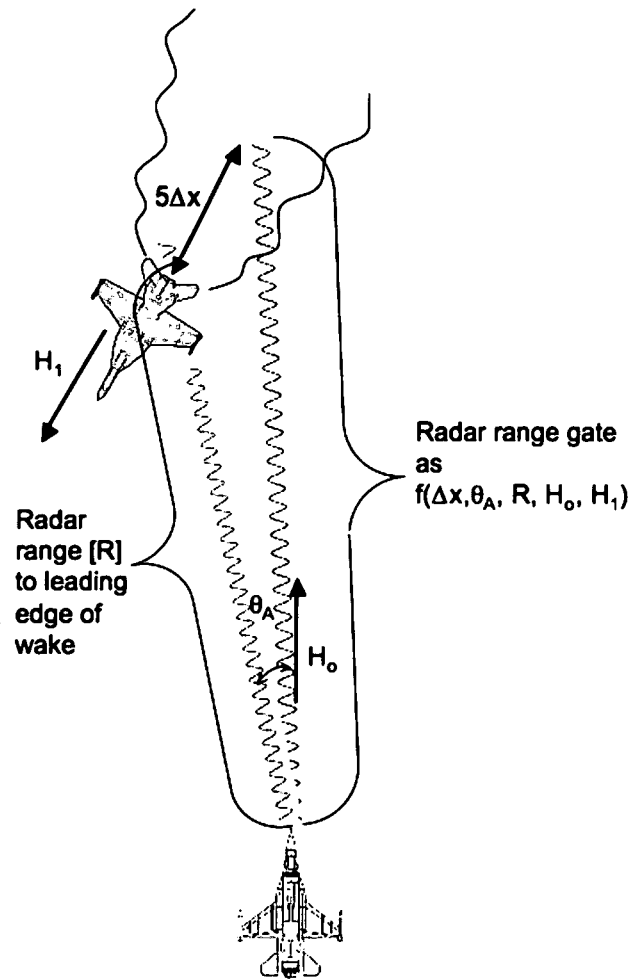


**Figure 36: Description of the radar range gate sampling of turbulent flow 5 body lengths behind the targeted aircraft**

Once the unknown aircraft is targeted, the radar sensor will automatically begin range gate sampling to identify the aircraft. The sensor measures turbulent reflectivity and measures the amount of turbulent energy dissipation at  $5\Delta x_f$ . From the aircraft database, information can be obtained that describes the integral scale and the mean rate of strain

calculated using the mean velocity at  $5\Delta x_f$  (see Table 7). The Reynolds stress is found by taking the surface integral of the modeled curves in Figure 30. The expected turbulent dissipation is calculated in the last column of the following table (Table 8).

| Aircraft Type | $\ell$ (ft) | $\bar{S}$ ( $s^{-1}$ ) | Reynolds stress ( $ft^2/s^2$ ) | $\epsilon$ ( $ft^2/s^3$ ) |
|---------------|-------------|------------------------|--------------------------------|---------------------------|
| F-16          | 2.00        | 24.10                  | $2.56 \times 10^{-1}$          | $6.16 \times 10^0$        |
| F-15          | 2.21        | 24.10                  | $3.38 \times 10^0$             | $8.15 \times 10^1$        |
| F-18          | 2.58        | 24.10                  | $1.37 \times 10^4$             | $3.31 \times 10^5$        |

**Table 8: Modeled values for integral scale, mean rate of strain, Reynolds stress, and turbulent dissipation for the F-16, F-15, and F-18 at  $M=0.85$ , 20,000' MSL, at a distance of  $5\Delta x_f$  behind the aircraft.<sup>93</sup>**

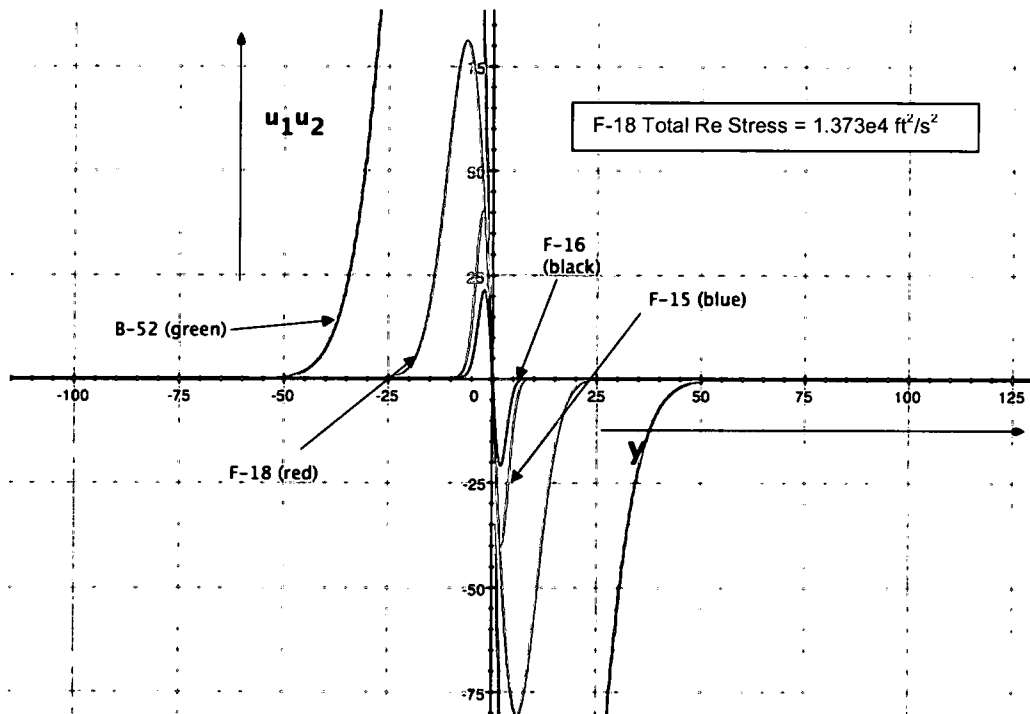


**Figure 37: The total Reynolds stress of the F-18 model shown as the shaded area under the curve.**

<sup>93</sup> Example calculations of this table can be found in APPENDIX 9: CHAPTER 3 SAMPLE CALCULATIONS

For example, if the atmospheric reflectivity at the range gate results in a measured value of turbulent dissipation of  $3.05 \times 10^5 \text{ ft}^2/\text{s}^3$ , then the resulting percent match to each aircraft's modeled  $\epsilon$  is shown in Table 9.

| Aircraft Type | Measured $\epsilon \text{ (ft}^2/\text{s}^3)$ | Modeled $\epsilon \text{ (ft}^2/\text{s}^3)$ | % match   |
|---------------|---|--|-----------|
| F-16          | $3.05 \times 10^5$                            | $6.16 \times 10^0$                           | 0.0020 %  |
| F-15          | $3.05 \times 10^5$                            | $8.15 \times 10^1$                           | 0.0267 %  |
| F-18          | $3.05 \times 10^5$                            | $3.31 \times 10^5$                           | 92.1579 % |

**Table 9: Correlation between measured and modeled values of  $\epsilon$  for the F-16, F-15, and F-18**

As seen in the table above, the measured value of turbulent dissipation most closely correlates to the F-18. If, for example, two aircraft were closely correlated to the measured turbulent dissipation, the radar scope would show a “mipple” or double correlation. The aircraft ID display would switch between both correlated aircraft. As long as both aircraft types were considered hostile, then the target could be declared hostile. If the correlation is between a friendly and hostile aircraft, then the pilot would hold his shot until a visual identification could be made.

#### Target Identification Using a Lidar Configuration

As discussed in Chapter 2, lidar can directly measure the radial component of velocity by directly measuring reflected IR energy off of naturally occurring aerosols in the atmosphere. By taking two lidar samples above and below the ownship's flight path, Equation 68 and Equation 69 can be used to determine the horizontal and vertical velocity of those aerosols.

In addition, the self-propelled momentum defect model can be used to correlate the measured momentum wake average velocity of the targeted aircraft. The measurement will be taken at the range gate defined in Figure 36. The total time of the

lidar sample in this case will be 30 seconds. During this time, the lidar will measure the instantaneous horizontal velocity and then average it over time to determine the average velocity. Table 10 shows the modeled average velocity for a self-propelled momentum defect wake.

| Aircraft Type | Self-propelled average velocity at $5\Delta x_f$ (ft/s) <sup>94</sup> |
|---------------|---|
| F-16          | 26.062  |
| F-15          | 28.798  |
| F-18          | 33.626  |

**Table 10: Average velocity model of self-propelled momentum wake for F-16, F-15, and F-18 at  $5\Delta x_f$**

As a reminder, the curve of the self-propelled momentum defect model shown in Figure 32 is also the PDF. As a result, an attempt can be made to correlate the targeted aircraft not only by the measured average velocity, but also by the ratio of the amount of time the measured average velocity is between the standard deviation of the PDF and the total time of the sample. In the following figures, the curve on the left side of the graph represents the fluctuating measurements of instantaneous horizontal velocity by the lidar. The blue shaded area below the curve represents the amount of time the instantaneous velocity falls within the standard deviation of each aircraft's PDF.

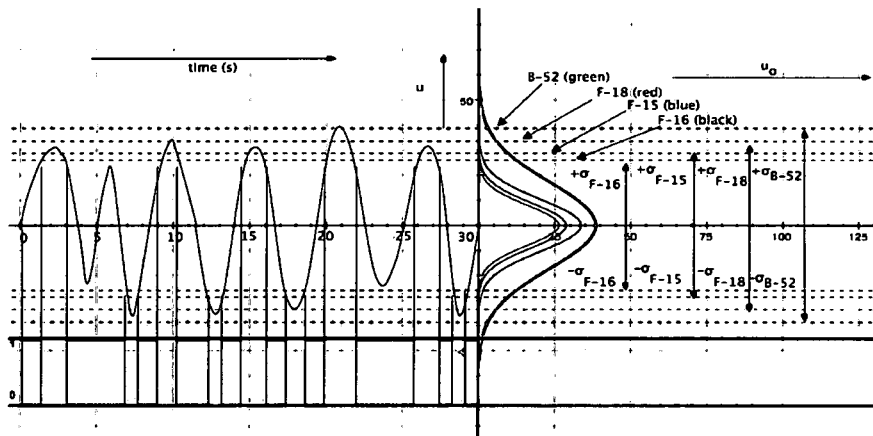


**Figure 38: Instantaneous velocity fluctuations and the correlation to the F-16 PDF**

<sup>94</sup> The self-propelled average velocity is 54% of the  $u_0$  at  $5\Delta x_f$  shown in Table 7.

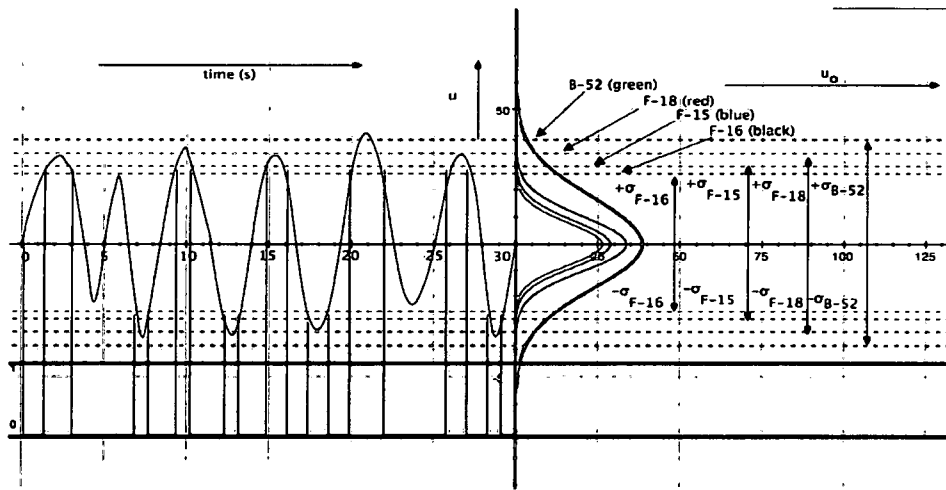


Figure 39: Instantaneous velocity fluctuations and the correlation to the F-15 PDF

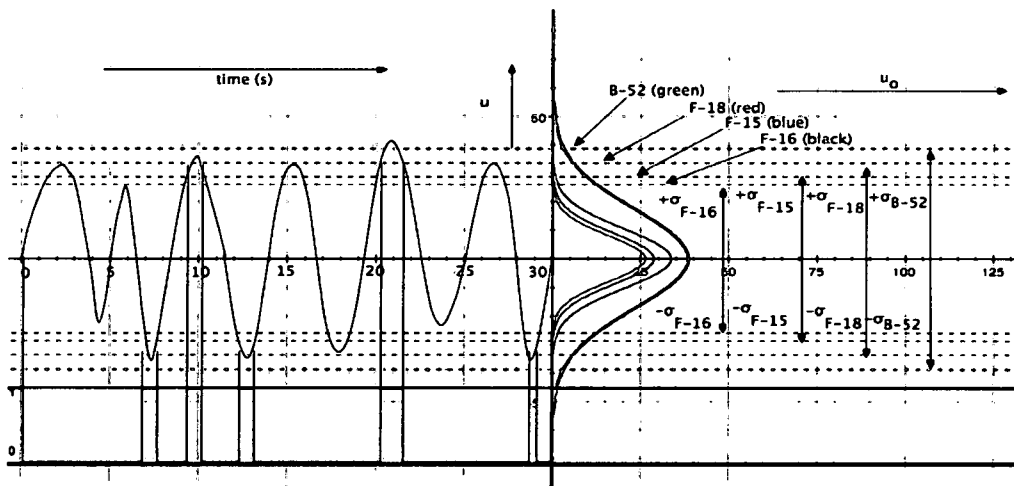


Figure 40: Instantaneous velocity fluctuations and the correlation to the F-18 PDF

For this example, the lidar's measured average velocity of the self-propelled momentum defect wake over a 30 second sample is 32.123 ft/s. Additionally, the probability of each aircraft's instantaneous velocity measurements can be evaluated by referencing Figure 38, Figure 39, and Figure 40. The results of this evaluation are shown in Table 11.

| Aircraft Type | Measured wake average velocity (fps) | Model wake average velocity (fps) | % match of model average velocity | Time (s) within $\sigma$ of aircraft PDF | Total sample time (s) | Probability of match |
|---------------|--------------------------------------|-----------------------------------|-----------------------------------|--|-----------------------|----------------------|
| F-16          | 32.123                               | 26.062                            | 81.132 %                          | 18.1                                     | 30                    | 60.3 %               |
| F-15          | 32.123                               | 28.798                            | 89.649 %                          | 18.7                                     | 30                    | 62.3 %               |
| F-18          | 32.123                               | 33.626                            | 95.530 %                          | 25.8                                     | 30                    | 86.0 %               |

**Table 11: Correlation of self-propelled momentum defect average velocity and PDF probability for F-16, F-15, and F-18**

Based on the measurements of the lidar, the targeted aircraft most closely correlates to a hostile F-18. Again, the mipping concept applies if two aircraft closely match correlation.

### The End Game

Once the radar/lidar sensor correlates the targeted aircraft's identification, the bugged target symbol will change from a circumscribed square to a red circumscribed triangle. The aircraft's ID will be shown next to the radar bug.

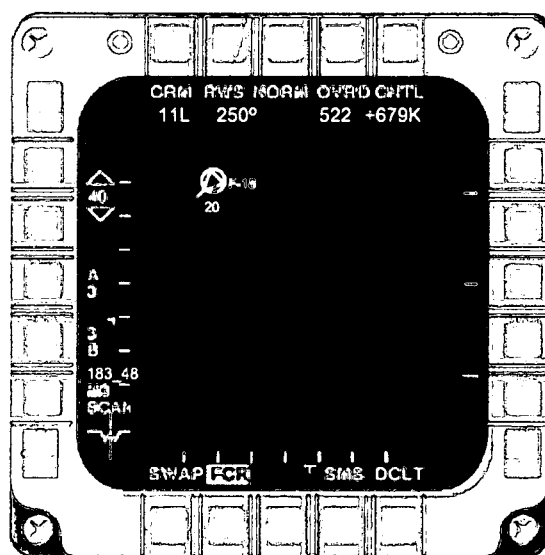
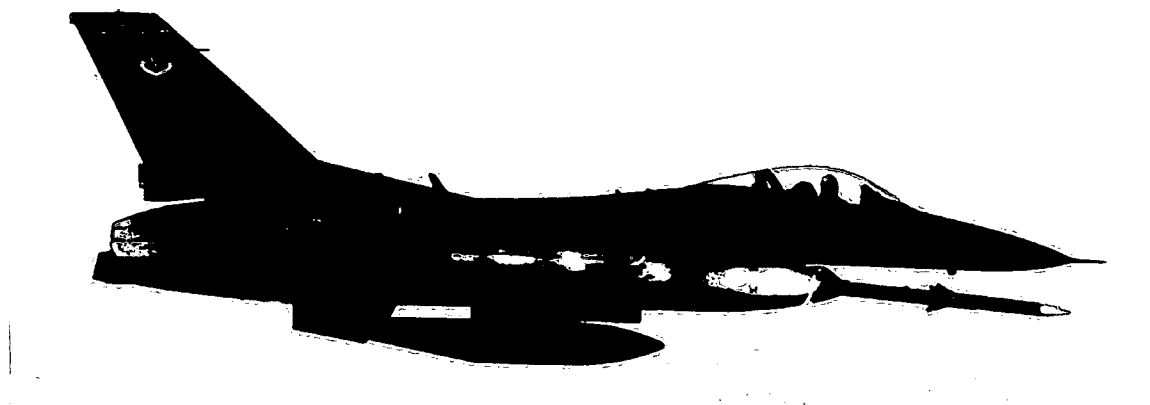


**Figure 41: Radar display of identified hostile F-18**

Viper 1: *"Darkstar, Viper 1 declare bullseye 183, 48, 20 thousand, hostile F-18.*

*Fox 3!!!"*<sup>95</sup>



*"Viper 1, Fox 3!!!"*

### Conclusion and Recommendations

It is important to note that the information described in Chapter 3 is a notional example of a radar with such capabilities. Chapter 3 textually identifies the requirements for such a radar and the possible operating principles based on the information presented in Chapter 1 and 2. Additional requirements for this radar would be that radar targets should be detected no later than 40 nautical miles, and should be identified no later than 30 nautical miles.

The obvious advantage of this radar sensor is that it can detect low observable targets. However, it can also be used to counter high observable aircraft radar defense maneuvers such as the Doppler notch (see Figure 12 and surrounding discussion). Because turbulent wakes have 3 dimensional characteristics, the radar sensor would be

---

<sup>95</sup> "Fox 3" is the radio brevity term for a radar guided air-to-air missile launch.

less affected by Doppler filtering used on traditional pulse Doppler radars. Aircraft also have sensors on the airframe that detect radar energy. This sensor is called the Radar Warning Receiver (RWR). It allows a pilot to know when an aircraft is targeting his ownship with a fire control radar. Since the turbulent radar sensor is illuminating the wake of the targeted aircraft and not the airframe itself, it is more likely that the enemy aircraft's RWR sensors will not detect the radar energy. Therefore, the turbulent radar could also be considered a "semi" passive radar system. This will allow an aircraft equipped with the turbulent radar sensor to detect, identify, and shoot an aircraft without the enemy being aware that the intercept is occurring.

The real world disadvantage of this system is that turbulent detection technology is still in its infancy. Even the most powerful radars can only detect large aircraft at 8.1 nautical miles, while lidars are affected by weather and can only detect aerosols at about 5.4 nautical miles. As technology progresses, and radar sensors become more powerful and sensitive, the requirements for a fighter aircraft radar will be met.

While the turbulent fundamentals outlined in Chapter 1 are well documented, the Reynolds stress model and self-propelled momentum defect model for the F-16, F-15, F-18, and B-52 have not been verified experimentally. This thesis provides a framework for future laboratory research that will eventually turn the detection and identification of aircraft turbulent wakes into a reality.

## VITA

|                  |   |
|------------------|---|
| January 13, 1974 | Born-Warren, Ohio   |
| 1996             | B.S., Aeronautical Engineering, USAF Academy, CO  |
| 1998             | Graduate, Euro-NATO Joint Jet Pilot Training<br>Sheppard AFB, Wichita Falls, Texas                              |
| 1999-2002        | F-16 Pilot, USAF, 13 <sup>th</sup> Fighter Squadron<br>Misawa AB, Misawa, Japan                                 |
| 2002-2005        | Air Liaison Officer, USAF, 1 <sup>st</sup> BDE, 10 <sup>th</sup> MTN Division<br>Fort Drum, Watertown, New York |
| 2004             | Fighter Duty Officer, USAF, Detachment Commander<br>Bagram AB, Afghanistan<br>Kandahar AB, Afghanistan          |
| 2005-2006        | Aeronautical Engineer, Syracuse Research Corporation<br>Dayton, Ohio  |
| 2006-2007        | F-16 Simulator Instructor Pilot, L-3 Communications<br>Thumrait Air Base, Sultanate of Oman                     |

## AWARDS AND DECORATIONS

Bronze Star, Air Force Commendation Medal, Air Force Achievement Medal, Army Commendation Medal, Air Medal, Aerial Achievement Medal

## FIELDS OF STUDY

Major field; Fluid Dynamics

Studies of Turbulence, Professor Mark Glauser, Syracuse University

Studies of Fluid Dynamics, Professor Jacques Lewalle, Syracuse University

## BIBLIOGRAPHY

- Antonia, R.A., Mi, J. 1998. Approach towards self-preservation of turbulent cylinder and screen wakes. *Experimental Thermal and Fluid Science*. 17. pp. 277-284.
- Bean, B.R. and Dutton, E.J. 1966 *Radio Meteorology* NBS Monograph 92, US Government Printing Office, Washington, D.C.
- Bernard-Trottole, S., Campistron, B., Druilhet, A., Lohou, F., Said, F. 2004. Trac98: Detection of coherent structures in a convective boundary layer using airborne measurements. *Boundary-Layer Meteorology*. 111. pp. 181-224.
- Brouwers, J.J.H. 2002. On diffusion theory in turbulence. *Journal of Engineering Mathematics*. 44. pp. 277-295.
- Carlson, J.R., Duquesne, N., Rumsey, C.L., Gatski, T.B. 2001. Computation of turbulent wake flows in a variable pressure gradient. *Computers and Fluids*. 30. pp. 161-187.
- Chadwick, R. B., Jordan, J. and Detman, T. 1984 Radar cross section measurements of wingtip vortices. *Proc. ESA IGARSS 1984*, vol. 1, pp. 479-483.
- Dole, J., Wilson, R. 2001. Turbulence Dissipation Rates and Vertical Diffusivity in the Stratosphere from Radar Observations. *Phys. Chem. Earth*. Vol. 26, No. 3. pp. 225-229.
- Elsner, J.W., Elsner, W. 1996. On the measurement of turbulence energy dissipation. *Meas. Sci. Technol*. 7. pp. 1334-1348.
- Gaifullin, A.M. 2001. Equations of Perturbation Growth in Aircraft Wakes. *Fluid Dynamics*. Vol. 36, No. 3. pp. 448-457.
- George, W.K. and Gibson, M.M. 1992: The self-preservation of homogeneous shear flow turbulence. *Experiments in Fluids*. 13. pp. 229-238.
- George, William K. 1989: The self-preservation of turbulent flows and its relation to initial conditions and coherent structures. *Advances in Turbulence*. p. 39-73.
- George, William K., 1974. The measurement of turbulence intensities using real-time laser-Doppler velocimetry. *J. Fluid Mech*. Vol. 66, Part 1. pp. 11-16.

- Gilson, W.H. 1994 Aircraft wake RCS measurement. *NASA Contractor Rep.* 10139, Part 2, pp. 603-623.
- Grant, Rebecca. *The RADAR game. Understanding Stealth and Aircraft Survivability.* IRIS Independent Research, Arlington, Virginia, 1998.
- Hannon, S.M. 2000: Autonomous Infrared Doppler Radar: Airport Surveillance Applications. *Phys. Chem. Earth.* Vol. 25, No. 10-12. pp. 1005-1011.
- Harris, M., Vaughan, M.J., Huenecke, K., Huenecke, C. 2000: Aircraft wake vortices: a comparison of wind-tunnel data with field trail measurements by laser radar. *Aerosp. Sci. Technolo.* 4. pp. 363-370.
- Hinze, J.O., *Turbulence.* McGraw-Hill, New York, 1959.
- Hovanessian, S.A. *Introduction to Sensor Systems.* Artech House, Norwood, MA, 1988.
- Hunt, J.C.R., Eames, I. 2002. The disappearance of laminar and turbulent wakes in complex flows. *J. Fluid Mech.* 457. pp. 111-132.
- Latteck, R., Singer, W., Hocking, W.K. 2005. Measurement of turbulent kinetic energy dissipation rates in the mesosphere by a 3 MHz Doppler radar. *Advances in Space Research.* 35. pp. 1905-1910.
- Megaw, E.C.S. 1957. *Proc. Inst. Elec. Eng.* 104C. p.441.
- Meunier, Patrice, Spedding, Geoffrey. 2006: Stratified propelled wakes. *Journal of Fluid Mechanics.* 552. pp. 229-256.
- Michelet, S., Antoine, Y., Lemoine, F., Mahouast, M. 1998. Mesure directe du taux de dissipation de l'énergie cinétique de turbulence par velocimétrie laser bi-composante: validation dans une turbulence de grille. *Mécanique des fluides.* 326, Series II b. pp. 621-626.
- Nespor, J., Hudson, E., Stegall, R., and Freedman, J. 1994 Doppler radar detection of vortex hazard indicators. *NASA Conf. Proc.* CP-10139, Part 2, pp. 651-688.
- Noonkester, V.R. and Richter, J.H. 198. FM-CW radar sensing of the lower atmosphere. *Radio Sci.* 15, 337-353.
- Novikov, B.G. 2001. Interference Model of the Wake Development Downstream of a Self-Propelled Body. *Fluid Dynamics.* Vol. 36, No. 4. pp. 581-588.
- Putkaradze, V., Weidman, P. 2003. Turbulent wake solutions of the Prandtl  $\alpha$  equations. *Physical Review.* 67, 306304. pp. 1-7.

- Rogers, Michael M. 2002. The evolution of strained turbulent plane wakes. *J. Fluid Mech.* 463. pp. 53-120.
- Saarenrinne, P., Piirto, M. 2000. Turbulent kinetic energy dissipation rate estimation from PIV velocity vector fields. *Experiments in Fluids. Suppl.* pp. S300-S307.
- Shariff, Karim and Wray, Alan. 2002: Analysis of the radar reflectivity of aircraft vortex wakes. *Journal of Fluid Mechanics.* 463. pp. 121-161.
- Silvestre, Ana Leonor. 2002. On the slow motion of a self-propelled rigid body in a viscous incompressible fluid. *J. Math. Anal. Appl.* 274. pp. 203-227.
- Smith, P.L. and Rogers R.R. 1963: *Proc. Tenth Weather Radar Conference, Am. Metero. Soc.*, Boston, p. 316.
- Soreide, D., Bouge, R., Ehernberger, L.J., Bagley, H. 1996. Coherent Lidar Turbulent Measurement for Gust Load Alleviation. *NASA Technical Memo. 104318.*
- Tennekes, H. and Lumley, J.L. *A First Course In Turbulence.* The MIT Press, Cambridge, Massachusetts, 1972.
- Vasil'ev, O.F., Demenkov, A.G., Kostomakha, V.A., Chernykh, G.G. 2001. Numerical Simulation of a Twisted Turbulent Wake beyond a Self-Propelled Body. *Doklady Physics.* Vol. 46, No. 1. pp. 52-55.
- Watkins, C.D. and Browning, K.A. 1973: The detection of clear air turbulence by radar. *Physics in Technology.* 4. pp. 28-61.
- Wynnanski, F.; Champagne; Marasli, B. 1986: On the large-scale structures in two-dimensional, small-deficit, turbulent wakes. *Journal of Fluid Mechanics.* 168. pp. 31-71.
- Xiaofeng, Liu, Thomas, Flint. 2004: Measurement of the turbulent kinetic energy budget of a planar wake flow in pressure gradients. *Experiments in Fluids.* 37. pp. 469-482.
- Younghase, John M. *Electronic Warfare Fundamentals.* SWL Inc., Vienna, VA, 1 August 1994, pp. 4-21.

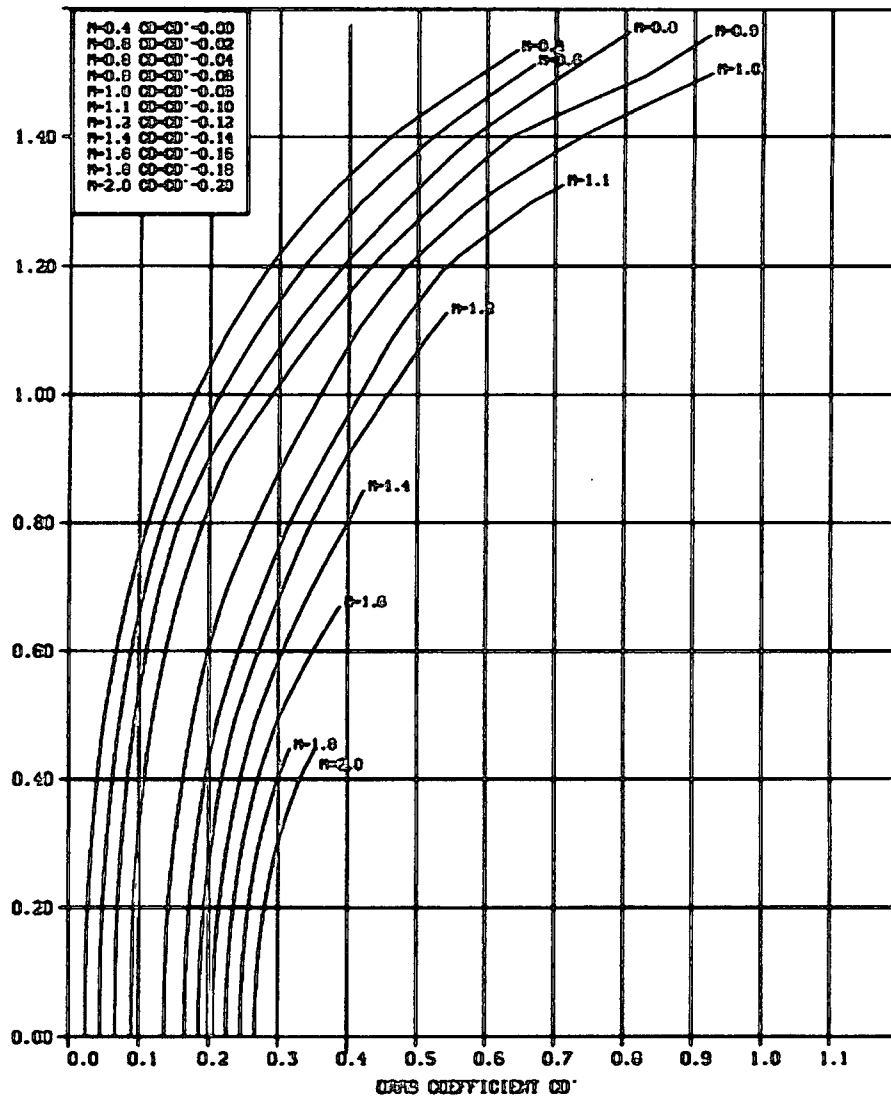
## APPENDIX 1: F-16C DRAG DATA

[illegible]

## APPENDIX 2: F-16C DRAG POLAR

F-16C Block 50 2-ARM9L  
 $S_{REF} = 27.9 \text{ m}^2$

LIFT COEFFICIENT  $C_L$



A- 669  
 07/29/84

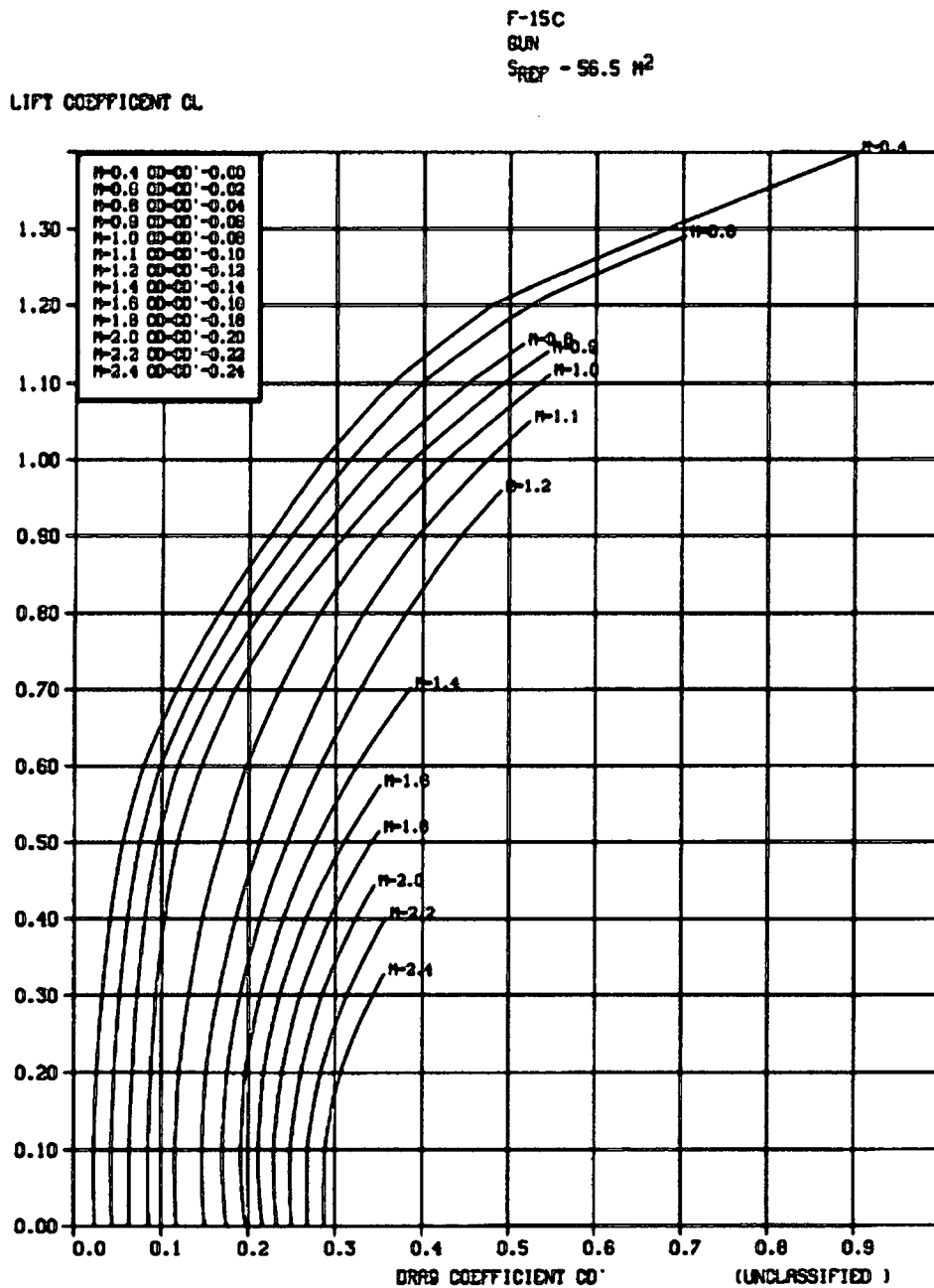
FIG. 11 (U) DRAG POLAR

## APPENDIX 3: F-15C DRAG DATA

**P-15 C (CLEAN)**

[illegible]

# APPENDIX 4: F-15C DRAG POLAR



A- 640  
08/17/93

FIG. 8 (U) DRAG POLAR

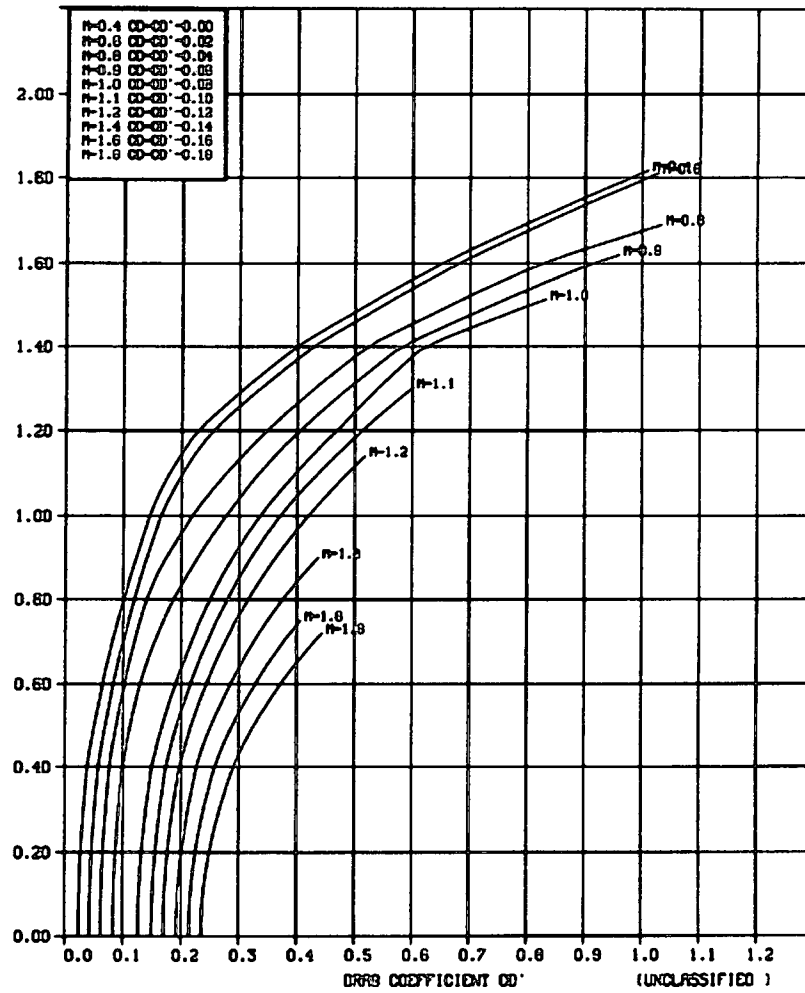
# APPENDIX 5: F-18C DRAG DATA

| A653.     |  | F-18C GUN   |   |
|-----------|--|---|---|
| 1922      | 0.0000   | 4000.4500.5000.5500.6000.6500.7000.7500.8000.8500.9000.9501.0001.0501 |   |
| 1.1001    | 1501.2001  | 4001.4001.8001.8500.0000.0000.0000                                    |   |
| 0.200     | 0255.0401.0458.0520.0590.0659.0736.0829.0921.1035.1131.1242.1357.1482.1609 |   |   |
| 1.1799    | 2024.2279.3999.6509.98121.071.0000.0000.0000                               |   |   |
| 0.500     | 0230.0376.0433.0495.0565.0634.0711.0804.0895.0997.1100.1208.1329.1429.1594 |   |   |
| 1.1784    | 2009.2264.3984.6504.97971.069.0000.0000.0000                               |   |   |
| 0.600     | 0225.0371.0428.0490.0560.0629.0706.0799.0891.0986.1091.1203.1325.1438.1618 |   |   |
| 1.1813    | 2053.2338.4078.6598.98911.079.0000.0000.0000                               |   |   |
| 0.700     | 0221.0367.0424.0486.0556.0625.0702.0795.0881.0982.1087.1213.1366.1536.1766 |   |   |
| 2.036     | 2346.2696.4441.71861.1231.233.0000.0000.0000                               |   |   |
| 0.800     | 0217.0363.0420.0482.0552.0621.0698.0791.0885.1002.1147.1335.1558.1784.2064 |   |   |
| 2.374     | 2719.3074.4809.78241.2671.402.0000.0000.0000                               |   |   |
| 0.850     | 0215.0361.0418.0480.0550.0619.0696.0789.0907.1052.1231.1446.1701.1971.2272 |   |   |
| 2.557     | 2892.3252.4992.81621.3291.473.0000.0000.0000                               |   |   |
| 0.900     | 0235.0391.0454.0521.0599.0691.0806.0937.1091.1361.1466.1681.1916.2171.2446 |   |   |
| 2.741     | 3076.3441.5201.84961.3751.519.0000.0000.0000                               |   |   |
| 0.950     | 0334.0513.0590.0679.0779.0887.1008.1137.1298.1481.1689.1913.2143.2388.2673 |   |   |
| 2.978     | 3313.3678.5453.88781.3951.504.0000.0000.0000                               |   |   |
| 1.000     | 0464.0696.0781.0876.0981.1101.1236.1376.1526.1696.1881.2086.2311.2556.2856 |   |   |
| 3.176     | 3516.3886.5384.92651.4181.550.0000.0000.0000                               |   |   |
| 1.050     | 0493.0713.0803.0903.1013.1133.1268.1413.1568.1733.1923.2128.2363.2608.2913 |   |   |
| 3.253     | 3613.3983.5803.89881.2411.326.0000.0000.0000                               |   |   |
| 1.100     | 0496.0739.0824.0924.1034.1159.1294.1449.1614.1799.1989.2207.2444.2704.3024 |   |   |
| 3.364     | 3739.4119.5954.80721.0391.119.0000.0000.0000                               |   |   |
| 1.150     | 0497.0754.0849.0949.1069.1199.1344.1504.1684.1869.2084.2309.2569.2844.3164 |   |   |
| 3.509     | 3884.4274.6154.80291.0201.092.0000.0000.0000                               |   |   |
| 1.200     | 0501.0774.0869.0974.1099.1239.1389.1564.1744.1954.2184.2429.2704.2994.3324 |   |   |
| 3.659     | 4059.4459.6229.7989.97491.019.0000.0000.0000                               |   |   |
| 1.300     | 0516.0824.0929.1049.1189.1344.1519.1709.1924.2149.2409.2694.3004.3344.3709 |   |   |
| 4.079     | 4449.4819.6299.7779.9259.9629.0000.0000.0000                               |   |   |
| 1.400     | 0524.0869.0984.1119.1279.1454.1644.1854.2086.2354.2644.2969.3344.3724.4104 |   |   |
| 4.484     | 4864.5284.6784.8284.98041.018.0000.0000.0000                               |   |   |
| 1.500     | 0531.0926.1046.1206.1371.1566.1771.2006.2271.2566.2886.3266.3646.4026.4406 |   |   |
| 4.786     | 5166.5546.7086.85861.0101.048.0000.0000.0000                               |   |   |
| 1.600     | 0540.0985.1125.1290.1475.1685.1915.2170.2460.2770.3080.3390.3700.4010.4320 |   |   |
| 4.630     | 4940.5250.6490.7730.8970.9280.0000.0000.0000                               |   |   |
| 1.700     | 0547.1042.1202.1377.1577.1802.2057.2337.2657.2987.3317.3647.3977.4307.4637 |   |   |
| 4.967     | 5297.5627.6947.8267.9587.9917.0000.0000.0000                               |   |   |
| 1.800     | 0554.1110.1270.1460.1680.1920.2200.2500.2845.3210.3575.3940.4305.4670.5035 |   |   |
| 5.400     | 5765.6130.7590.90501.0511.088.0000.0000.0000                               |   |   |
| 728.00000 | 1.80000  | 7.50000   | 0.00000 0.00000 0.00000 0.00000 0.00000 |

# APPENDIX 6: F-18C DRAG POLAR

F-18C  
EUN  
SREF = 37.2 m<sup>2</sup>

LIFT COEFFICIENT  $C_L$



R 653  
01/03/95

# APPENDIX 7: B-52H DRAG DATA

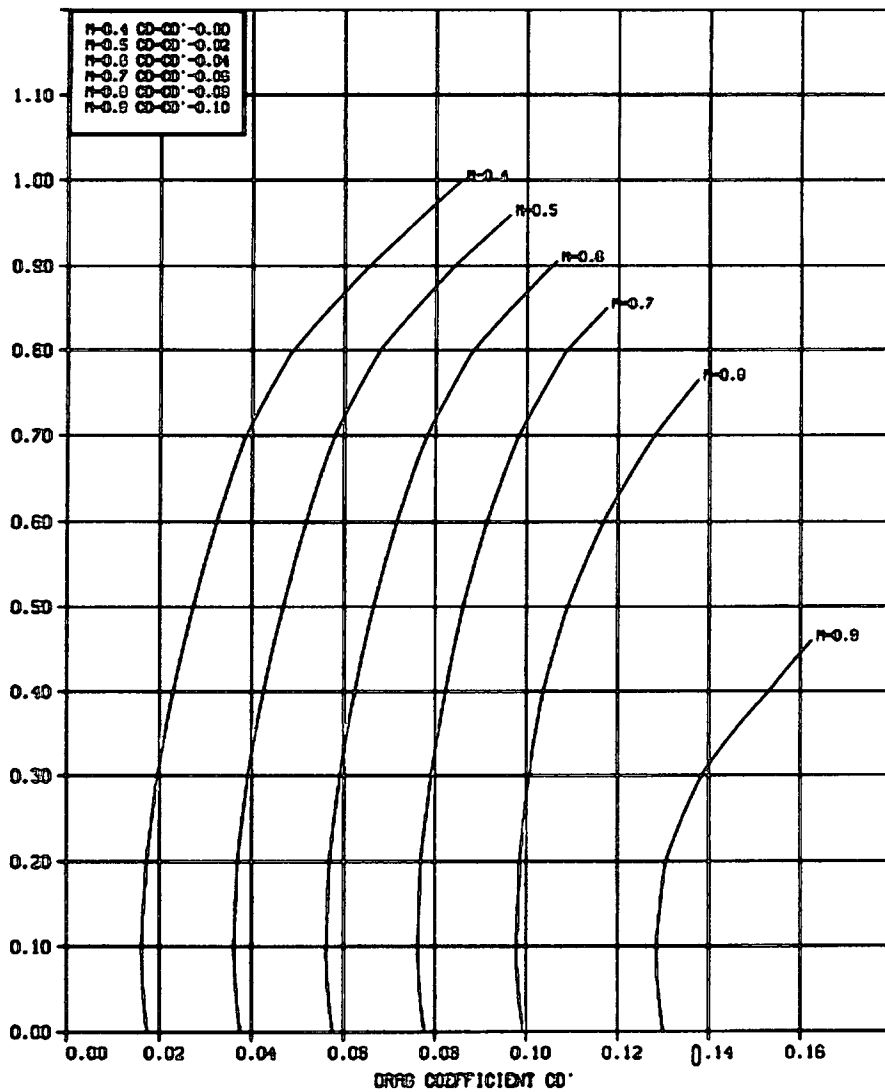
B-52M STRATOFORTRESS (FLIR, ECP, DATA CORRECTED AT CL = 0.8 AND 0.9)

|           |           |           |           |           |           |           |           |           |           |
|-----------|-----------|-----------|-----------|-----------|-----------|-----------|-----------|-----------|-----------|
| 1211      | 0.0000    | 1000.2000 | 3000.4000 | 5000.6000 | 7000.8000 | 9001.0000 | 0000.0000 | 0000.0000 | 0000.0000 |
|           | 0.0000    | 0000.0000 | 0000.0000 | 0000.0000 | 0000.0000 | 0000.0000 | 0000.0000 | 0000.0000 | 0000.0000 |
| 0.000     | 0.171     | 0.161     | 0.175     | 0.199     | 0.233     | 0.276     | 0.329     | 0.393     | 0.497     |
|           | 0000.0000 | 0000.0000 | 0000.0000 | 0000.0000 | 0000.0000 | 0000.0000 | 0000.0000 | 0000.0000 | 0000.0000 |
| 0.300     | 0.171     | 0.161     | 0.175     | 0.199     | 0.233     | 0.276     | 0.329     | 0.393     | 0.497     |
|           | 0000.0000 | 0000.0000 | 0000.0000 | 0000.0000 | 0000.0000 | 0000.0000 | 0000.0000 | 0000.0000 | 0000.0000 |
| 0.500     | 0.175     | 0.162     | 0.169     | 0.192     | 0.225     | 0.268     | 0.317     | 0.379     | 0.477     |
|           | 0000.0000 | 0000.0000 | 0000.0000 | 0000.0000 | 0000.0000 | 0000.0000 | 0000.0000 | 0000.0000 | 0000.0000 |
| 0.700     | 0.177     | 0.163     | 0.169     | 0.192     | 0.223     | 0.261     | 0.313     | 0.383     | 0.487     |
|           | 0000.0000 | 0000.0000 | 0000.0000 | 0000.0000 | 0000.0000 | 0000.0000 | 0000.0000 | 0000.0000 | 0000.0000 |
| 0.750     | 0.183     | 0.170     | 0.174     | 0.194     | 0.224     | 0.266     | 0.320     | 0.397     | 0.513     |
|           | 0000.0000 | 0000.0000 | 0000.0000 | 0000.0000 | 0000.0000 | 0000.0000 | 0000.0000 | 0000.0000 | 0000.0000 |
| 0.790     | 0.190     | 0.176     | 0.183     | 0.203     | 0.233     | 0.280     | 0.350     | 0.448     | 0.581     |
|           | 0000.0000 | 0000.0000 | 0000.0000 | 0000.0000 | 0000.0000 | 0000.0000 | 0000.0000 | 0000.0000 | 0000.0000 |
| 0.810     | 0.199     | 0.183     | 0.190     | 0.209     | 0.241     | 0.299     | 0.386     | 0.511     | 0.679     |
|           | 0000.0000 | 0000.0000 | 0000.0000 | 0000.0000 | 0000.0000 | 0000.0000 | 0000.0000 | 0000.0000 | 0000.0000 |
| 0.830     | 0.209     | 0.193     | 0.200     | 0.221     | 0.258     | 0.333     | 0.448     | 0.607     | 0.793     |
|           | 0000.0000 | 0000.0000 | 0000.0000 | 0000.0000 | 0000.0000 | 0000.0000 | 0000.0000 | 0000.0000 | 0000.0000 |
| 0.850     | 0.223     | 0.208     | 0.215     | 0.239     | 0.290     | 0.393     | 0.545     | 0.723     | 0.913     |
|           | 0000.0000 | 0000.0000 | 0000.0000 | 0000.0000 | 0000.0000 | 0000.0000 | 0000.0000 | 0000.0000 | 0000.0000 |
| 0.870     | 0.245     | 0.229     | 0.239     | 0.269     | 0.349     | 0.493     | 0.663     | 0.847     | 1.047     |
|           | 0000.0000 | 0000.0000 | 0000.0000 | 0000.0000 | 0000.0000 | 0000.0000 | 0000.0000 | 0000.0000 | 0000.0000 |
| 0.890     | 0.277     | 0.263     | 0.276     | 0.323     | 0.463     | 0.620     | 0.797     | 0.982     | 1.157     |
|           | 0000.0000 | 0000.0000 | 0000.0000 | 0000.0000 | 0000.0000 | 0000.0000 | 0000.0000 | 0000.0000 | 0000.0000 |
| 0.910     | 0.323     | 0.307     | 0.334     | 0.445     | 0.599     | 0.767     | 0.947     | 1.107     | 1.273     |
|           | 0000.0000 | 0000.0000 | 0000.0000 | 0000.0000 | 0000.0000 | 0000.0000 | 0000.0000 | 0000.0000 | 0000.0000 |
| 400.00000 | 0.90000   | 0.90000   | 1.80000   | 0.00000   | 0.00000   | 0.00000   | 0.00000   | 0.00000   | 0.00000   |

# APPENDIX 8: B-52H DRAG POLAR

B-52H  
CLEARW  
S<sub>REF</sub> = 372 M<sup>2</sup>

LIFT COEFFICIENT C<sub>L</sub>



A-710  
01/22/97

## APPENDIX 9: CHAPTER 3 SAMPLE CALCULATIONS

Explanation of calculations shown in Chapter 3:

1. Given:

| Atmospheric Conditions at 20,000 ' MSL (Standard Temperature and Pressure) |                                |
|--|--------------------------------|
| Density ( $\rho$ )   | 0.001226 slugs/ft <sup>3</sup> |
| Temperature (degrees F)  | -12.3232 degrees F             |
| Kinematic viscosity ( $\nu$ ) at temp. shown                               | 1.24 e -4 ft <sup>2</sup> /s   |
| M = 1  | 1036.845 fps                   |
| M = 1  | 614.314 nm/hr                  |

2. Aircraft specific variables:

| Type A/C | T/O Weight (lbs) | Cruise Weight (lbs) | S (ft <sup>2</sup> ) | Wingspan (ft) | Mach | Airspeed (fps) | C <sub>L</sub> | C <sub>D</sub> | $\theta$ (ft) |
|----------|------------------|---------------------|----------------------|---------------|------|----------------|----------------|----------------|---------------|
| F-16     | 37,500           | 31,875              | 303.83               | 34            | 0.85 | 881.318        | 0.220          | 0.026          | 0.439         |
| F-18     | 65,800           | 55,930              | 405.11               | 45            | 0.85 | 881.318        | 0.290          | 0.032          | 0.730         |
| F-15     | 68,000           | 57,800              | 615.29               | 42            | 0.85 | 881.318        | 0.197          | 0.026          | 0.536         |
| B-52     | 488,000          | 414,800             | 4051.08              | 185           | 0.85 | 881.318        | 0.215          | 0.022          | 2.044         |

2.1. Cruise weight is assumed to be 85% of T/O weight

2.2. T/O weight, wing surface area, and wingspan given by online source.<sup>96</sup>

2.3. Mach number assumed to be 0.85. Airspeed given by multiplying Mach at 20,000' MSL by 0.85.

2.4. C<sub>L</sub> is determined using equation  $C_L = L/qS$ . L = cruise weight during level flight.

2.5. C<sub>D</sub> is given by tables in the appendix. For example: C<sub>D</sub> for the F-18 is found in APPENDIX 5: F-18C DRAG DATA. The top row of the table shows the coefficient of lift. The left column of the table shows the corresponding Mach number. In our case, a F-18 with a C<sub>L</sub> of 0.290 has a corresponding

<sup>96</sup> <http://www.fas.org/man/dod-101/sys/ac/>

$C_D$  between 0.0215 and 0.0361. Using interpolation, the corresponding  $C_D$  for a  $C_L$  of 0.290 equals 0.03245 (rounded to 0.032).

2.6. Momentum thickness is found using the equation  $C_D d = 2\theta$ . In this case,  $d$ , equals the wingspan of the aircraft. For the F-18,  $\theta = (0.03245 * 45) / 2 = 0.73$ .

3. Calculations for coefficients used for the Reynolds stress and self-propelled momentum defect models.

| Aircraft Type | $L_o$ at $x=0$ (ft) | $L_o$ at $x=5\Delta x$<br>note 89 (ft) | $U_o$ at $x=5\Delta x$<br>note 89 (fps) | $R_\ell$ | $v_T$ (ft <sup>2</sup> /s) | $A$     |
|---------------|---------------------|--|---|----------|----------------------------|---------|
| F-16          | 3.5818              | 8.0091                                 | 48.264                                  | 2.36 e 4 | 2.90                       | 139.921 |
| F-18          | 4.6212              | 10.3335                                | 62.271                                  | 3.92 e 4 | 4.83                       | 300.521 |
| F-15          | 3.9577              | 8.8497                                 | 53.329                                  | 2.88 e 4 | 3.54                       | 188.763 |
| B-52          | 7.7327              | 17.2908                                | 71.376                                  | 7.53 e 4 | 9.26                       | 660.671 |

3.1.  $L_o$  at  $x=0$  is found using Equation 47.  $L_o = \theta \sqrt{\frac{x - x_o}{2\theta}}$ . If  $x = x_o$ , the equation would be undefined. As a result,  $x$  is assumed to be one fighter category length (58.5 ft). It is assumed that the value of  $L_o$  at  $x=0$  is the same at  $x=58.5$  ft. For the F-18,  $L_o = 0.730 \text{ ft} * (58.5 \text{ ft} / (2 * 0.730 \text{ ft}))^{(1/2)} = 4.6212 \text{ ft}$ . (note: values in table were computed by spreadsheet. Hand calculation of this example will produce minor rounding errors).

3.2.  $L_o$  at  $x=5\Delta x$  is found using the same procedure in 3.1. but  $x - x_o$  is defined as 5 times 58.5 ft (5 times the fighter category length). For the F-18,  $L_o \text{ at } 5\Delta x = 0.730 \text{ ft} * (5 * 58.5 \text{ ft} / (2 * 0.730 \text{ ft}))^{(1/2)} = 10.335 \text{ ft}$ . (note: values in table were computed by spreadsheet. Hand calculation of this example will produce minor rounding errors).

3.3.  $U_o$  at  $x=5\Delta x$  is also found using Equation 47.  $u_o = \frac{U_\infty}{\sqrt{\frac{x - x_o}{2\theta}}}$ .  $x - x_o$  is defined

as 5 times 58.5 ft (5 times the fighter category length). For the F-18,  $u_o \text{ at } 5\Delta x = (881.318 \text{ ft/s}) / (5 * 58.5 \text{ ft} / (2 * 0.730 \text{ ft}))^{(1/2)} = 62.271 \text{ ft/s}$ . (note: values in table were computed by spreadsheet. Hand calculation of this example will produce minor rounding errors).

3.4.  $R_\ell = u_o \ell / \nu$ . In this equation, velocity  $u_o$  is 3% of the mean velocity found at  $5\Delta x$ .  $\ell$  is the integral scale found at  $5\Delta x$  which is proportional to 25% of  $L_o$  at  $x=5\Delta x$ .  $\nu$  is a constant  $1.23e^{-4} \text{ ft}^2/\text{s}$ . For the F-18, the turbulence Reynolds number  $R_\ell = ((0.03 * 62.271 \text{ ft/s}) * (0.25 * 10.3335 \text{ ft})) / (1.23e^{-4} \text{ ft}^2/\text{s}) = 3.92 e^4$ . (note: values in table were computed by spreadsheet. Hand calculation of this example will produce minor rounding errors).

R002593416

3.5.  $\nu_T = R_\ell \nu$ . For the F-18,  $\nu_T = 3.92 \text{ e}^4 * 1.23 \text{ e}^{-4} \text{ ft}^2/\text{s} = 4.83 \text{ ft}^2/\text{s}$ .

3.6.  $A$  is a non-dimensional number proportional to  $\nu_T U_o$  at  $x=5\Delta x$ . Therefore, for the F-18,  $A = 4.83 \text{ ft}^2/\text{s} * 62.271 \text{ ft/s} = 300.521$  (note: values in table were computed by spreadsheet. Hand calculation of this example will produce minor rounding errors).

4. Calculations for modeled values for integral scale, mean rate of strain, Reynolds stress, and turbulent dissipation at  $x=5\Delta x$ .

| Aircraft Type | $\ell$ (ft) | $\bar{S}$ ( $\text{s}^{-1}$ ) | Reynolds stress ( $\text{ft}^2/\text{s}^2$ ) | $\epsilon$ ( $\text{ft}^2/\text{s}^3$ ) |
|---------------|-------------|-------------------------------|--|---|
| F-16          | 2.00        | 24.10                         | 2.56 e -1                                    | 6.16 e 0                                |
| F-15          | 2.21        | 24.10                         | 3.38 e 0                                     | 8.15 e 1                                |
| F-18          | 2.58        | 24.10                         | 1.37 e 4                                     | 3.31 e 5                                |

4.1.  $\ell$  is the integral scale found at  $5\Delta x$  which is proportional to 25% of  $L_o$  at  $x=5\Delta x$ . For the F-18,  $\ell = 0.25 * 10.3335 \text{ ft} = 2.58 \text{ ft}$ .

4.2.  $\bar{S}$  is approximated using the relation  $\frac{u}{\ell}$ , where  $u = U_o$  at  $x=5\Delta x$ . For the F-18,  $\bar{S} = (62.271 \text{ ft/s})/2.58 \text{ ft} = 24.10 \text{ s}^{-1}$  (note: values in table were computed by spreadsheet. Hand calculation of this example will produce minor rounding errors).

4.3. Reynolds stress is found by taking the line integral of Equation 52.

$\tilde{u}_1 \tilde{u}_2(y) = -A \frac{y}{L_o} e^{-y^2/L_o^2}$ . This was done using a computer application. The values of  $A$  and  $L_o$  were calculated in section 3 of this appendix.

4.4.  $\epsilon$  is found using the relation  $u_1 u_2 = \frac{\epsilon}{\bar{S}}$ . For the F-18,  $\epsilon = 1.37 \text{ e}^4 \text{ ft}^2/\text{s}^2 * 24.10 \text{ s}^{-1} = 3.31 \text{ e}^5 \text{ ft}^2/\text{s}^3$  (note: values in table were computed by spreadsheet. Hand calculation of this example will produce minor rounding errors).